Radiation damage of the optical components of the ATLAS TileCal calorimeter at the High-Luminosity LHC

Beatriz Catarina Pinheiro Pereira

Thesis to obtain the Master of Science Degree in

Engineering Physics

Supervisors: Dr. Rute Costa Batalha Pedro
Prof. Patricia Conde Muiño

Examination Committee

Chairperson: Prof. Mário João Martins Pimenta
Supervisor: Dr. Rute Costa Batalha Pedro
Member of the Committee: Prof. José Maneira

December 2020

To my parents and to Pedro.

Acknowledgments

First of all, I want to thank my supervisors, Rute Pedro and Patricia Muiño for all the availability, support and patience during all the development of this dissertation. In special to Rute for the mentoring and guidance that lead to the concretisation of this work. To professor Agostinho for reviewing my proceedings, without him the publication wouldn't be possible. Also, I would like to thank Pawel Klimek and Ammara Ahmad for having time to discuss the best path to present the result in meetings.

À minha família por estar sempre disponível e presente. Em especial à minha mãe e ao meu pai pelo incansável apoio, pela ajuda e sobretudo pela paciência durante estes anos. Aos meus avós que sempre se esforçaram por me ensinarem e por me passarem os seus conhecimentos e valores. À minha avó Pilôfa por me deixar passar esta quarentena na sua casa para que eu pudesse espairecer.

Aos meus amigos Leonor, Gonçalo e André pelo companheirismo e anos que passámos juntos na FCT. Ao Caponso por estar sempre disponível para me ouvir e discutir ideias que tanto me fizeram crescer e ver o mundo de outra forma.

À Madalena por estar sempre disposta a treinar as minhas apresentações, por me ter feito companhia, ainda que online, durante toda a minha dissertação e ainda por ser uma excelente amiga disposta a ajudar-me sempre que necessário. À Mariana pelas horas passadas, sem nos apercebermos, a falar e a partilhar experiências.

Ao meu irmão, Guilherme, que sempre me incentivou a saber mais e esteve sempre presente para me ajudar quer na área de física como noutros assuntos da minha vida. E como diz a canção "No meio dos amigos; aprende-se muito mais; do que em todos os manuais, histórias de fazer corar; coisas da vida reais" e por isso um obrigado ao Gonçalo e ao Rafa pelos muitos anos de amizade. Ao António que está sempre pronto a partilhar comigo o que aprende bem como os seus projetos.

Ao Pedro a quem nunca vou conseguir agradecer o suficiente por estar sempre presente, mesmo nos momentos mais difíceis e que me ajudou a ultrapassar todos os pequenos e grandes obstáculos durante este meu percurso.

Resumo

O TileCal é um calorímetro hadrónico pertencente à experiência ATLAS do LHC. O material ativo é composto por telhas plásticas cintilantes, onde a luz é produzida e transmitida pelas fibras de deslocamento do comprimento de onda até aos fotomultiplicadores.

O programa Alta Luminosidade-LHC (AL-LHC) prolongará a utilização do TileCal por mais 20 anos do que inicialmente projetado. Pela exposição à radiação e ao envelhecimento natural os seus componentes óticos degradam-se. Como estes componentes não podem ser substituídos, a capacidade dos materiais em resistir à radiação terá de ser avaliada com precisão. A experiência ganha com detetores submetidos, durante muito tempo, a difíceis condições de radiação terá impacto no desenho de futuros detetores do FCC, bem como, noutros detetores similares. A resposta dos cintiladores e fibras do TileCal foi determinada explorando os sistemas de calibração que usam fontes de Césio e pulsos de Laser. As incertezas associadas à calibração a Laser foram estudadas para avaliar a degradação ótica. Os dados da *Run* 2 foram analisados, indicando que as células da camada A, e as células B11 e C10 perderam cerca de 5% de coleção de luz. Para as outras células não foram encontradas mudanças significativas. Os resultados foram extrapolados para o final da *Run* 3 e da AL-LHC, sugerindo uma perda de luz, para a maioria das células de aproximadamente 20% e as mais irradiadas podem perder até 80% de coleção de luz. Como a incerteza na extrapolação é elevada são precisos mais dados para ter uma melhor precisão.

Palavras-chave: LHC, ATLAS, TileCal, Resistência a radiação, Detetor de Cintilação.

Abstract

TileCal, a sampling hadronic calorimeter, is an essential component of the ATLAS detector at the LHC. The active material, made of plastic scintillating tiles, produces light when traversed by charged particles. The light is transmitted to photomultiplier tubes by wavelength shifting fibres.

The High Luminosity-LHC (HL-LHC) program will extend the TileCal lifetime for 20 years more than originally designed. The detector performance is affected by the increased exposure to radiation that will degrade the TileCal optics and by natural ageing. Since the TileCal's optical components cannot be replaced, their radiation hardness must be evaluated with precision. In addition, the experience gained with a real detector under harsh radiation conditions for long time will be invaluable for the design of future detectors at FCC or other detectors. The TileCal scintillators and fibres' response was determined by exploring information about dedicated calibration systems that employs a cesium source and laser light pulses. The uncertainties associated with the Laser calibration were studied to evaluate the optics' ageing. Run 2 data were analysed, indicating that cells of layer A, and B11 and C10 cells have already lost about 5% of light yield. No significant changes were found for the other cells. The results were extrapolated to the end of Run 3 and end of the HL-HLC, suggesting a light loss of about 20% for most cells, while the most irradiated may lose up to 80% of light yield. Nevertheless, the extrapolation uncertainty is large, so more data needs to be explored to reach better precision.

Keywords: LHC, ATLAS, TileCal, Radiation Hardness, Scintillator Detector.

Contents

List of Tables

List of Figures

List of Abbreviations

SM	Standard model
PMT	PhotoMultiplier Tube
WLS	WaveLength Shifter
CERN	European Organization for Nuclear Research
LHC	Large Hadron Collider
ATLAS	A Toroidal LHC ApparatuS
TileCal	Tile Calorimeter
OF	Optimal filtering
CIS	Charge Injection System
Las	Laser System
Cs	Cesium System
EB	Extended Barrel
LB	Long Barrel
R&D	Research and Development
FCC	Future Circular Collider
HL-LHC	High Luminosity-LHC phase
UV	Ultraviolet
CMS	Compact Muon Solenoid

Chapter 1

Introduction

The first scintillator device used for particle detection was the spinthariscope invented by Crookes in 1903 [1]. The scintillating material generates light when struck by ionising radiation. The spinthariscope consisted of a zinc sulfide screen that produces weak light when an α particle passes through it. The light detection was made with the naked eye. A quantitative way of detection was required and, in 1944, Curran and Baker replaced the naked eye by a photomultiplier tube, PMT, which converted the light into electrical pulses. Currently, this technique is still used to detect ionising particles in high energy physics, medical field and many applications of dosimetry. Typically, scintillator-based detectors consist of three main parts: a scintillating material, a photodetector such as a PMT and a readout system. Some of the scintillating materials used in the construction of these detectors may suffer damage with time, due to natural ageing of the materials, as well as with the accumulated radiation dose. A good knowledge of both is fundamental for the design of detectors for future high energy experiments. The study of scintillating materials in search for increased radiation hardness is expected to have a boost in the near future in view of the update European Strategy for Particle Physics, that remarked the importance of the R&D in preparation for the Future Circular Collider (FCC) [2]. The particle detectors that will operate at FCC will suffer radiation doses several times larger than the ones expected in whole life of the LHC experiments. In addition, the detectors will have to operate for an even longer period of time [3]. The experience gained with real detectors, such as those at the LHC, that are currently operating under harsh radiation damage conditions and for a long period of time will, therefore, be paramount to guide the design of future detectors. The principle of operation of the scintillator detectors, including the scintillation process, and previous studies of radiation damage in these materials are presented in Chapter 2.

The ATLAS experiment of the LHC, described in Chapter 3, is one example of a high energy physics experiment that uses plastic scintillator detectors in the Tile Calorimeter detector. The main purpose of this detector is to measure the energy and direction of hadrons and τ-jets by their interaction with the scintillator material, also contributing to the evaluation of the missing transverse energy and to the electron/photon identification. Scintillating light from TileCal is collected and guided by the wavelength shifting fibres until it reaches the photomultiplier tube and read-out electronics. Chapter 3 also describes the calibration and monitoring systems dedicated to the different TileCal components.

The main subject of this work is to study the radiation hardness of the TileCal optical components with a two-fold motivation. On the one hand, the TileCal detector was designed to operate for a period of up to six years at a maximum instantaneous $p-p$ collisions luminosity of 10^{34} cm^{-2} s^{-1}. The extension of the LHC programme with a phase of High Luminosity (HL-LHC) that will last for longer than 10 years, operating at an instantaneous luminosity of 5 to 7 times larger than the design, will challenge the detector components that cannot easily be exchanged and that have to operate with good performance till the end of the LHC lifetime. This is the case of the scintillating and optical components of the TileCal. It is, thus, crucial to estimate their expected radiation damage at the end of the HL-LHC phase, in order to design strategies to mitigate or recover at least part of the performance loss, in case it is found to be severe. On the other hand, the measurements of radiation hardness with a real detector that has operated up to now for more than 10 years, will be invaluable for the design of future detectors since some of the effects (such as low radiation doses for very long periods of time) are not easy to simulate in laboratory conditions or beam tests.

To study the radiation damage of the TileCal optical components, it is important to understand the uncertainties associated with the TileCal calibration procedures since they will limit the precision on the measurement of the radiation damage. Studies within the TileCal group already established the systematic uncertainties of the Cesium calibration. However, the uncertainties of the Laser calibration with the novel data analysis method — the Combined method — had not been studied. Whence, part of the dissertation work was dedicated to determine them. The method and the results obtained are presented in Chapter 4.

The LHC Run 2 ended in 2018, the measurements of the light yield of the TileCal optics in Run 2 are presented in Chapter 5. These measurements were modelled as a function of the simulated dose in Run 2 and extrapolated to future runs in order to study the radiation hardness of the optical components at the end of the Run 3 and High Luminosity LHC phase. This analysis and its results are also contained in Chapter 5.

In Appendix A, the distributions of the dose value calculated using GEANT4 simulation of ATLAS in the Tile Calorimeter region for $p-p$ collisions was developed by the Radiation Simulation working group of ATLAS and are used as an input for the evaluation of the radiation hardness.

During the development of this dissertation, some plots were discussed and approved by the TileCal group as public ATLAS results [4, 5]. The results about the uncertainties of the Laser system were presented in two Tilecal Calibration, Data Preparation and Performance in Tile Week. The results presented here are part of a TileCal internal note that will be the input for a publication in preparation. This work was also shown in a poster format in the 6^{th} IDPASC/LIP PhD Students Workshop [6] and in the 5^{th} International Conference on Particle Physics and Astrophysics in a poster [7] format as well as the proceedings [8].

Chapter 2

Scintillator detectors

This Chapter is devoted to introducing ionising radiation detectors based on scintillators. Section 2.1 explains the scintillation process intrinsic to this type of detectors. Section 2.2 describes how plastic scintillators operate. Section 2.3 discusses the scintillation light detection, focusing on photomultiplier tubes.

When ionising radiation interacts with matter, it loses energy by transmitting it to the material. Scintillating materials will produce photons with smaller energy than the initial incident radiation upon de-excitation. This phenomenon is called scintillation. Larger ionization energy will generate more photons.

There are many scintillating materials, such as NaI, CsI and benzene, used for radiation detection in high energy particle detection. A good scintillator to detect radiation needs to be efficient in converting the excitation energy into fluorescent radiation and transmitting light from the fluorescence emission. In scintillator detectors, light detection employs devices that convert light into an electrical signal. There are many options, such as photodiodes or photomultiplier tubes (PMT), and the choice of photodetector is also important. The conversion efficiency of the device must be high to maximize the collected information in the form of light to the output information in the form of an electrical signal. The typical efficiency of a PMT is of the order of 30% [1].

Over time much development has been made around scintillators, and they can be divided into two groups: organic and inorganic. They are the basis of many detectors in particle physics experiments, such as calorimeters.

2.1 The Scintillation Phenomenon

Organic scintillators, which can be solid (plastic) or liquid, are made of aromatic hydrocarbon compounds consisting of ring molecules of benzene (C_6H_6). The electronic configuration of the carbon in the ground state is $1s^2 2s^2 2p^2$. The promotion of one $2s^2$ electron pair to the empty $2p$ orbital takes place to bind carbons and hydrogen in the benzene molecule. The carbon bound configuration in the molecules is $1s^2 2s^1 2p^3$ leaving four valence electrons, and the hydrogen configuration is $1s^1$. Each carbon atom forms three σ bonds with two carbon atoms and one hydrogen atom. The other electron is a π electron and prone to excitation by radiation [9]. In scintillating organic materials, the light is generated from the de-excitation of π electrons of the molecules. The energy levels of the π electrons are presented in Figure 2.1, where the singlet and triplet states are denoted by S_{nm} and T_{nm}, respectively, and where n has the values of $0, 1, 2, 3$ representing the electron energy level and m represents the respective vibrational sub-level and can have values of $0, 1, 2, 3$. The ground state is represented by S_{00}.

Electrons in higher energy levels than the first excited state decay to the S_{10} state through internal conversion without photon emission. This decay has a very short time, typically smaller than 10 ps. The decay of S_{10} to S_{0m} leads to photon emission within a time of the order of ns (depending on the scintillator) and is called fluorescence [1]. In the triplet case, the excited electrons decay to T_{10} due to thermal degradation. The decay from this state to the singlet state occurs by radiative transitions with photon emission, a process known by phosphorescence that has a decay time in the order of ms [10, 11].

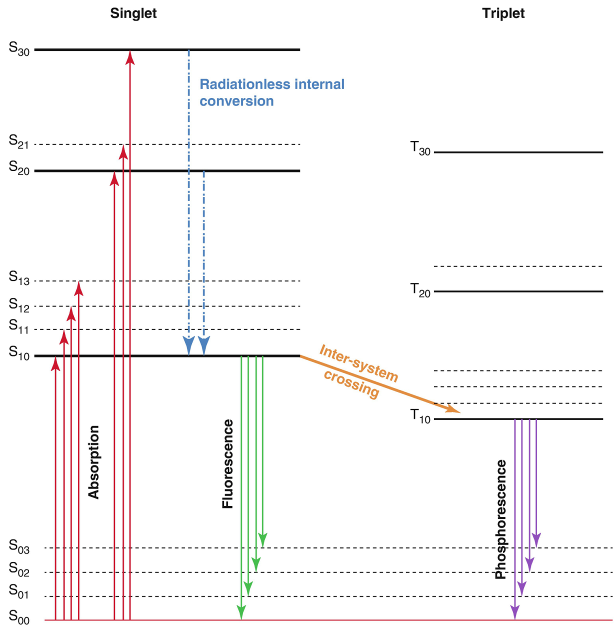

Figure 2.1: Schematic of absorption and emission levels of a benzene molecule. The singlet states are represented by S and the triplet states are represented by T. The first index indicates the state and the second index the respective excited or ground state [12].

The intensity of light produced in scintillators is almost linear to the energy deposited by the incident ionising particle. The emission of photons in a scintillator can be approximated by an exponential decay described in Equation 2.1 where τ_s and τ_f are constants referring to the slow (phosphorescence) and fast (fluorescence) components, respectively, and the relative magnitudes, A and B can vary with the material of the scintillator [1].

$$N(t) = Ae^{(-t/\tau_f)} + Be^{(-t/\tau_s)} \tag{2.1}$$

It is important to note that these processes obey the Franck-Condon principle, where their transition probability is proportional to the overlapping area of the two states' vibrational wave function. This principle is illustrated in Figure 2.2, where an excitation from the ground state to the second vibrational state of the next energy level occurs. Then the de-excitation, from the lowest vibrational state of that level to the second vibrational state of the lowest level, occurs. The difference – shift — in energy, wavelength or frequency between absorbed energy and emitted photon energy, represented by q_{01}, is called Stokes shift.

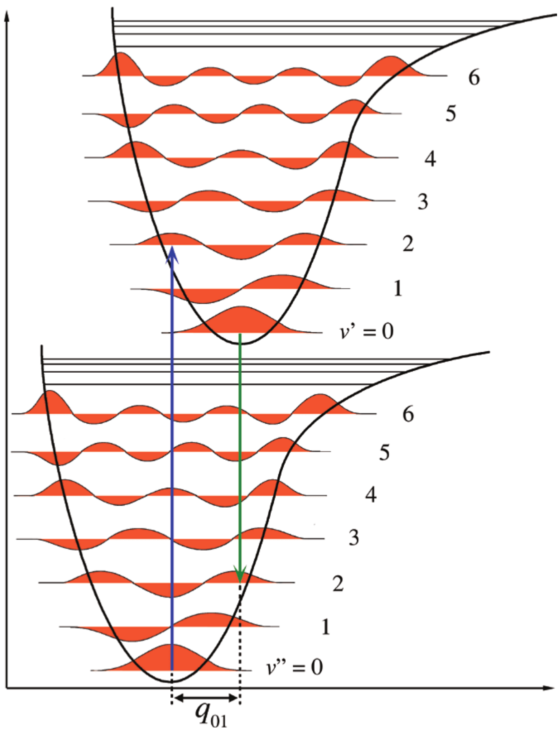

Figure 2.2: Schematic of absorption and emission levels of an organic molecule illustrating the Stokes shift. [13]

The Birks law [14] defines the light output per ionising particle unit length, dL/dx, for the scintillators detector as:

$$\frac{dL}{dx} = \frac{\epsilon_s \frac{dE}{dx}}{1 + k_B \frac{dE}{dx}} \tag{2.2}$$

where $\frac{dE}{dx}$ the energy loss in the material, ϵ_s is the absolute scintillation efficiency and k_B the parameter is the Birk's constant, dependent on the material, governing non-radiative processes dependent on the density of excited molecules. This model assumes a linear response of the detector and a non-linear component due to non-radiative quenching interactions between the excited molecules created along the incident particle path. A larger ionisation power yields a larger density of excited molecules, hence more quenching interactions will take place for these particles [1, 14].

2.2 Plastic Organic scintillators

A typical plastic organic scintillator is composed of three parts: a polymer base, a primary dopant (with a concentration $\sim$ 1%) and a secondary dopant (with a concentration $\sim$ 0.05%). A schematic illustrating the absorption and emission of the scintillator composed of these three parts is presented in Figure 2.3.

The polymer base, such as polyvinyltoluene (PVT) or polystyrene (PS), usually has an absorption band in the deep UV (240-280 nm) and an emission spectrum in the UV region of 290-370 nm [9]. The energy is transferred to the primary dopant mainly through the Förster mechanism, which is proportional to the overlap between the material's emission spectrum and the absorption spectrum of the acceptor, and to the dopant concentration. Therefore, the primary dopant, such as p-terphenyl (PTP) and 2-(4-tert-butylphenyl)-5-(4-biphenylyl)-1,3,4-oxadiazole (BPBD), must have a high solubility in the plastic, a high quantum light yield and an absorption band that overlaps the emission spectrum of the base. Its emission is generally in the UV region. This wavelength is not well adjusted to the quantum efficiency of the light detectors such as PMTs. A second dopant, e.g. 4-bis(5-phenyl-2-oxazolyl)benzene (POPOP), 1,4-bis(4-methyl-5-phenyl-2-oxazolyl)benzene (DM-POPOP) and 1,4-bis(2-methylstyryl)benzene (bis-MSB), is used to shift the wavelength of the light emitted by the primary dopant to a wavelength compatible with the light detection efficiency of the photodetector, which is usually in the visible range.

The light yield of scintillators that uses PS or PVT-bases is affected by the self-absorption of intrinsic radiation [15]. The concentrations are chosen to maximise light absorption efficiency by the next molecules in the chain and minimise the reabsorption by the previous material.

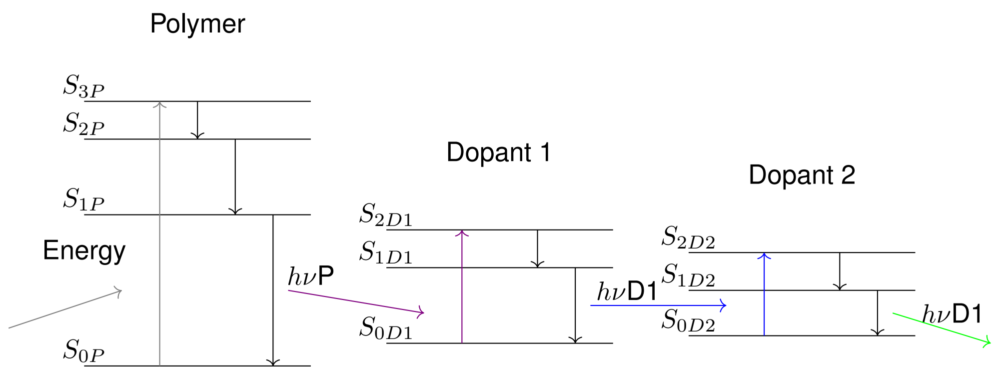

Figure 2.3: Schematic of absorption and emission levels of the scintillator with a polymer based and two dopants.

2.2.1 Radiation damage

The radiation hardness of the scintillating material is an exciting topic to discuss since it is important to understand if the organic scintillator detectors will be suitable for the radiation environment where they will operate on. This was the case of the design of the LHC experiments, where the materials used in the detectors had to be tested for their radiation hardness prior to construction. Organic materials are known to suffer from radiation damage and the light output, L, of the scintillator decreases exponentially with the dose received as [9, 16]:

$$L(d) = L_0 e^{-d/D} \tag{2.3}$$

where L_0 is the light output before the irradiation, D is the exponential constant governing the degradation rate and d is the dose received. The dose in the irradiated material is defined as the energy deposited, E_{dep}, by ionising radiation per unit mass of the material:

$$d = \frac{E_{dep}}{m} = \frac{E_{dep}}{\rho \times volume} \tag{2.4}$$

where m is the material mass and ρ the density of the material, and the dose rate is defined as the total delivered dose per unit of time.

The value of D depends mainly on the material used and some studies also showed a dependency on the dose rate, which will be discussed later. The commonly used dopants, such as PTP and POPOP, do not degrade significantly under irradiation, but the polymer base does [17]. The molecule chains in the scintillator suffer damage, breaking and cross-linking after being irradiated. This leads to changes in the structure of the polymers and the production of free radicals, which absorb and scatter the scintillation light affecting the light yield, transmittance and mechanical properties of scintillators [15]. To understand more how the degradation process occurs, it is important to study the impact of the dose rate effects in damaging the scintillator and the recovery process.

Dose rate and recovery

Studies show that lower dose rate results in increased light output damage, yet, the dependence is different for each scintillator [16, 18, 19]. The light output of scintillators employed in the CMS detector at the LHC accelerator as a function of the integrated luminosity, a quantity proportional to the dose, is shown in Figure 2.4 for different scintillators detector in layers 1 and 7. According to simulation corresponding to 23.3 fb^{-1} of integrated luminosity, the dose for layer 1 ranges from 0.01 to 0.2 Mrad (0.1 to 2 kGy) and for layer 7 is between 0.00005 and 0.03 Mrad (0.5 and 300 Gy). Since the irradiation period is common for this set of scintillators, their dose rates span 4 orders of magnitude. Using Equation 2.3 [1] to fit the data, if D does not depend on the dose rate, it will be expected that the scintillating tiles have the same exponential constants, regardless of the dose [16]. Since this is not verified, as shown by the fit results presented in Figure 2.4, the value D should also depend on the dose rate. This is confirmed by Figure 2.5, where the exponential constant values as a function of the dose rate are shown. The squared points correspond to different tiles in layers 1 and 7. The blue (red) circles represent measurement of a PS (PVT)-based scintillator after being irradiated with a ^{60}Co source. A strong dependence with the dose rate is observed, the tiles with the smaller dose rate have smaller exponential constant values. This implies that they suffer more damage for the same dose than the tiles with higher exponential constants values.

[1] The values of the exponential constant in terms of the integrated luminosity were converted into radiation dose units in Rad, using the proportionality between dose and integrated luminosity.

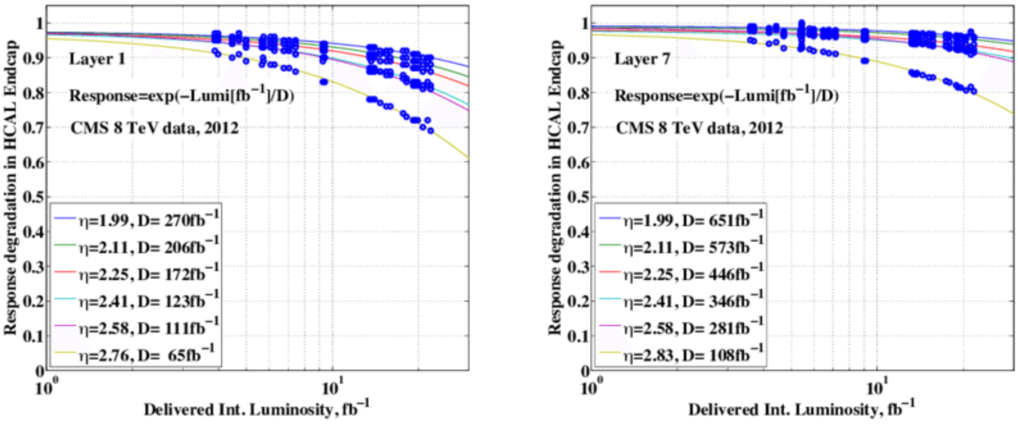

Figure 2.4: Relative light yield (the ratio between the light yield after the irradiation and the light yield before the irradiation) for CMS plastic scintillator tiles as a function of the integrated luminosity for (right) the layer 1 and (left) layer 7 [16].

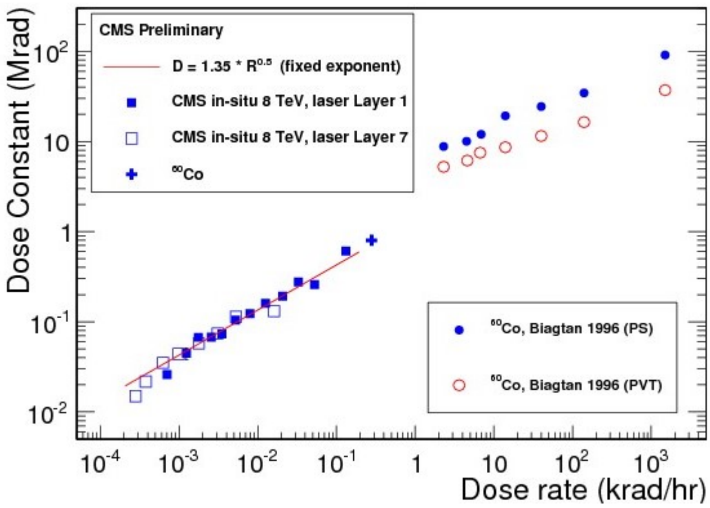

Figure 2.5: Exponential constant as a function of dose rate. The filled squares are the layer 1 results, and the open squares are the layer 7 results. The blue (red) circles are PS (PVT)-based scintillators irradiation with ^{60}Co source [16].

The dose rate effects can be related to gas diffusion in the surrounding atmosphere into the irradiated object. For example, if this gas is oxygen, the ionisation of this molecule may lead to the formation of free radicals, which can induce the breaking of the polymer chain. The diffusion is a slow process, therefore if the dose rate is very high, the impact of the total absorbed dose will be smaller than in the case of long irradiation at a low dose rate [20]. The diffusion rate is linked to the material, for example, in a PVT-based scintillator, the diffusion rate of oxygen is 13 times slower than for PS-based. This is why the PS seems to be more tolerant to radiation than the PVT. Moreover, a larger diffusion rate also facilitates the recovery of the material [16]. When radicals are more mobile, they are more likely to reform good bonds, reducing the damage. The free radicals that disappear after a no irradiation period are defined as temporary damage. Free radicals that remain after no irradiation period are defined as permanent damage [16].

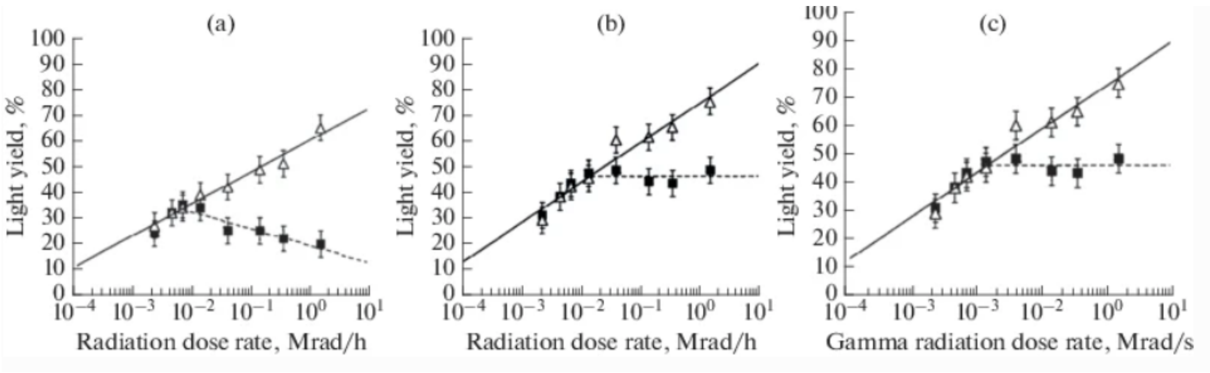

Figure 2.6: Light yield of SCSN-38 (a), BC-499-35 (b) and SCSN-81 (c) scintillators as a function of the radiation dose rate immediately after a 10 Mrad irradiation (black squares) and after seven days of recovery (white triangles) [15].

Furthermore, Figure 2.6 shows the light yield of three types of scintillators — SCSN-38, BC-499-35 and SCSN-81 —- immediately after a 10 Mrad (0.1 MGy) irradiation and after 7 days of recovery as a function of the delivery dose rate. The samples irradiated indicates that the recovery decreased with a decreasing dose rate. The samples irradiated with a larger dose rate recovered the most, while the samples irradiated with a smaller dose rate recovered the least or did not recover at all [18]. The latter happened for dose rates bellow 10^{-2} Mrad/h (100 Gy/h).

In summary, to obtain the minimum radiation damage, the base material should be chosen according to the detector's radiation environment (namely the dose rate at which it will operate), and the concentrations of the dopants should be chosen to maximise the efficiency of the wavelength shift. The work presented in this dissertation studies the radiation hardness of the plastic scintillators used in the Tile Calorimeter of the ATLAS detector at the LHC. These are based on PS and doped with a primary dopant with a concentration of 1.5% PTP and a concentration of 0.044% POPOP for the secondary dopant [21].

2.3 Light detection

In the scope of this work, the scintillation light is collected from the scintillator with a wavelength shifting (WLS) fibre, guiding it until it reaches the light detector, which for this case is a photomultiplier tube. A schematic of a PMT is shown in Figure 2.7. The WLS fibre, as the name indicates, is a fibre used to shift the wavelength of the light to be more compatible with the PMT detection efficiency spectrum.

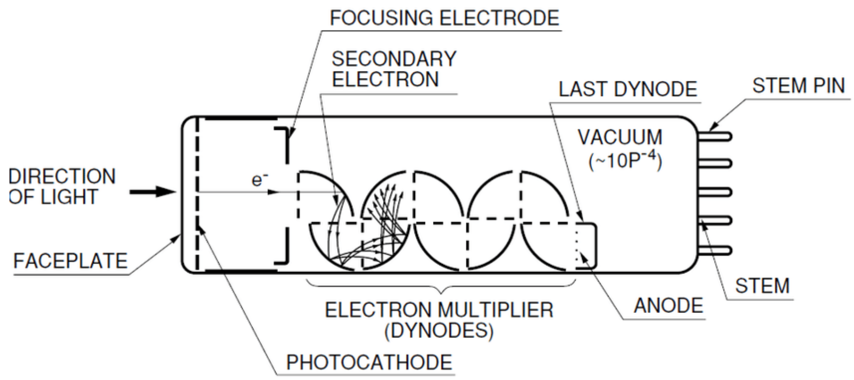

Figure 2.7: Schematic of photomultiplier tube [22].

The PMT consists of a vacuum tube with a photocathode made of a photosensitive material, followed by an electron collection system, an electron multiplier (dynodes) and an anode. When the photons interact with the photocathode material, if the energy is sufficient, an electron is ejected. Einstein's photoelectric effect governs the process:

$$E = h\nu - \phi \tag{2.5}$$

where E is the kinetic energy of the emitted electron, ν the frequency of the incident light, h the Planck constant and ϕ the work function, the minimum energy necessary to remove an electron from the material. The quantum efficiency, $\eta(\lambda)$ is the relation between the number of photoelectrons generated, N_{gen}, and the number of incident photons, N_{inc}, on the cathode:

$$\eta(\lambda) = \frac{N_{gen}}{N_{inc}}. \tag{2.6}$$

The number of photoelectrons generated depends on the wavelength, λ, since the photoelectric effect also depends on it — $\nu = \frac{c}{\lambda}$; where c is the light velocity. The WLS fibres are used to ensure that the photons that arrive at the PMT have the right wavelength so that the photoelectric effect is maximised.

Next, in the PMT, the ejected electron is collected and focused on the focusing electrode to reach the first dynode in the multiplier. This is achieved by applying a difference of potential between the cathode and the anode. The PMT's time resolution depends on the time it takes for an emitted electron to travel from the cathode to the anode. Electron multipliers are responsible for amplifying the weak photocurrent from the scintillator signal. They are made of a very low work function material to allow an electron that strikes this material with enough energy to release one or more electrons. This phenomenon is called secondary emission. The released electrons are accelerated and will strike the next dynode in the electron multiplier, since each dynode has applied a more positive potential that the previous one. This process is repeated across the number of successive dynodes and amplifies the current to be measured the anode. The High Voltage power supply is responsible for applying the difference of potential. The number of electrons released in the electron multiplier, δ, is defined as:

$$\delta = KV^{\alpha} \tag{2.7}$$

where K is a proportionality constant associated with the electron gain factor of the dynode, V the voltage applied between dynodes and α is a coefficient determinated by the dynode structure and the material. Assuming an equal applied voltage between dynodes the gain, G, can also be defined in function of the voltage applied:

$$G = KV^{\alpha n} \tag{2.8}$$

where n is the number of dynodes. The anode will receive the electrons multiplied and outputs the electric current to an external circuit [23].

Even when the PMT is not being illuminated, a small current is still detected, called dark current. This can occur due to the thermionic emission from the cathode or electron multipliers or due to radioactive contamination [1]. Also, some statistical noise can be detected, which directly results from the statistical nature of the photoemission and secondary emission processes. The first source arises from the statistical nature of the photoelectric effect. For a constant intensity of light, the number of photoelectrons emitted as well as the number of secondary electrons emitted will fluctuate with time, and the statistical nature of the photoelectric effect can be calculated assuming a Poisson distribution [23].

Chapter 3

The ATLAS Experiment at CERN's Large Hadron Collider

In Greece during the VI and V century BC, Leucippus and Democritus have proposed the atomic concept. They claimed that matter was formed by small, invisible, indivisible, and eternal particles called atoms [24]. However, it took until the XIX and XX centuries to discover the first fundamental particles [24]. In 1897, J. J. Thomson discovered the electron by accelerating cathode rays using two electrodes with a high voltage supply. The resulting beam was deflected with electric and magnetic fields to determine the charge-to-mass ratio of cathode rays. So, accelerators became necessary instruments in particle physics to understand the material world around us. The colliders also have an essential role: they are used to collide particles against each other, transforming them into new particles. Currently, the world's largest collider is the Large Hadron Collider (LHC).

The principal objective of the ATLAS LHC is the search for new particles belonging and beyond the Standard Model (SM). One achievement was the discovery of the Higgs boson by the ATLAS and CMS collaboration in 2012. An overview of the LHC and the ATLAS experiment and detectors is presented in this chapter. The first section shortly outlines how particles are accelerated and collided at the LHC. The ATLAS and its sub-detector system are briefly described in Section 3.2. Moreover, in Section 3.3, the ATLAS Tile hadronic calorimeter (TileCal) is described in more detail and its calibration and monitoring systems in Section 3.4 since it made part of the scope of the dissertation.

3.1 The Large Hadron Collider

The LHC is an accelerator located in the facilities of the European Organization for Nuclear Research - CERN - in the France–Switzerland border near Geneva. CERN's mission is to understand the birth of our universe, how the universe works, and its fundamental elements, using particle accelerators and colliders. In the LHC, it is possible not only to collide head on bunches of 10^{11} protons (p) but also heavy ions such as lead nuclei.

Before the particles reach the LHC, they are accelerated by a chain of linear and synchrotron accelerators. The main principle of the LHC is to use magnets to deflect and collimate the beam and use radio-frequency (RF) cavities to accelerate particles. The RF alternates between positive and negative charge to pull and push protons to accelerate them.

The journey of the proton starts inside a bottle of hydrogen. The atoms of hydrogen are sent to the source chamber, where they traverse an electric field that strips off their electrons. A schematic of the CERN accelerator complex is presented in Figure 3.1. The first accelerator where the protons go through is a linear accelerator called LINAC 2, where protons reach the energy of 50 MeV [25]. Next, the beam goes through the Proton Synchrotron that increases the beam intensity due to its four superimposed synchrotron rings and accelerates to 1.4 GeV [26]. The beam is then injected in a synchrotron accelerator called Proton Synchrotron (PS) with a circumference of 628 meters, where the beam reaches to 25 GeV [27]. The particles are then circulated in a second synchrotron the Super Proton Synchrotron with a circumference of 7 kilometres, to accelerate them up to 450 GeV [28]. Finally, the protons reach the LHC, which has a circumference of 27 kilometres and is 100 m underground. Here they can reach 99% of the speed of light with an energy of 7 TeV. Until now, the maximum nominal energy that was reached was 6.5 TeV. To reach this energy, the LHC employs superconductors to bend the particles and accelerate them with minimal losses. At the LHC, there are two beams pipes in an ultrahigh vacuum where the protons travel in opposite directions [29]. The beams of protons cross over inside the four detector caverns - ATLAS, CMS, ALICE, and LHCb - where the beam particles collide at a design center-of-mass energy, $\sqrt{s}$ equal to 14 TeV.

The LHC was designed for a $\mathscr{L} = 10^{34}$ cm^{-2}s^{-1} peak of instantaneous luminosity for proton collisions [30]. The instantaneous luminosity is defined as:

$$\mathscr{L} = \frac{N_b^2 n_b f_{rev} \gamma}{4\pi \epsilon_n \beta^*} F \tag{3.1}$$

where N_b is the number of particles in the crossing bunches, n_b is the number of bunches per beam, f_{rev} is the beam revolution frequency, γ the relativistic factor, F (≤ 1) is a reduction factor to account for geometric luminosity reductions due to the presence of crossing angles at the interaction point, ϵ_n is the normalised transverse emittance of the beam, and β^* is the beta function at the collision point that is related to the transverse size of the beam. Moreover, the integrated luminosity is given by:

$$L = \int \mathscr{L}(t)\, dt \tag{3.2}$$

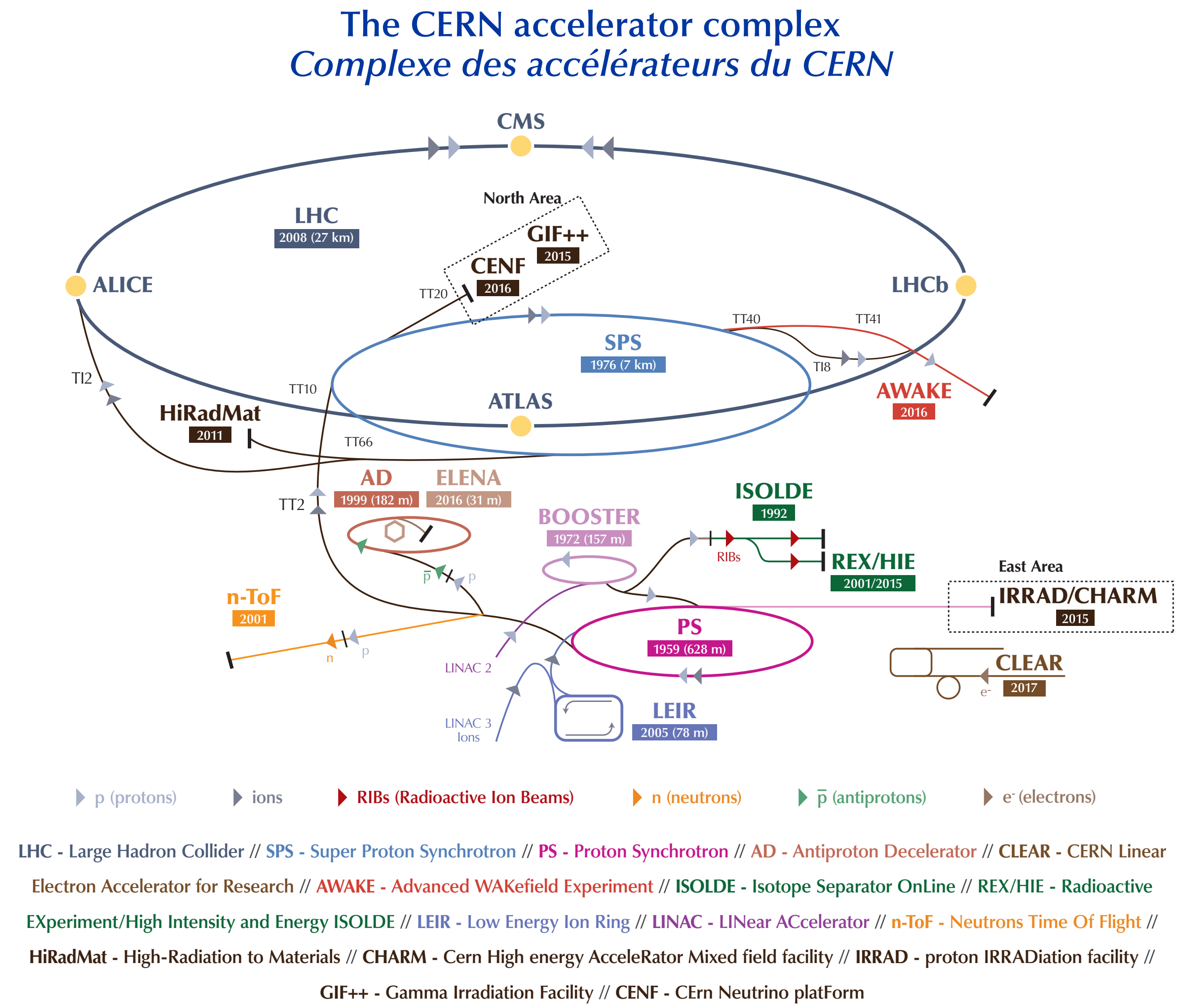

Figure 3.1: The CERN accelerator complex [31]. The path taken by the protons to reach the ATLAS experiment is shown in this figure, consisting of LINAC 2, Booster, PS, SPS and finally the LHC.

Figure 3.2 sketches the operation and upgrade plan of the LHC from 2011 until 2040. At the end of the Run 1, $p-p$ collisions at a center-of-mass energy of $\sqrt{s}$ =8 TeV were collected reaching an integrated luminosity of 30 fb^{-1}. During the LHC Run 2, the integrated luminosity between 2015 to 2018 was approximately 150 fb^{-1}, and the nominal luminosity ranged from 5-20 $\times 10^{33}$ cm^{-2}s^{-1} for $p-p$ collisions at $\sqrt{s}=13$ TeV [32]. Run 3 is expected to start, after two and a half years of shut down, at the end of 2021 and during this period the integrated luminosity is expected to be 160 fb^{-1}. According to this plan, in 2027 the HL-LHC will start. The instantaneous luminosity is expected to increase 5 to 7.5 $\times$ the nominal one so the integrated luminosity can reach more than 3000 fb^{-1}. For this last phase, not initially planned during the LHC experiments design, the radiation damage to the detectors must be evaluated carefully since their components can lose some properties when exposed to the radiation, resulting in performance degradation.

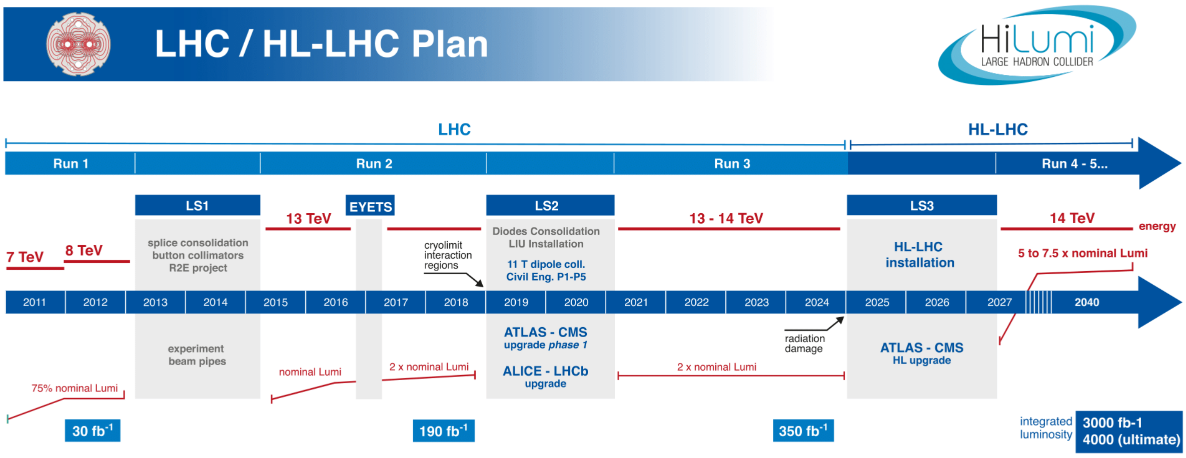

Figure 3.2: LHC and High Luminosity-LHC upgrade plan [33].

3.2 The ATLAS detector

Many particle physics phenomena can occur in $p-p$ collisions, which result in diverse collision products spanning a broad scale of energy. It is through the detection and analysis of the collision products that the $p-p$ interactions are studied and the LHC detectors play a central role in the LHC physics. The ATLAS (A Toroidal LHC ApparatuS) detector is responsible for detecting, measuring, tracking, and identifying various particles produced in the LHC collisions and investigating a wide range of high energy physics phenomena.

The ATLAS detector is a 46 m long cylinder with 25 m of diameter installed 100 m underground. The ATLAS coordinate system is based on the right-handed system, with the origin at the centre of the detector. The x-axis points to the centre of the LHC, the y-axis points upwards, and the z-axis is tangent to the beam line. Sometimes the spherical coordinates are used (r, Φ, θ), where the azimuthal angle Φ is defined in the x-y plane, transverse to the z-axis, while the polar angle θ is measured from the z-axis. The analysis of collision events often uses the pseudorapidity η (Equation 3.3) and the angular distance ΔR between two particles (Equation 3.4):

$$\eta = -ln \tan \frac{\theta}{2} \tag{3.3}$$

$$\Delta R = \sqrt{(\Delta\Phi)^2 + (\Delta\eta)^2} \tag{3.4}$$

The ATLAS detector, sketched in Figure 3.3 with all the components, is divided into four sub-systems: the inner detector [34] responsible for reconstructing the trajectories of electrically charged particle produced in the collision, the two calorimeters [35, 36] which measure the energy of electrons, photons and hadrons and the muon spectrometer [37] that serves to identify and measure muon trajectories with precision. The magnet system [38] is responsible for bending the charged particles trajectories. This system allows their momenta measurement, which is proportional to the curvature of the trajectory, and the curvature direction gives the sign of their charge.

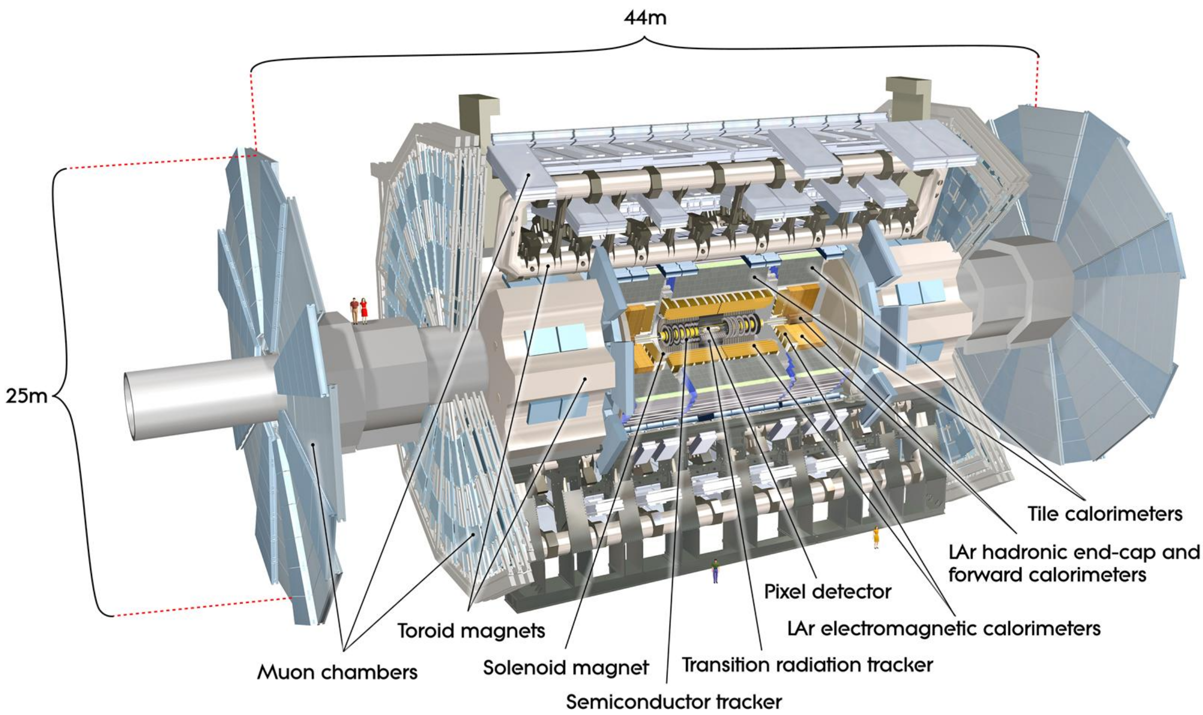

Figure 3.3: The ATLAS detector [39].

Table 3.1: Performance goals of the ATLAS detector [39].

Detector component	Required resolution
Inner detector	$\sigma_{p_T}/p_T = 0.05\% p_T \oplus 1\%$
EM calorimeters	$\sigma_E/E = 10\%\sqrt{E} \oplus 0.7\%$
Hadronic calorimeters:	
barrel and end-cap	$\sigma_E/E = 50\%\sqrt{E} \oplus 3\%$
forward	$\sigma_E/E = 100\%\sqrt{E} \oplus 10\%$
Muon spectrometer	$\sigma_{p_T}/p_T = 10\% p_T$ at $p_T = 1TeV$

Inner detector

The ATLAS Inner Detector (ID) was designed to track charged particles and determine the position of the collision vertices and secondary vertices from possible particle decays compound by three detectors and overall 146$\times$10^6 channels. The detector has 2.1 meters of diameter and is 6.2 meters long, as shown in Figure 3.4. This detector tracks electrically charged particles within the pseudorapidity range $|\eta| < 2.5$, with an excellent resolution in transverse momentum (p_T), meeting the ATLAS performance requirements shown in Table 3.1. The ID composed of a pixel detector made of silicon pixel layers allowing to reconstruct a 3-hit charged particle track; a semiconductor tracker made of silicon microstrips layers allowing to record the positions of charged particles with an accuracy of $17\ \mu$m per layer; a transition radiation tracker that uses layers of gaseous straw tubes filled with transition radiation material. When a charged particle passes through the gas and ionises it there is a drift of free electrons collected by a gold-plated tungsten wire, amplified and readout. Since the transition radiation is produced proportionally to the energy-mass ratio of the charged particle, this provides additional information especially to discriminate electrons from hadrons.

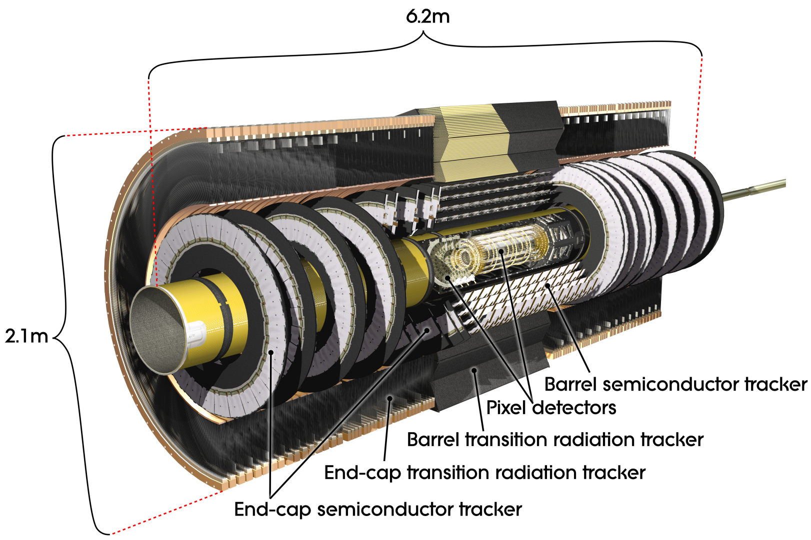

Figure 3.4: The ATLAS Inner Detector [40].

A solenoid magnet surrounds the ID. The intensity of the magnetic field generated by this magnet is 2 T. Its purpose is to bend the charged particles, allowing the particle momentum and electrical charge to be determined from the particle's curvature.

Calorimeters

The ATLAS detector comprises electromagnetic (EM) calorimeters and hadronic calorimeters, covering the pseudorapidity range of $|\eta| < 4.9$. They are built to measure the energy deposits of electrons, photons and isolated hadrons. They also contribute to particle identification and the muon momentum reconstruction. The EM is devoted to measuring photons' and electrons' energy, while the hadronic calorimeter measures the hadrons' energy. The sampling calorimeters are composed of an absorber material and an active material. The interactions of the incident particles produce a shower of particles — an electromagnetic shower in the case where the incident particle is an electron or photon, and an hadronic shower (which also have an electromagnetic component) in the case where the incident particle is an hadron. The particles of the shower deposit their energy in the active material, which will be detected in the form of light.

A schematic overview of the calorimeters of ATLAS is shown in Figure 3.5. The ATLAS calorimeters are divided into five different detectors: the Liquid Argon (LAr) electromagnetic calorimeter barrel (EMB), the LAr electromagnetic end-caps (EMEC), the LAr hadronic end-cap (HEC), the Forward hadronic calorimeters (FCal) and a central hadronic calorimeter (TileCal) divided in one Long Barrel and two Extended Barrels.

The first four systems use liquid argon as the active medium. The EMB and the EMEC uses lead as the absorber material, covering the pseudorapidity range of 1.375 $<|\eta|<$ 3.2 and 1.475 $<|\eta|$, respectively. The HEC covers $1.5<|\eta|$ <3.2 and uses copper as absorbers. Covering 3.1$<|\eta|$ <4.9 is the FCal and uses copper and tungsten as an absorber material. The TileCal uses plastic scintillator tiles as the active material and steel as absorber material. The EM was designed to have better energy and spatial resolution than the TileCal, which is the hadronic calorimeter with the best resolution, detailed in Table 3.1. The TileCal detector will be described in more detail in Section 3.3.

The electromagnetic e and the hadronic h energy responses of the ATLAS calorimeter are different: this is called a non-compensating response. For this reason, the energy scale of jets and hadronically decaying τ-leptons are corrected using simulation.

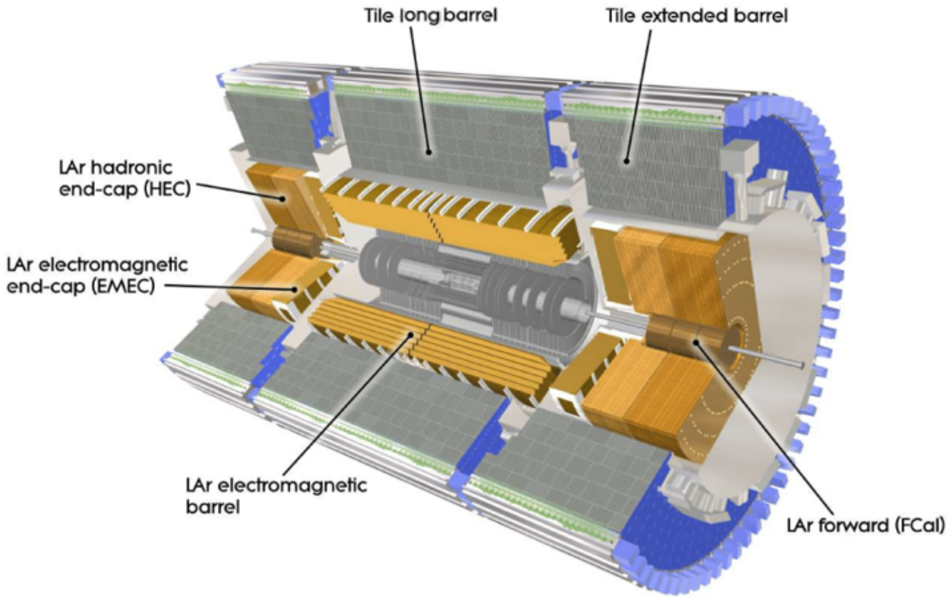

Figure 3.5: The ATLAS Calorimeters. Adapted from: [41].

Muon Spectrometer

The Muon Spectrometer (MS) is located at the outermost part of the ATLAS detector. It is responsible for measuring the momentum and trajectory of muons. The particles are deflected in a strong magnetic field, which is generated by large superconducting magnetic coils forming a toroidal magnet. The muon's momentum and electrical charge are determined from the particle curvature under the magnetic field. A scheme of the MS is presented in Figure 3.6, where it is possible to see that the MS is composed by Monitored Drift Tubes (MDT) and Cathode Strip Chambers (CSC), to track the muons with high precision in the range of $|\eta|<2.7$. Resistive Plate Chambers (RPC) and Thin Gap Chambers (TGC) covering $|\eta|<2.4$, are employed to provide information of prompt muon tracks for an event trigger, to identify the bunch-crossing and measure the muon's coordinates orthogonal to those measured with MDT and CSC.

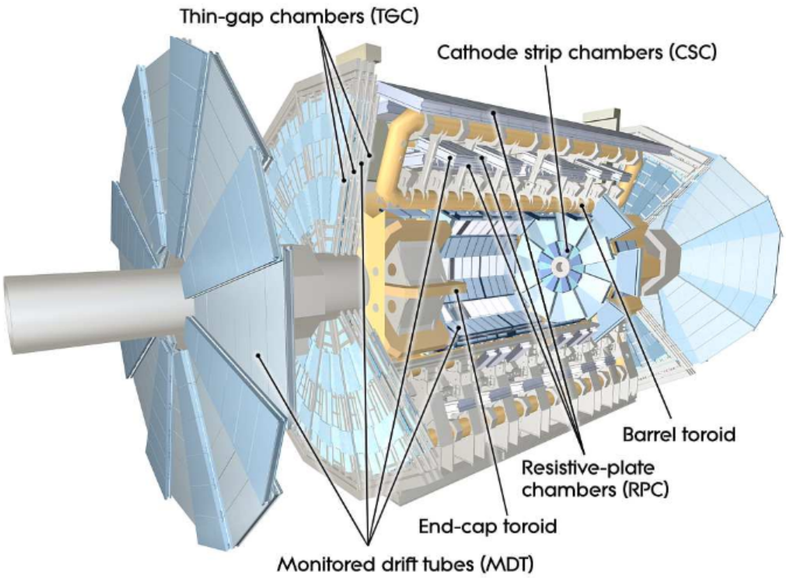

Figure 3.6: The ATLAS Muon Spectrometer [39].

3.3 The ATLAS Tile Calorimeter

TileCal plays an essential role in the ATLAS experiment. This detector's main purpose is to measure the energy and direction of hadrons and τ-jets and contributing to the evaluation of the missing transverse energy. It was designed to reach an energy resolution for jets of $\sigma/E = 50\%/\sqrt{E(\text{GeV})} \oplus 3\%$ ensuring a good sensitivity for measurements to the TeV scale.

The Tile calorimeter is located at the central region of the ATLAS detector, covering $|\eta| < 1.7$. As Figure 3.5 shows, TileCal is divided into three Barrels: one Long Barrel (LB) located in $|\eta| < 1.0$ and two Extended Barrels (EB) located on opposites sides of the LB and covering $0.8 < |\eta| < 1.7$. To differentiate the Barrels, the ones in the positive η side are called LBA and EBA, and the others are called LBC and EBC. The Barrels are segmented into 64 modules in Φ with a $\Delta\Phi$ granularity of approximately 0.1 radians. Also, the TileCal is divided into radial layers, as shown in Figure 3.7, the layer closer to the beam line is called A layer, the next layer is the B layer (BC in the Long Barrel), the one further from the beam line is the D layer. The E cells are placed in the gap region of the detector. The segmentation in η, for the first two layers is 0.1 in $\Delta\eta$, and for the D layer is 0.2. With these three coordinates, Φ, η, and radial one it is possible to define the three-dimensional detector cells of the TileCal, illustrated by Figure 3.7 [41]. In total, the Tile calorimeter has 5182 cells read out by 9852 electronic channels, the reason for this will be explained in what follows.

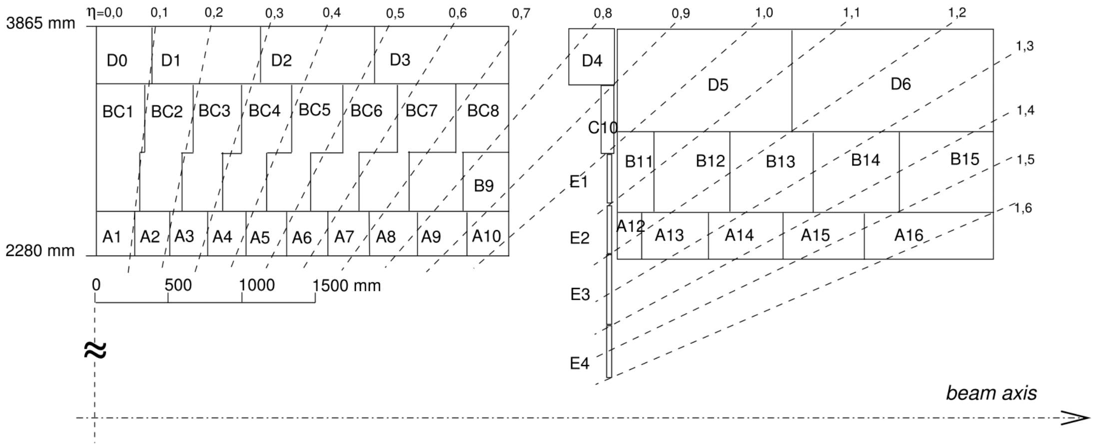

Figure 3.7: Map of Tiles cells of the LBA and EBA [42].

Each cell is composed of steel plates and scintillator tiles made of polystyrene basis [43]. The plates and the tiles are put alternately, as shown in Figure 3.8. There are approximately $460\ 000$ scintillators which have the function to produce light when ionising radiation passes through them. Each plastic scintillator tile is read by two wavelength shifting (WLS) optical fibres, each fibre connected to a tile edge. So when light is produced in the scintillator, the WLS fibres transport it to be read by a photomultiplier tube (PMT), as shown in Figure 3.8. The PMT converts light into an electrical signal, and each PMT is linked to a readout channel. A bundle of fibres groups several tiles into a common readout by a single PMT, defining the detector cell. Each cell is read by two sides, and this double readout is very important since the light attenuation in the scintillator tiles would cause a non-uniformity up to 40% with only one readout, and with the double readout, the percentage is reduced [41]. It also provides redundancy in the cell energy measurement in case of failure in one readout channel. Moreover, the electronics readout employs a high gain (HG) or low gain (LG) signal amplifier to better adjust the analogue signal amplitude to the dynamic range of the ADC converter.

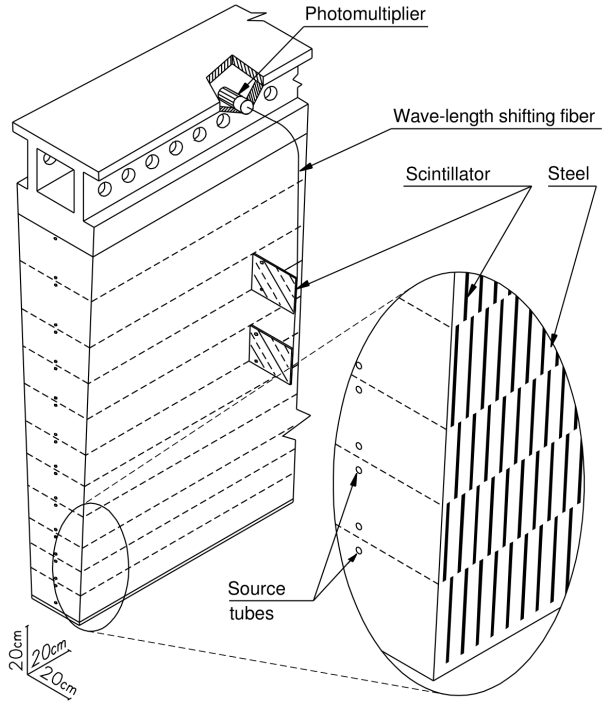

Figure 3.8: Schematic of the optical readout of the TileCal [42].

TileCal employs the optimal filtering (OF) algorithm to reconstruct the amplitude and time of the channel's signal. The OF ensures good resolution when there is accurate knowledge of the pulse shape. It is responsible for reconstructing the amplitude (A[ADC]) of the signal using a linear weighted sum of seven digital signal samples $S_i(i = 1, .., 7)$ read with a 25 ns time interval:

$$A[ADC] = \sum_{i=1}^{n=7} a_i S_i \tag{3.5}$$

where the OF weights, a_i, are obtained from the reference pulse shape, exhibited in Figure 3.9. The reference pulse shapes, one for each gain, were extracted from data taken at the test beam, selecting a channel with a given value of deposited energy and are the reference used to estimate of the OF weights.

[41].

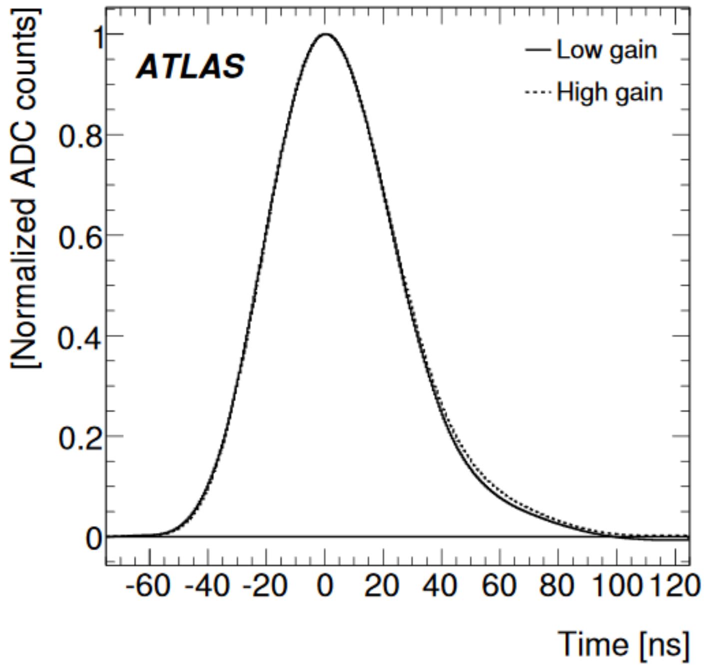

Figure 3.9: Pulse shape for high and low gain from test beam data, used as reference for the OF weights calculation. [41]

TileCal is a very complex detector, in a cylindrical shape divided in Barrels and each Barrel is divided into cells that employ a reading chain with diverse elements: scintillators, fibres, PMTs and electronics readout. It makes use the optimal filtering to reconstruct the signal amplitude and of distinct calibration, systems discussed in the next Section 3.4 to monitor the different elements of TileCal.

3.4 TileCal Calibration and Monitoring Systems

TileCal has three calibration systems, represented in Figure 3.10, to provide the necessary data to calibrate the energy measurement concerning fluctuations of the response of individual parts of the detector readout chain. Such fluctuations can be due to the high light fluxes that cause instabilities in the PMTs response and light yield degradation of the scintillators with exposure to radiation. The cell energy is reconstructed as:

$$E[GeV] = A[ADC] \times C_{pC \to GeV} \times f_{ADC \to pC} \times f_{Cs} \times f_{Las} \tag{3.6}$$

where $A[ADC]$ is the amplitude in ADC counts computed by the optimal filtering method, $f_{ADC \to pC}$ is the ADC to pC conversion factor measured by the Charge Injection System (CIS), $C_{pC \to GeV}$ is the pC to GeV conversion factor defining the energy scale determined with electron beams in past beam tests and f_{Cs} and f_{Las} are correction factors extracted from the Cesium and Laser calibrations, respectively [44].

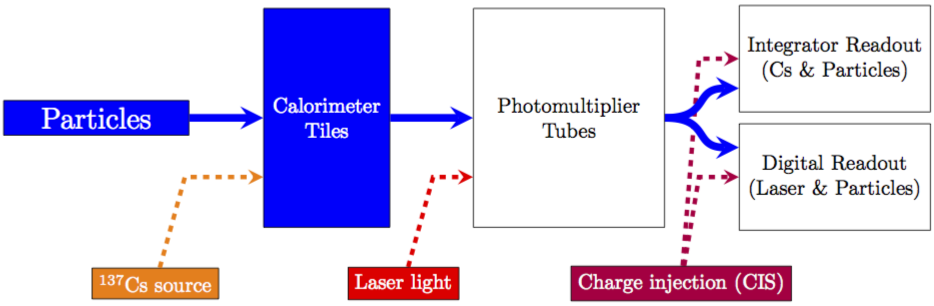

Figure 3.10: Schematic of the TileCal calibration systems. The ^{137}Cs source is responsible for calibrating the overall calorimeter response (tiles and fibres and the PMTs). The Laser light probes the response of the PMTs and electronics. The Charge injection calibrates the electronics readout [45].

3.4.1 Charge Injection System

The Charge Injection system is based on the injection of a known charge from 0 to 800 pC from a capacitor into a shaper circuit, that simulates the TileCal PMTs signal [46]. Although the signal produced is similar in shape to the signal produced by a PMT, the full width at half maximum (FWHM) is about 10% narrower and the amplitude 10% higher than a PMT signal with the same charge [47]. It is designed to determine the conversion factors from ADC to pC counts, $f_{ADC \to pC}$, from Equation 3.6, for all TileCal channels in both low gain and high gain readout and to track any variation with time.

The CIS is a very reliable calibration system. Studies in Figure 3.11 show that the systematic uncertainty is 0.7%. The electronics readout is very stable. As an example, from 2015 to 2018 the variation of the CIS conversion factors was measured to be less than 1%.

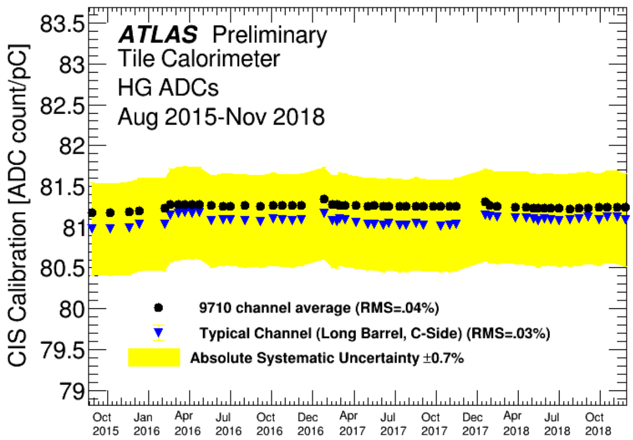

Figure 3.11: Detector-wide CIS calibration constant averages of all the high-gain ADCs for a selection of CIS calibration runs spanning Run 2, plotted as black circles. CIS constants from a typical channel are additionally plotted as blue triangles for comparison. The yellow error band are the systematic uncertainty in individual calibrations [48].

3.4.2 Laser System

The Laser system, represented in Figure 3.12, is used for monitoring the response of the calorimeter PMTs and their digital readout. This system uses a laser pulse with a wavelength of 523 nm. This wavelength was chosen to be close to that of the light coming out of the WLS fibres (480 nm) [49]. The Laser head sends the light beam through a semi-reflecting mirror that redirects about 10% of the light towards monitoring photodiodes. The light that passes through the semi-reflecting mirror reaches a rotating filter wheel with light filters of different transmittance, attenuating the outgoing light (attenuation factor from 3 to 1000), allowing the variation of intensity of the light beam. Then the light passes through another semi-reflecting mirror, where part of the light reaches to different monitor diodes and the other part reaches a light mixer responsible for expanding the laser beam diameter from about 700 μm up to the size of the bundle of 400 clear fibres. The light mixer is used to improve the split uniformity and avoid any speckle effects. The beam is guided through 400 long clear fibres with 100 m. Some of these 400 fibres are connected to four monitor diodes and the others reach the TileCal modules. Each of these fibres is connected to a second light mixer to split the light between the 32 (EB) or 45 (LB) fibres of 2 m long clear fibres, each of these fibres reaching one PMT.

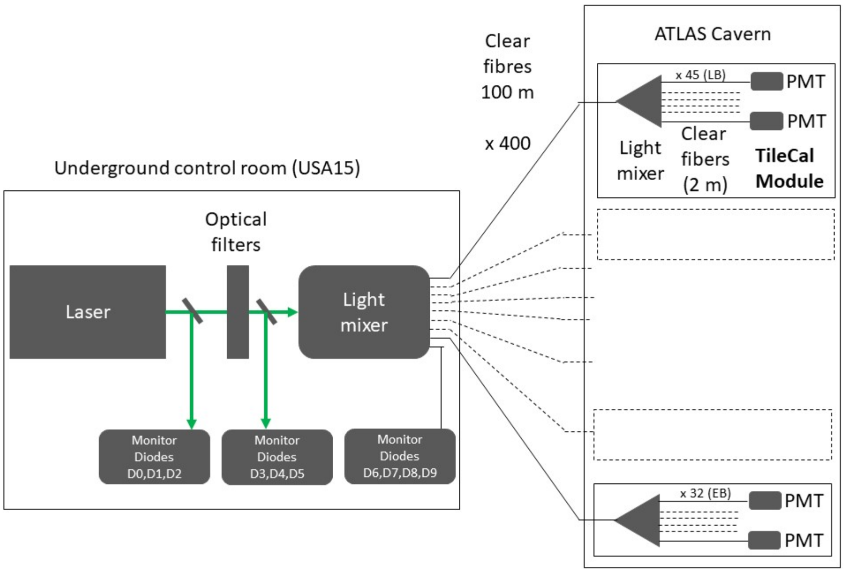

Figure 3.12: Schematic of the Laser system used during Run 2.

In summary, a controlled light pulse is sent via dedicated optical fibres to each of the 9852 PMTs that compose the readout. This system allows monitoring the stability and linearity of the PMTs response. The calibrations of the PMTs with the Laser system are done between two successive Cesium scans. Since this calibration runs are very fast when compared with others, they can be taken every two-three days during pauses of LHC collisions and during collision runs by pulsing the Laser in the empty bunch intervals.

Figure 3.13 shows the average PMT drift during Run 2 as measured with the Laser calibration system. It is important to remark that the down-drifts of the PMT response coincide with $p-p$ collision periods, while the response recovery occurs during LHC technical stops. Down-drifts mostly affect PMTs reading out cells of the TileCal inner layer A, which is the most exposed layer, with a variation of the response that can reach 6%.

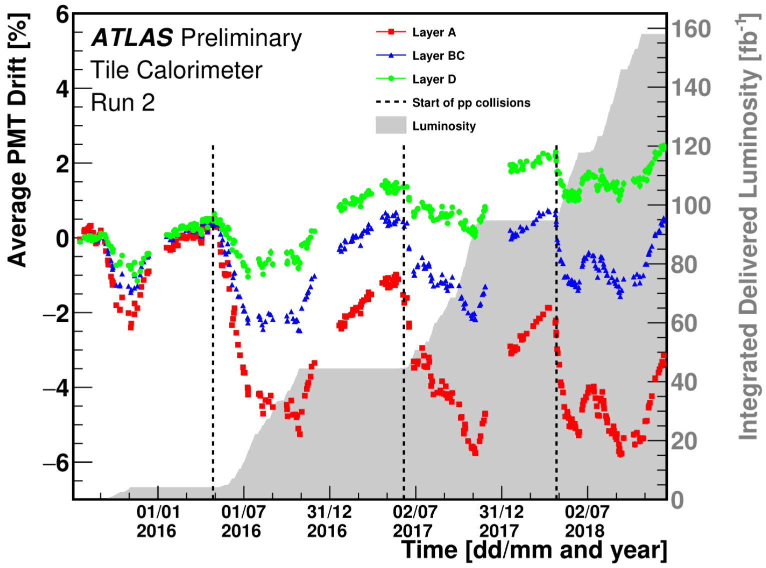

Figure 3.13: Evolution of the mean relative response of the 3 longitudinal layers (A, BC, D) in the ATLAS Tile Calorimeter as a function of time, as measured by the Laser calibration system. The dashed lines indicate the start of the pp collisions period in the respective years. The LHC delivered luminosity is shown for comparison [50].

3.4.3 Cesium System

The Cesium calibration system, as the name suggests, uses movable ^{137}Cs γ-sources, one for the Long Barrel and one for each Extended Barrel. Each source is inside a capsule, and it is carried along tubes (represented in Figure 3.8) by a hydraulic system with liquid flow inside, scanning the detector modules. The velocity of the source is of the order of 35 cm/s, allowing to scan the LB in one direction in 5 hours and the EB modules in 3 hours. Since the EB is smaller than the LB, during one scan the EB is scan in both directions while the LB source changes direction in each scan [51]. Cs scans need a pause of at least six hours in the $p-p$ collisions to perform the calibration. For this reason, this calibration can not be done very often. Also, the E cells are not calibrated by the Cs system since they do not have tubes for the capsule to pass. In 2016, a potential leakage in the hydraulic system of the Cs had been detected. Since then the Cs scan has been done less often to avoid possible damage to the other detectors.

The Cs calibration system provides information about the response of the TileCal optics (scintillator tiles and fibres) ($R(tiles+fibres)$) and the response of the PMTs ($R(PMT)$), and can be factorised into these two components:

$$\frac{1}{f_{Cs}} = R(Cs) = R(tiles+fibres) \times R(PMT) \tag{3.7}$$

The average response to the Cesium system, measured between 2015 and 2018, did not decrease more than 13%, as shown in Figure 3.14.

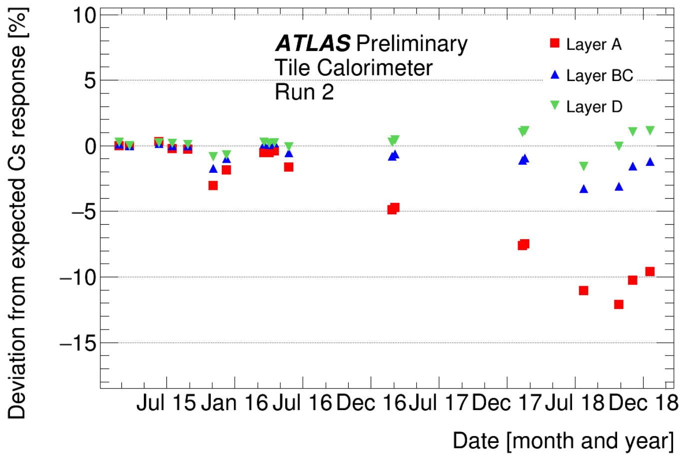

Figure 3.14: Evolution of Tile Calorimeter response to Cesium source as a function of time in 3 different longitudinal layers [52].

3.4.4 Minimum Bias System

The Minimum Bias system uses an integrator readout to measure the response of the detector to minimum bias events produced during the LHC $p-p$ collisions. The PMT signals caused by these events are integrated over, approximately 10 ms during the $p-p$ collisions. This system can also monitor the stability of the channels during data-taking, as well as providing the instantaneous luminosity, since the TileCal response to signals induced by the MB scale with instantaneous luminosity [44].

Each of these systems has an important role in the data analyses of the TileCal. The Cesium and the Laser systems are used to determine the uncertainties on the PMT response determined with the Laser discussed in the Chapter 4 and to evaluate the light output degradation of optics addressed in Chapter 5.

Chapter 4

TileCal Calibration with the Laser System

4.1 PMT response calibration

The Laser calibration system is responsible for calibrating the photomultiplier tubes and the electronics readout. The correction factor f^{Las} from Equation 3.6 is determined using this system for each PMT channel i (f_i^{Las}). For each pulse of the Laser system, described in Section 3.4.2, the PMTs responses and the diode responses are registered. The normalised response of the PMT i during the Laser run, $R_{i,p}$, is given by:

$$R_{i,p} = \frac{S_{i,p}}{D6_p} \tag{4.1}$$

where p is the Laser pulse, S_i is the reconstructed PMT signal, described in Section 3.3, and $D6$ is the photodiode 6 signal measured by the Laser box. The PMT signal is reconstructed using $A[ADC]$ and $f_{ADC\to pC}$ from Equation 3.6. The photodiode 6 measures the laser light from one of the four hundred 100 m long clear fibres dispatching the light into the detector. The Laser calibration procedure uses a Laser reference run taken close to the last Cesium scan used to calibrate the TileCal energy scale. The relative response of the individual PMT i, x_i^{Las}, is defined as:

$$x_i^{Las} = \frac{R_i}{R_i^{ref}} \tag{4.2}$$

with the normalised response of the PMT channel i during the Laser reference run define as R_i^{ref} and R_i is the PMT average response over all the pulses — $\langle R_{i,p}\rangle$. The Laser correction factor for each PMT channel, f_i^{Las}, is simply given by:

$$f_i^{Las} = \frac{1}{x_i^{Las}} = \frac{R_i^{ref}}{R_i}. \tag{4.3}$$

The respective PMT response variation, Δx_i^{Las}, is defined as:

$$\Delta x_i^{Las} = \frac{R_i - R_i^{ref}}{R_i^{ref}} \times 100\% \tag{4.4}$$

The measurement of the Laser constants (f_i^{Las}) can be biased due to instabilities related to the Laser calibration system itself, usually associated with the so-called global effects and fibre effects. The global effects are a global and coherent drift of all PMT caused by an instability of the reference diode, or from the variation of light received by the PMTs, or common ageing of the long fibres delivering the laser light. The fibre effects are caused by the variation with time of the light transmission or from light splitting fraction from fibre to fibre.

4.2 PMT calibration with the Combined method

The so-called Combined method is used to determine the PMT calibration constants, as described in Equation 3.6, from the bias introduced by the global corrections, δx_G, and fibre corrections, $\delta x_{f(i)}$, from laser events data:

$$f_i^{Las} \Longrightarrow f_i^{Las} = \frac{R_i^{ref}}{R_i} \times \delta x_G \delta x_{f(i)} = \frac{\delta x_G \delta x_{f(i)}}{x_i^{Las}} \tag{4.5}$$

The global and fibre corrections are calculated by comparing the PMT response with the PMT gain, which, if determined correctly, is not biased by the light fluctuation.

In order to determine the PMT gain, one explores the statistical nature of the photoelectrons production and multiplication inside the PMT.

The PMT gain, G, defined as:

$$G = \frac{\langle q \rangle}{e \cdot \langle N \rangle} \tag{4.6}$$

where e is the electron charge, $\langle q \rangle$ is the average anode charge q measured during the run and $\langle N \rangle$ the average number of photoelectrons.

The main contributions to the PMT anode charge fluctuations are: variation in the intensity of the laser source called coherence factor, fluctuations in the photoelectron emission spectrum and multiplication (following a Poisson distribution):

$$\frac{Var[q]}{\langle q \rangle^2} = f \cdot \frac{Var[N]}{\langle N \rangle^2} + \frac{Var[I]}{\langle I \rangle^2}. \tag{4.7}$$

where f is the excess noise factor based on the Poisson distribution photostatistic and $\langle I \rangle$ ($Var[I]$) the average (variance) light intensity I of a pulse source on the cathode. Since the signal from the calibration system produced more than thousands of photoelectrons, the noise effect can be neglected, to high light intensity. Another assumption to calculate the gain is that the laser light has temporal coherence. The coherence factor, $\frac{Var[I]}{\langle I \rangle^2}$, depends only on the characteristics of the light source. For a common light source the coherence factor can be measured with several PMTs using the covariance, Cov:

$$\frac{Var[I]}{\langle I\rangle^2} = \frac{Cov[q_i, q_j]}{\langle q_i\rangle\langle q_j\rangle} \tag{4.8}$$

where i and j represent any pair of PMTs. Equation 4.7 can be rewritten using Equation 4.8 to determine the PMT gain as:

$$G = \frac{1}{f \cdot e} \cdot \left(\frac{Var[q]}{\langle q\rangle} - \frac{Var[I]}{\langle I\rangle^2} \cdot \langle q\rangle \right) \tag{4.9}$$

the factor of coherent is difficult to measure so, in order to limit the weight of $\langle q\rangle$ that multiplied by this factor only values with small reconstructed charges, meaning low light intensity will be used. The relative gain of the PMT i ($x_{G,i}$) with respect to a reference is given by:

$$x_{G,i} = \frac{G_i}{G_i^{ref}} \tag{4.10}$$

where G_i is the gain of the PMT i, and G_i^{ref} is the gain of the same PMT determined with the Laser reference run. The reference gain is usually obtained by averaging over a set of 10 runs around the Laser reference run to overcome the known effects of fluctuations in the gain determination. Since the calculation of the gain works better at a lower light intensity, only high gain calibration runs with the filter wheel in the eighth position are used.

The global correction, δx_G, is determined from the average ratio between the PMT relative gain ($x_{G,i}$) and the relative response (x_i) using PMTs reading the D-layer and the BC1, BC2, B13, B14 and B15 cells. These PMTs are chosen because their response is more stable:

$$\delta x_G = \langle \frac{x}{x_G} \rangle \tag{4.11}$$

The PMTs with bad status (identified by data quality activities with data corruption, dead Analog to Digital Conversion (ADC) or no response to the CIS system), saturated or with an absolute difference between the high voltage (HV) set by the detector control system and the HV measured superior to 10 V are discarded.

The fibre correction, δx_f, is the average ratio between the PMT relative gain and relative response over all the channels connected to a common long fibre. To avoid double correction, the global correction must be taken into account when defining the fibre correction:

$$\delta x_f = \langle \frac{x}{x_G} \delta x_G \rangle \tag{4.12}$$

An important part of the work of this dissertation is discussed in Section 4.3. It consists of determining the uncertainties on the PMT response to the Laser calibration system using the Combined method.

4.3 Uncertainties on the PMT calibration

The uncertainties on the PMT response calibration using the Laser system are usually evaluated making a direct comparison between the calorimeter response to the Cs scans and Laser pulses. This procedure relies on frequent Cs scans where the effects from radiation damage on the optics are small enough to be neglected, i.e., where the evolution of the Cs constants should match the evolution of the Laser constants. Since the Cs system had a leakage problem (discussed in Section 3.4.3), not enough Cs scans were available for the years 2017 and 2018. A new indirect method was developed to determine the uncertainties on the PMT response, $R(PMT)$, that takes advantage of the double cell readout of TileCal and explores the responses to Cs, $R(Cs)$, and Laser measured with left and right PMTs reading the same cell.

As discussed in Section 3.4.3, the Cs calibration system provides information about the response of the TileCal optics and the PMTs. Rewriting Equation 3.7, the optical response read by the left PMT is:

$$R(tiles + fibres_L) = \frac{R_L(Cs)}{R_L(PMT)} \tag{4.13}$$

and by the right PMT is:

$$R(tile + fibres_R) = \frac{R_R(Cs)}{R_R(PMT)}. \tag{4.14}$$

where the R and L subscripts denote the response measured through the right and left side channels of the cell, respectively.

Assuming that the difference between the response given by the left and the right fibres connected to the same cell is equal, i.e. assuming $R(fibres_L) = R(fibres_R)$, one can write:

$$R(tile + fibres) = \frac{R_L(Cs)}{R_L(PMT)} = \frac{R_R(Cs)}{R_R(PMT)} \tag{4.15}$$

and the difference between the measured $\frac{R_L(Cs)}{R_L(PMT)}$ and $\frac{R_R(Cs)}{R_R(PMT)}$ can be explored to determine the uncertainties on the PMT response calibration.

The four Cesium scans and the four closest Laser runs to these scans, taken during the year 2018, were used. The Laser run and the Cs scan numbers, as well as the $p-p$ integrated luminosity, during 2018, corresponding to the time of the scans/runs, are presented in Table 4.1. The Cs scan 356509 was only performed in the Extended Barrel.

The relative response to Cs, x^{Cs}, is determined with respect to the first Cs scan (Scan=342550) as the reference scan, $R^{ref}(Cs)$:

$$x^{Cs} = \frac{R(Cs)}{R^{ref}(Cs)} \tag{4.16}$$

The Laser reference is also from the same date. The response to the Cs, $R(Cs)$, the relative response to the Cs, x^{Cs}, and the relative response to the Laser, here $x^{Las} \equiv x_i^{Las}$ defined in Equation 4.2, are shown for all the channels reading the A1 and the A13 cells in Figure 4.1. In the beginning of the

TileCal, the response to Cs was 1.0 for all channels and until 2018 the response has been decreasing. In Figure 4.1 — top the average response for both cells is in the order of 0.9, meaning that a global loss for those cells is about 10%, with an identical RMS, even so, the cell A13 has a smaller response. The results for the response to the Laser system are very similar, the A13 cell has a smaller response when compared with the A1 cell.

Table 4.1: Calibration type, Run/Scan number, date and integrated luminosity of the data analysed to determine the uncertainties on the PMT response calibration with the Laser II system.

Calibration type	Run/Scan number	Date (2018)	Integrated Luminosity [fb^{-1}]
Cs	342550	17 February	0
Laser	344432	17 February	0
Cs	356509	25 July	28.6
Laser	356440	27 July	28.6
Cs	365480	27 October	63.3
Laser	364612	28 October	63.3
Cs	367400	3 December	63.3
Laser	367420	3 December	63.3

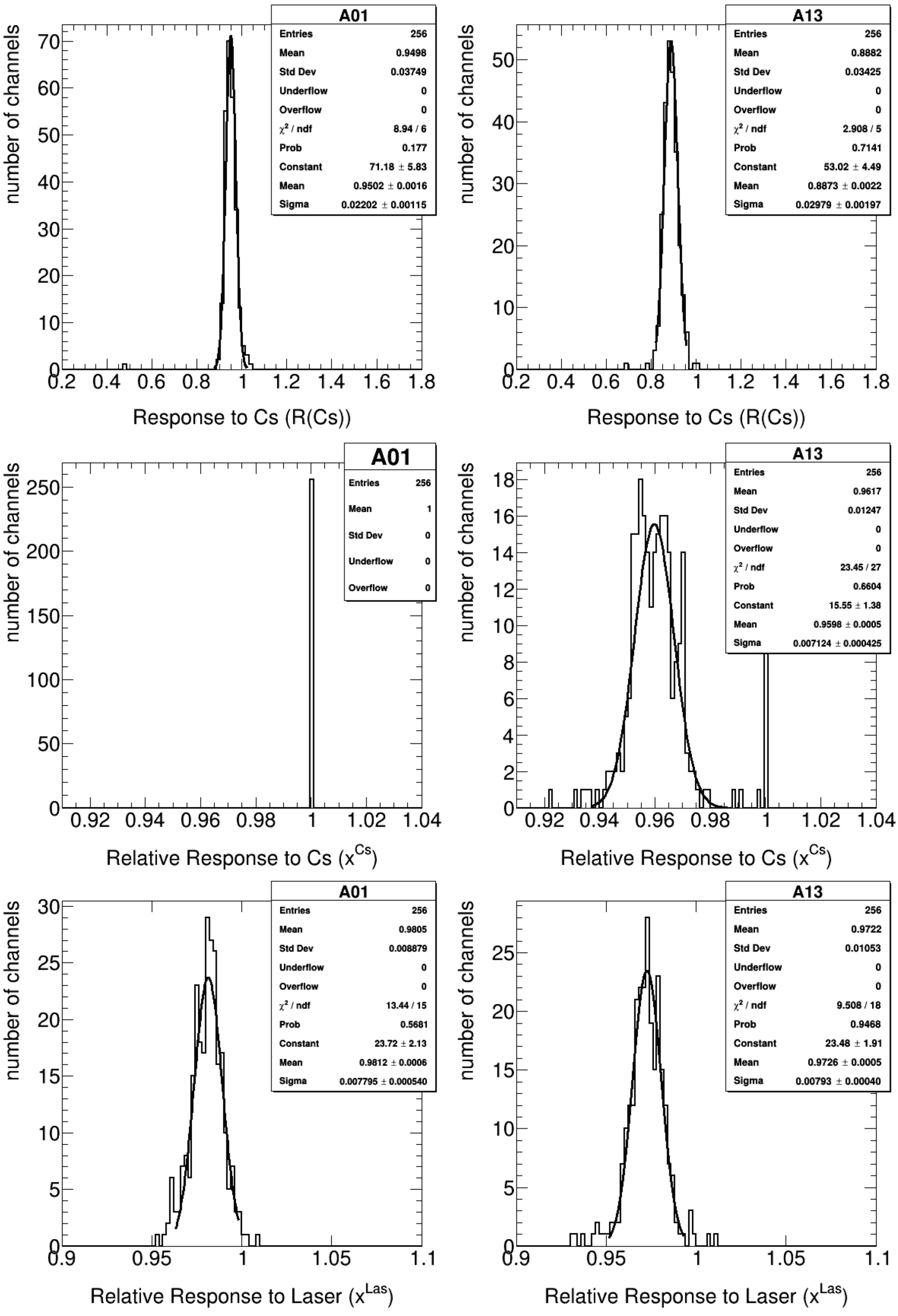

Figure 4.1: Distribution for (left) the A1 cell and (right) the A13 cell of the response (top) to Cesium, $R(Cs)$, for the February scan, the relative response (middle) to Cesium, x^{Cs}, and (bottom) to Laser, x^{Las}, for the scan/run of July. A Gaussian function was adjusted to the data, the parameters of the fit are presented in the plot.

The spike at the value 1.0 that is visible in the top right plot of Figure 4.1 is due to channels that were not updated with new constants from the Cs scans. These channels were excluded from further analysis. The comparison for the A13 cell in Scan=356509 with all channels or removing the cases where the relative response is one is represented in Figure 4.2.

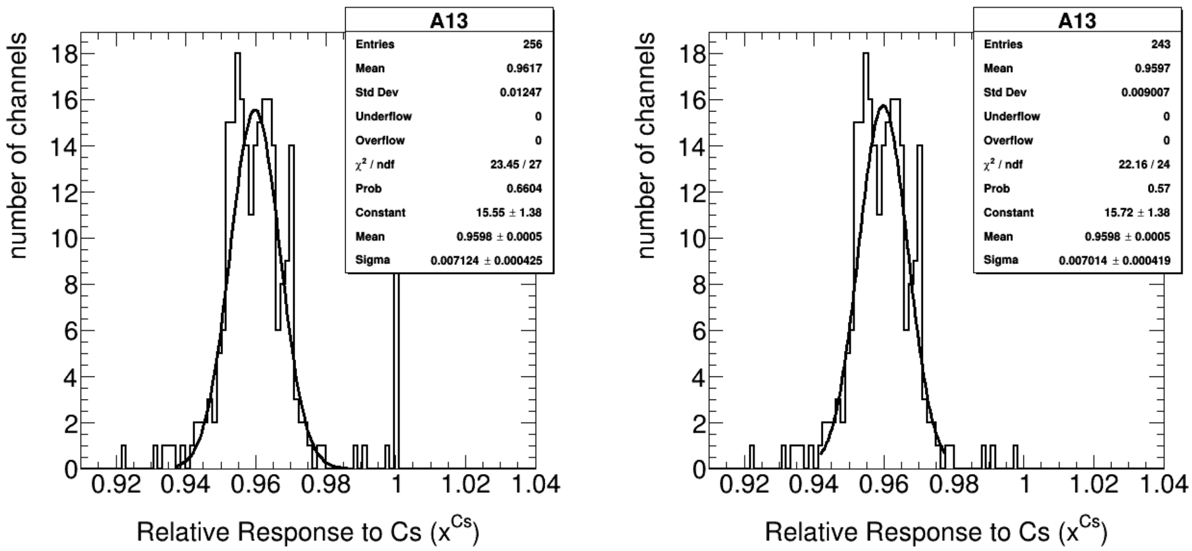

Figure 4.2: Distribution of the relative response to Cesium for the A13 cell (left) with all channels and (right) after removing the values of the relative response equal to 1.0 for the scan of July (Scan=356509). A Gaussian function was adjust to the data, the parameters of the fit are presented in the plot.

The mean from the Gaussian fit to the $R(Cs)$, x^{Cs} and x^{Las} distributions as a function of the integrated luminosity for A1 and A13 cells is presented in Figure 4.3. Since there was no Cs scan in the LB cells for the Scan=356509, the response to the Cs for the two first points for A1 cell is the same. As a consequence, the relative response to the Cs for A1 cell does not exist for the second run (with an integrated luminosity of 28.6 fb^{-1}). A decrease in the calorimeter response is observed with the increase of the integrated luminosity, either using the Cs or the Laser systems, x^{Cs} decreases more than x^{Las}. This is expected since the Cs system probes the response of the optical component and the PMTs while the Laser system only probes the PMTs response onwards. So, the extra degradation of these optical components is only seen in response to the Cs system.

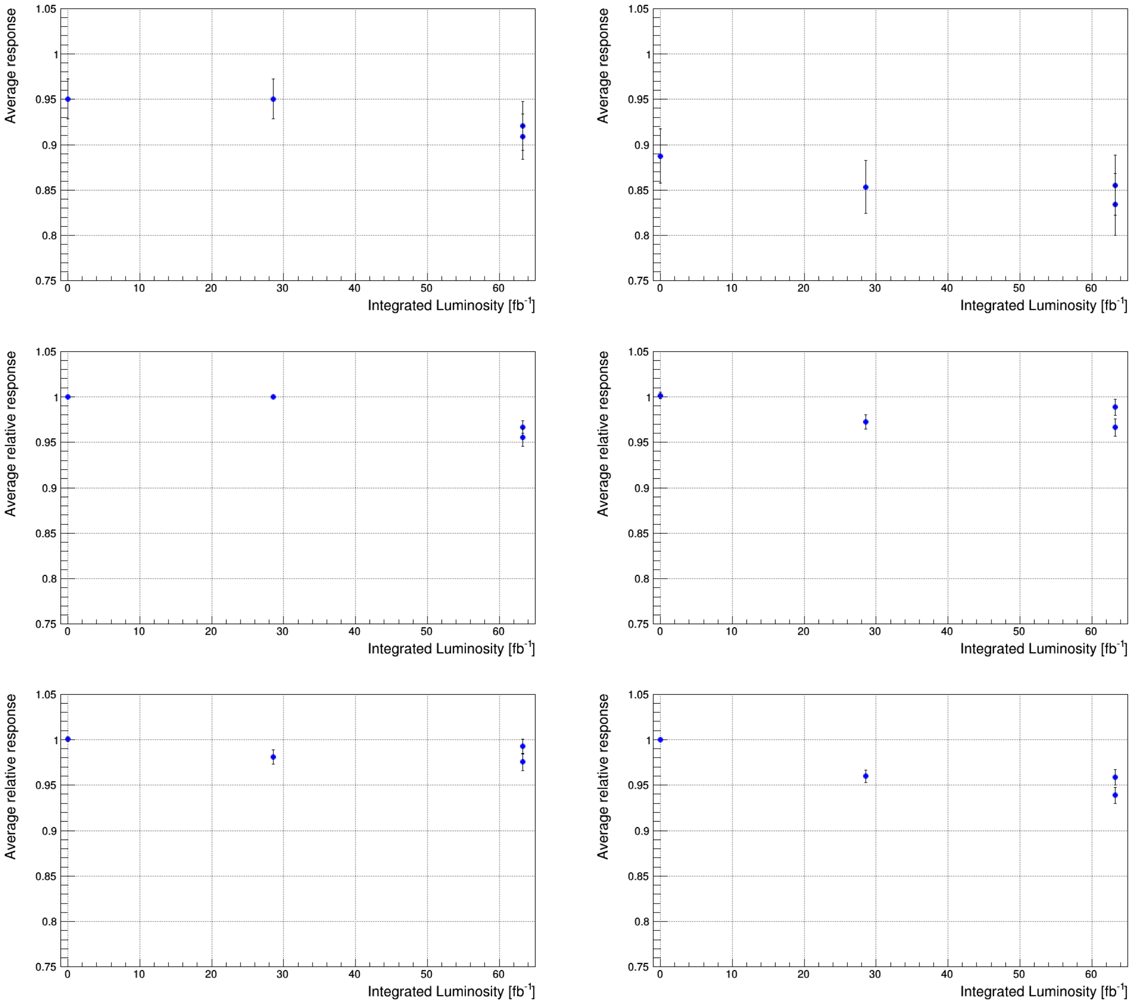

Figure 4.3: Mean of the Gaussian fit to (top) the response to the Cesium, (middle) the relative response to the Cs and (bottom) the relative response to the Laser for (left) the A1 and (right) the A13 cell as a function of the integrated luminosity. The vertical error bars correspond to the standard deviation of the Gaussian fit.

Given Equation 4.15, any difference between the left and right side measurements of $R(tiles{+}fibres)$ is defined as σ_1, which is given by:

$$\sigma_1^2[\%] = E\left[\left(\frac{100\%}{\sqrt{2}}\left(\frac{x_L^{Cs}}{x_L^{Las}} - \frac{x_R^{Cs}}{x_R^{Las}}\right) - \mu_1\right)^2\right] \tag{4.17}$$

where the σ_1 value is the standard deviation, E is the expected value and μ_1 the mean value of a Gaussian fit to the distribution of the quantity $\frac{100\%}{\sqrt{2}}\left(\frac{x_L^{Cs}}{x_L^{Las}} - \frac{x_R^{Cs}}{x_R^{Las}}\right)$ of Equation 4.17 and is around 0.3-0.6% for the EB and LB as shown in Figure 4.4. The $1/\sqrt{2}$ factor is introduced to compensate for the double contribution of the Laser uncertainty in the above equation, associated with the x_L^{Las} and x_R^{Las} measurements.

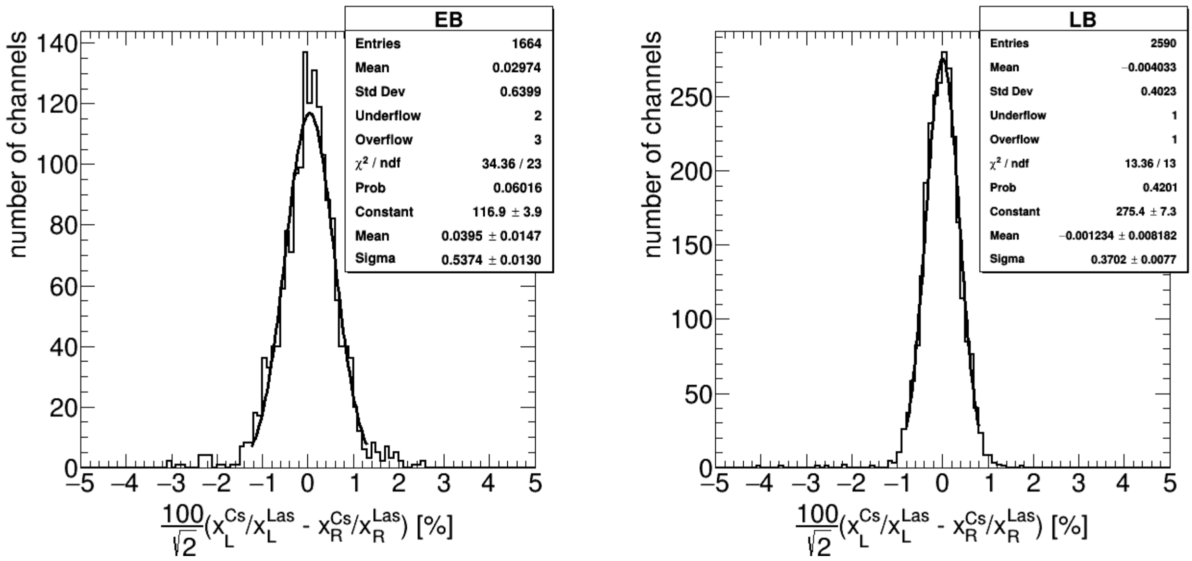

Figure 4.4: Distribution of the difference between the ratio of the left relative response to Cesium and Laser and the ratio of the right relative response to Cesium and to Laser for (left) the Extended Barrel and (right) the Long Barrel for December data. A Gaussian function was adjusted to the data, the parameters of the fit are presented in the plot.

The value of σ_1 has a contribution from the Laser uncertainty and from the Cs uncertainty as well. In order to disentangle their different contributions, the difference between the relative response of the left and right cell readout to the Cs and to the Laser systems were independently analysed using these equations:

$$\sigma_2^2[\%] = E\left[\left(\frac{100\%}{\sqrt{2}}\left(x_L^{Cs} - x_R^{Cs}\right) - \mu_2\right)^2\right] \tag{4.18}$$

$$\sigma_3^2[\%] = E\left[\left(\frac{100\%}{\sqrt{2}}\left(x_L^{Las} - x_R^{Las}\right) - \mu_3\right)^2\right] \tag{4.19}$$

The distribution of these equations are shown in Figure 4.5, σ_2 varies around 0.5-0.7% and σ_3 around 0.6-0.8%.

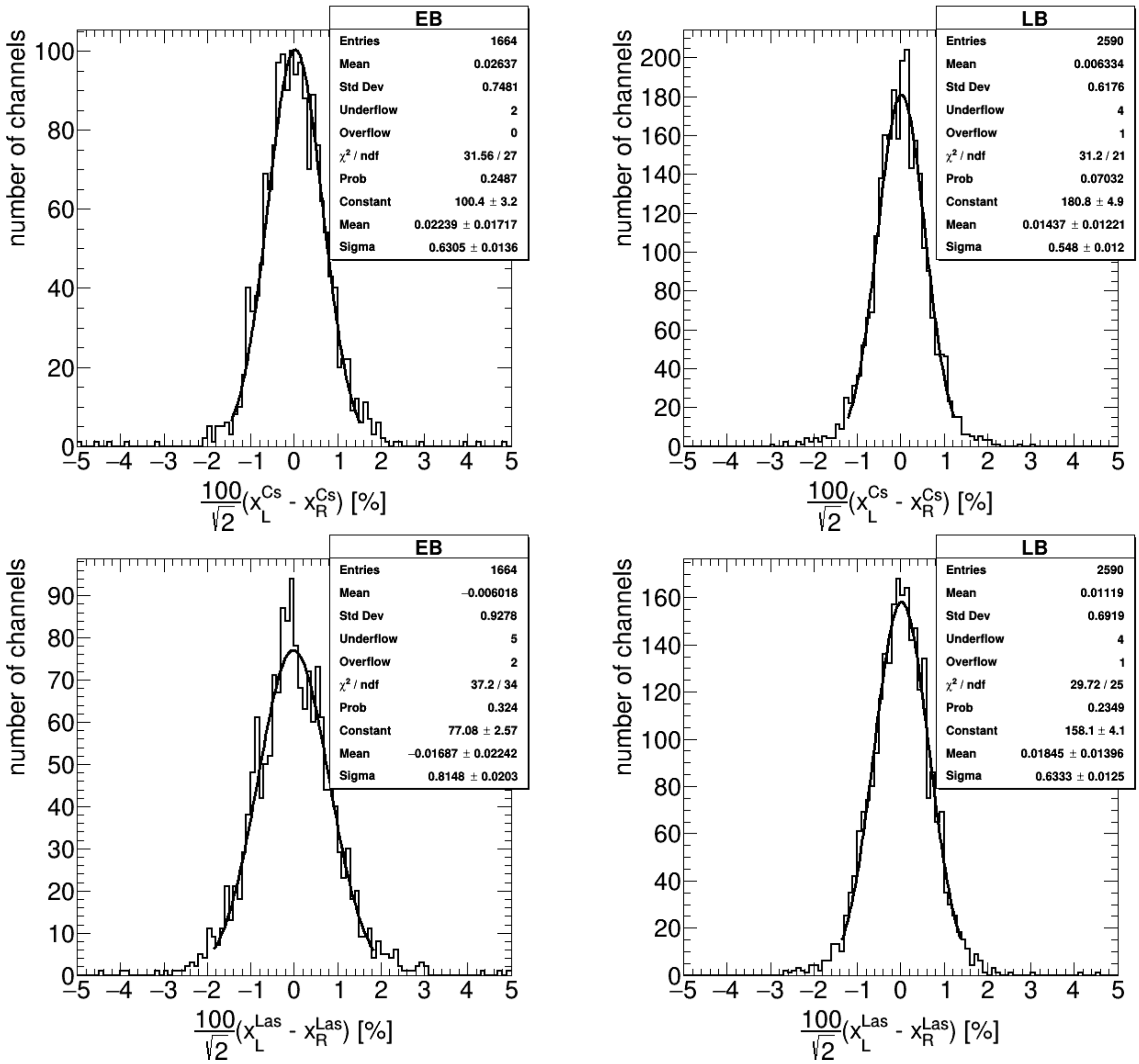

Figure 4.5: Distribution of the difference between the left and right side response to the (top) Cs (Scan=367400) and to the (bottom) Laser (Run=367420) for (left) the Extended Barrel and (right) the Long Barrel. A Gaussian function was adjusted to the data, the parameters of the fit are presented in the plot.

The uncertainties on the Cs and Laser measurements contribute differently to the Equations 4.17, 4.18 and 4.19:

- σ_1 is affected by the uncertainty on the Cs measurement, σ_{Cs}, the uncertainty of the Laser measurement, σ_{Laser}, and the possible difference between the left and right WLS fibres response which we assume negligible.

- σ_2 receives contributions from the uncertainty on the Cs measurement, σ_{Cs}, the real response fluctuations between the left and right PMTs, δ_{PMT}, and the possible difference between the left and right WLS fibres response which we assume negligible.

- σ_3 is by the uncertainty on the Laser measurement, σ_{Laser}, and the real response fluctuations between the left and right PMTs, δ_{PMT}.

We assume no correlation between these factors so that they sum quadratically:

$$\begin{cases} \sigma_1^2 = \sigma_{Cs}^2 + \sigma_{Laser}^2 \\ \sigma_2^2 = \sigma_{Cs}^2 + \delta_{PMT}^2 \\ \sigma_3^2 = \sigma_{Laser}^2 + \delta_{PMT}^2 \end{cases} \tag{4.20}$$

σ_{Laser} is determined from solving the above system of equations. The results obtained for σ_1, σ_2 and σ_3, and σ_{Laser}, with the Cs and Laser data from Table 4.1, are plotted as a function of the integrated luminosity and shown in Figure 4.6. By analysing this Figure, σ_{Laser} increases linearly with the luminosity. Therefore a linear equation was fitted in the Laser uncertainties to derive a parametrisation of these uncertainties with an explicit luminosity dependence. This was derived separately for the Extended and Long Barrels.

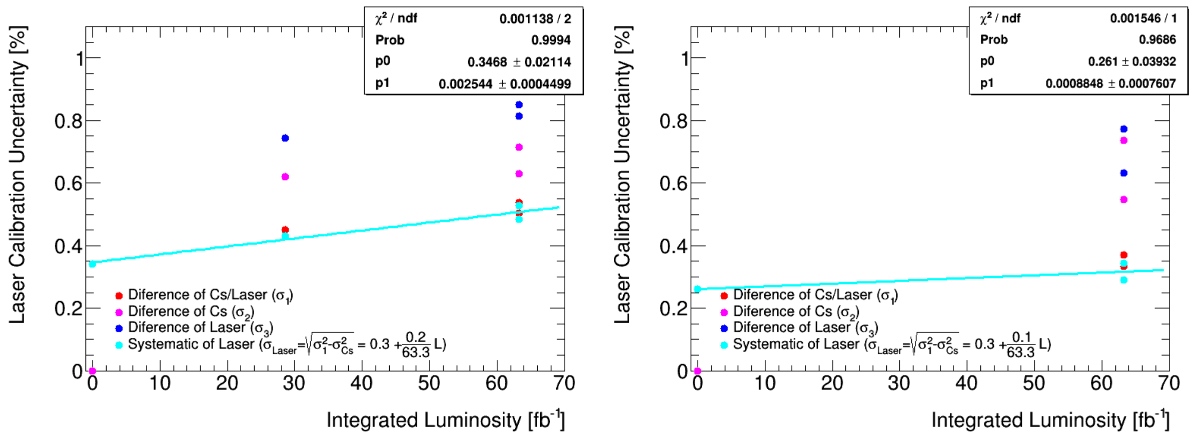

Figure 4.6: The standard deviations σ_1, σ_2 and σ_3, and σ_{Laser} as a function of the integrated luminosity for the (left) Extended Barrel and (right) Long Barrel. A linear equation was fitted to the σ_{Laser} points. The fit result is shown in the plot.

As a cross-check, the study was repeated layer by layer to determine whether the values of uncertainty for the LB and EB were representative of each layer. The results for each layer are shown in Figure 4.7. In the EB, the layer B uncertainty has a smaller dependence on the luminosity than the inclusive uncertainty but this last covers well the separate ones. The same reasoning is made for the LB, so all the layers are well-represented by the EB and LB inclusive equations.

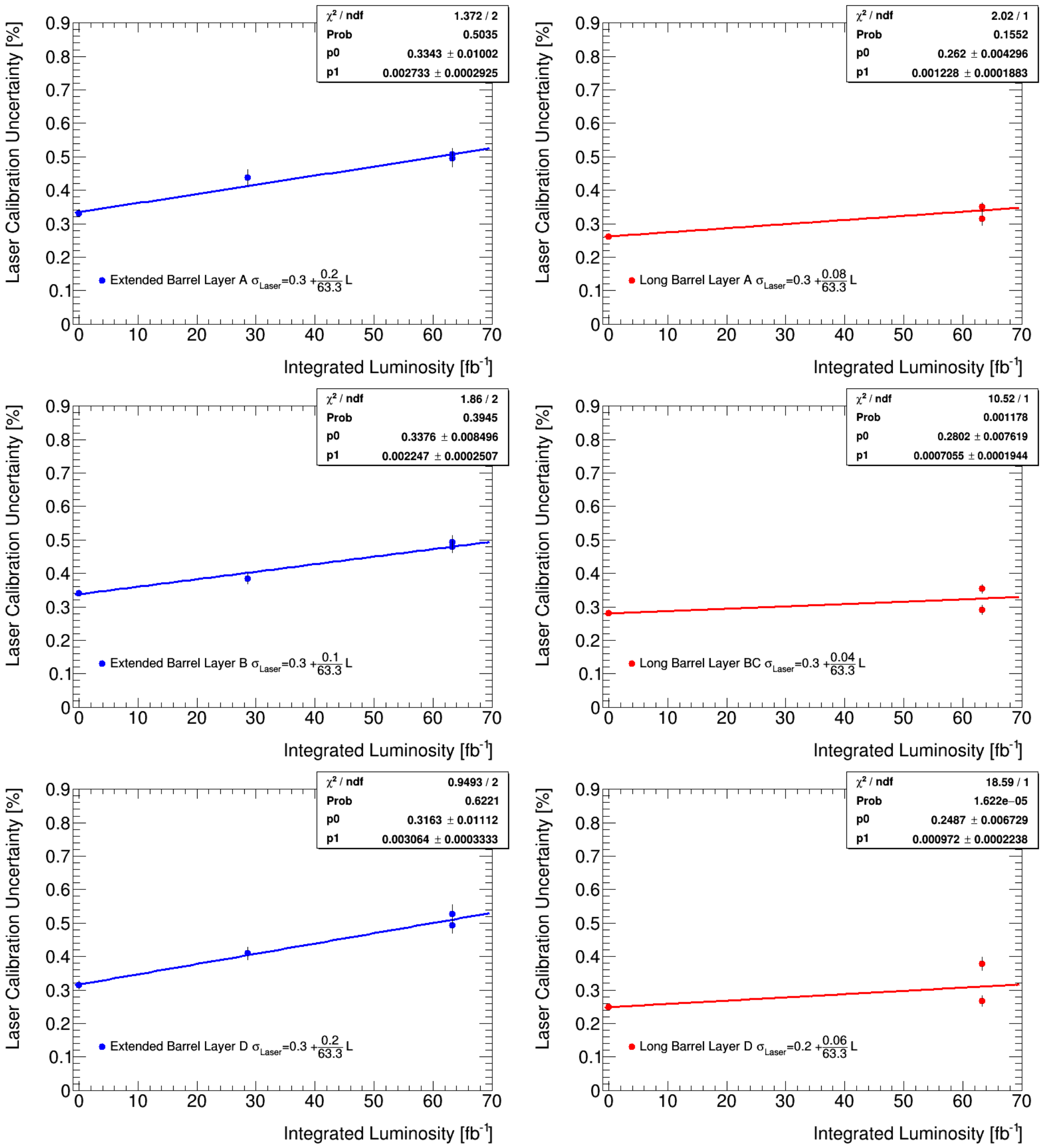

Figure 4.7: Uncertainties on the PMT Laser calibration as a function of the integrated luminosity for the (left) Extended Barrel and for the (right) Long Barrel, splitted into the (top) A, (middle) B/BC and (bottom) D layers.

So, the final uncertainties on the PMT response to the Laser system as a function of the integrated luminosity for the EB, $\sigma^{EB}_{final,Laser}$, and LB, $\sigma^{LB}_{final,Laser}$, separately are presented in Figure 4.8:

$$\sigma^{EB}_{final,Laser} = 0.3 + 0.2/63.3 \times L \tag{4.21}$$

$$\sigma^{LB}_{final,Laser} = 0.3 + 0.1/63.3 \times L \tag{4.22}$$

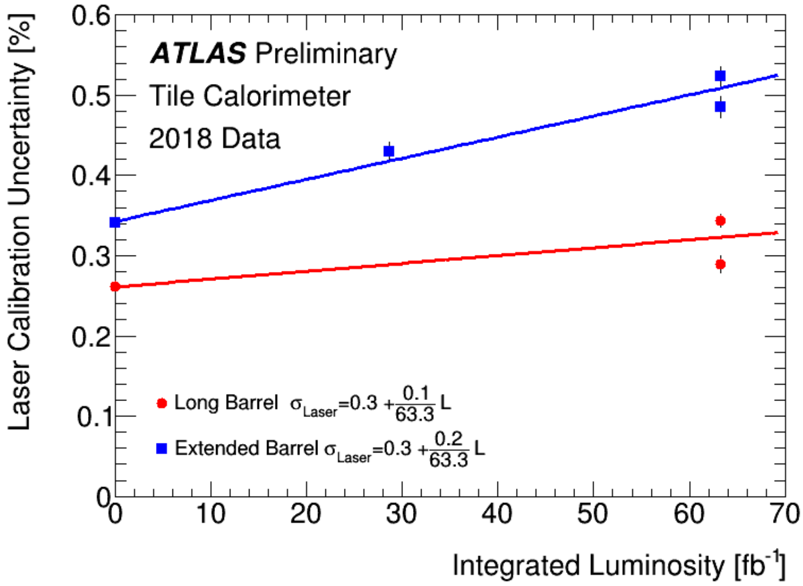

Figure 4.8: Uncertainties on the photomultiplier (PMT) response calibration (in %) with the Laser system, as a function of the integrated delivered luminosity L (in fb^{-1}), for PMTs reading the Long Barrel (LB) in red circles and the Extended Barrel (EB) in blue squares [5].

While this method evaluates uncertainties on the PMT inter-calibration from the comparison between left to right PMT responses, mostly addressing errors introduced by the fibre correction procedure, described in Section 4.2. A global scale systematic would not be captured, if a systematic error were to shift all the PMT responses by a given amount, the relative uncertainty on the PMT determined by this procedure would be the same. In 2015, enough Cs scans were made to have a direct comparison between the Cs and Laser response where the optics degradation effects could be neglected. Studies using the comparison between the PMT response evolution and the calorimeter response evolution measured with the Laser and Cs system in 2015, presented in Figure 4.9, show that the uncertainty on the Laser calibration global scale is no more than 0.4% as given by the standard deviation of the distribution. This last value is summed in quadrature with the results $\sigma_{final,Laser}$ from Equation 4.21 and 4.22. The total uncertainty on the Laser calibration of a single PMT, for the Long Barrel (σ^{LB}_{Laser}) and Extended Barrel (σ^{EB}_{Laser}) yields:

$$\sigma^{EB}_{Laser} = 0.5 + \frac{0.2}{63.3} \times L \tag{4.23}$$

$$\sigma^{LB}_{Laser} = 0.5 + \frac{0.1}{63.3} \times L \tag{4.24}$$

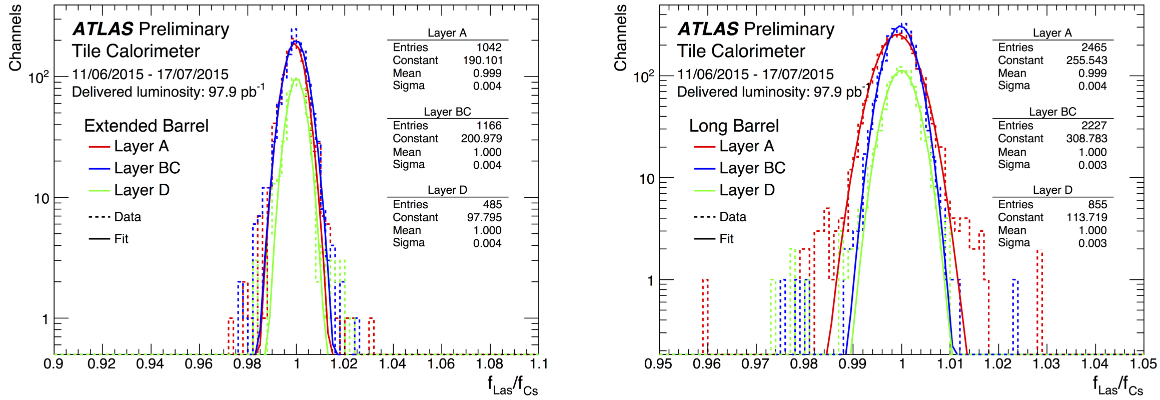

Figure 4.9: Ratio of laser calibration constants over cesium calibration constants for channels in Layer A, BC and D in the (left) Extended Barrel and in the (right) Long Barrel [45].

The PMT uncertainties from Equations 4.23 and 4.24 were determined based on the comparison between the left and right PMT relative response to the Laser and to the Cesium systems, and are uncorrelated across the PMT channels. The total uncertainty, $\sigma_{tot,Laser}$,on the average response of N PMTs should be multiplied by a factor $\frac{1}{\sqrt{N}}$, resulting in:

$$\sigma_{tot,Laser}^{EB} = \sqrt{0.4^2 + (\frac{0.3 + 0.1/63.3 \times L}{\sqrt{N}})^2} \tag{4.25}$$

$$\sigma_{tot,Laser}^{LB} = \sqrt{0.4^2 + (\frac{0.3 + 0.2/63.3 \times L}{\sqrt{N}})^2}. \tag{4.26}$$

The study of the uncertainties on the response to the Laser system was an essential input to the degradation study of the optical components, described in Chapter 5.

Chapter 5

Radiation hardness of the Tile Calorimeter optical components

The current LHC plans foresee a Run 3 and a High Luminosity-LHC (HL-LHC) phase, as described in Section 3.1; that will extend the TileCal lifetime further from the 10 years design goals. Since the optical components cannot be replaced, their radiation hardness must be studied. In this chapter, a measurement of the light yield degradation in Run 2 is presented. These results were then used to model the degradation in terms of total ionising dose and they allowed to extrapolate the expected relative light yield per cell to the end of Run 3 and to the end of the HL-LHC phase.

5.1 Dose simulation

The Total Ionisation Doses (TID) deposited in TileCal were determined with a GEANT4 simulation of the ATLAS detector in the Tile calorimeter region for 50000 $p-p$ generated collisions at the centre-of-mass energy of $\sqrt{s} = 13$ TeV, generated with Pythia 8 [53]. This simulation was developed by the Radiation Simulation working group of ATLAS.

The variation of TID within TileCal is presented in Figure 5.1. The TID is shown as a function of $|z|$ and for different radius intervals and for different density materials: scintillators, steel and a material with the average density of these two materials. As expected, the innermost radial layers have larger TIDs since they are the most exposed to radiation. The dose is larger for the $|z| \sim$ 360 cm within a radial interval between 130 and 280 cm, corresponding to the E cells. The region between 380 $< |z| <$ 480 cm correspond to the A12, A13 and A14 cells of the Extended Barrel, these are the most exposed cells in this Barrel. By analysing the Figure 5.1, the dose is larger for the scintillator material than for steel, in agreement with Equation 2.4. The density of the steel is larger when compared with the scintillator's density, so for the same deposited energy and volume the dose will be larger for the scintillator.

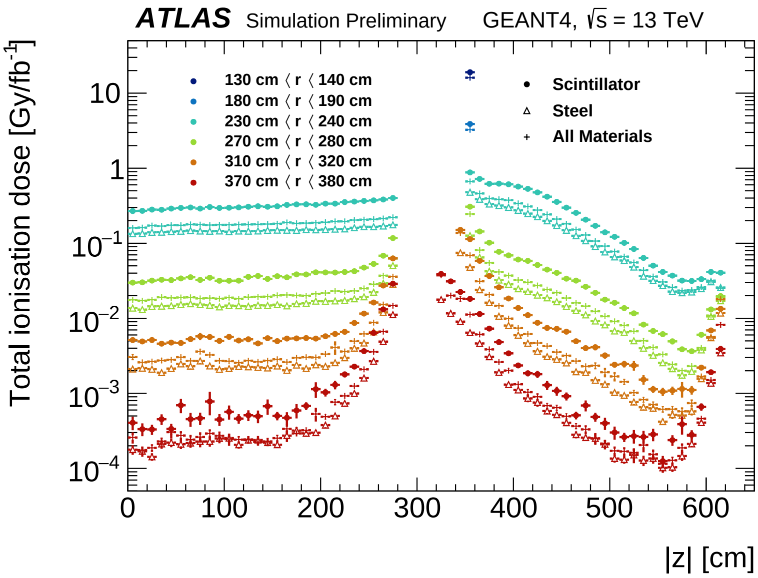

Figure 5.1: Total ionisation dose in Gy/fb^{-1} obtained from a using GEANT4 simulation of the ATLAS detector in the Tile calorimeter region for 50000 $p-p$ generated collisions at the centre-of-mass energy of $\sqrt{s} = 13$ TeV for scintillating tiles, steel absorbers and all materials as average dose from the sum of individual doses as a function of $|z|$ for different r values [53].

The dose was simulated in bins of 4 cm × 4 cm in the z × r plan. This map is presented in Figure 5.2, the colour represents the value of the simulated TID per fb^{-1} of $p-p$ collisions and can be used as conversion factors from integrated luminosity to dose. Given the dose spread within the cell volume, the dose conversion factors were determined for each cell by averaging the dose values over the bins belonging to the cell. The dose distribution for the A13 cell is presented in Figure 5.3, the simulated dose ranges between 0.1 and 1 Gy/fb^{-1}, the average cell dose is around 0.4 Gy/fb^{-1} and the RMS is around 0.2 Gy/fb^{-1} represents the spread of the dose within the large cell volume. The dose distribution for each cell is presented in the Appendix A.

The TID in a given cell is obtained by multiplying the integrated luminosity by the dose conversion factor for the cell. The dose for the A13 for an integrated luminosity of 158.1 fb^{-1} (end of Run 2) is 67 Gy. The average cell dose conversion factors for the Run 2, Run 3 and HL-LHC run conditions are shown in Figure 5.4, 5.5 and 5.6, respectively. The dose maps are different for each Run depending on the ATLAS detector geometry. In particular, upgrades in the inner detector and the LAr calorimeter, that are placed between the beam pipe and the TileCal, imply a difference in the material in front of the scintillators of the TileCal in these three run periods. Nevertheless, the dose conversion factors are very similar in between Runs. The TID in layer A ranges from 32 to 556 mGy/fb^{-1}, in the layer BC is between 5 and 179 mGy/fb^{-1}, in the D layer it ranges from 0.7 to 63 mGy/fb^{-1}.

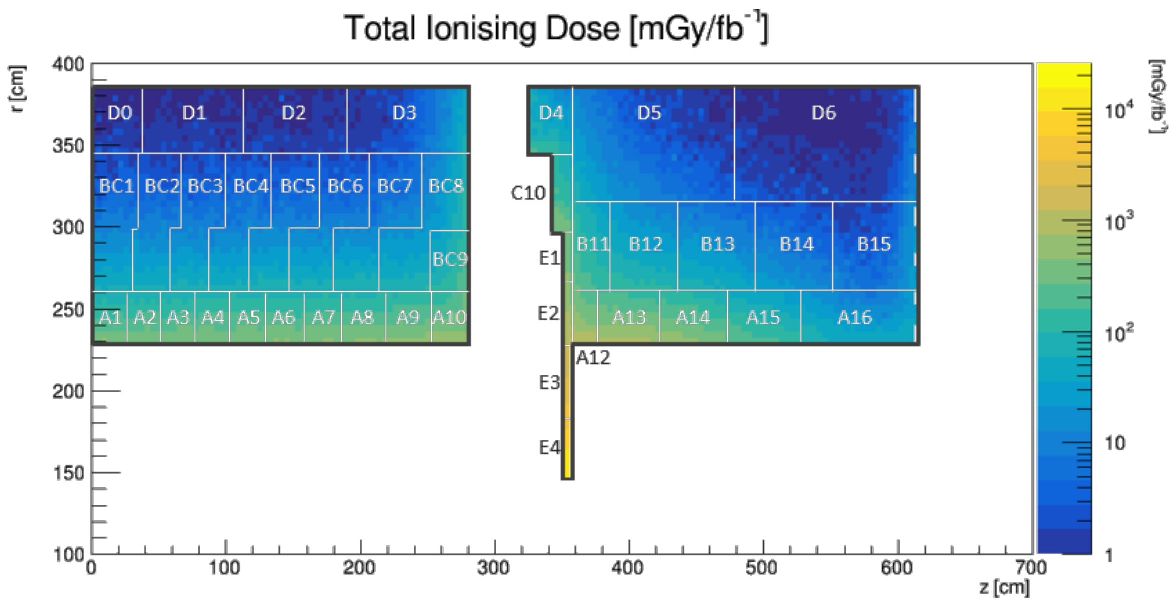

Figure 5.2: The total ionisation dose, obtained in bins of 4 cm $\times$ 4 cm, using GEANT4 simulation of the ATLAS detector in the Tile calorimeter region for 50000 $p-p$ generated collisions at the centre-of-mass energy of $\sqrt{s} = 13$ TeV, as a function of the radial r and z distance at the end of Run 2. The schematic of the TileCal readout was overlap.

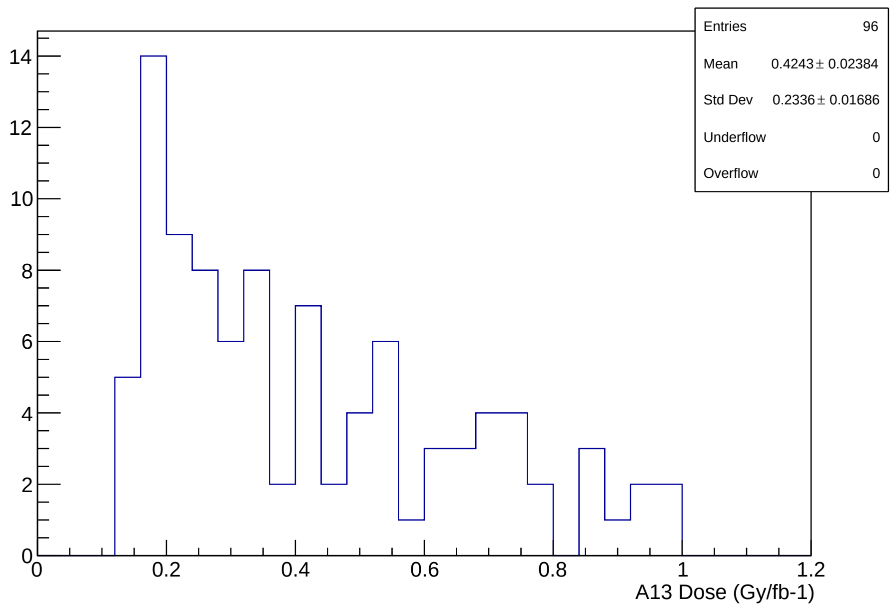

Figure 5.3: Distribution of the dose values, obtained in bins of 4 cm $\times$ 4 cm, using GEANT4 simulation of the ATLAS detector in the Tile calorimeter region for 50000 $p-p$ generated collisions at the centre-of-mass energy of $\sqrt{s} = 13$ TeV, for the A13 cell.

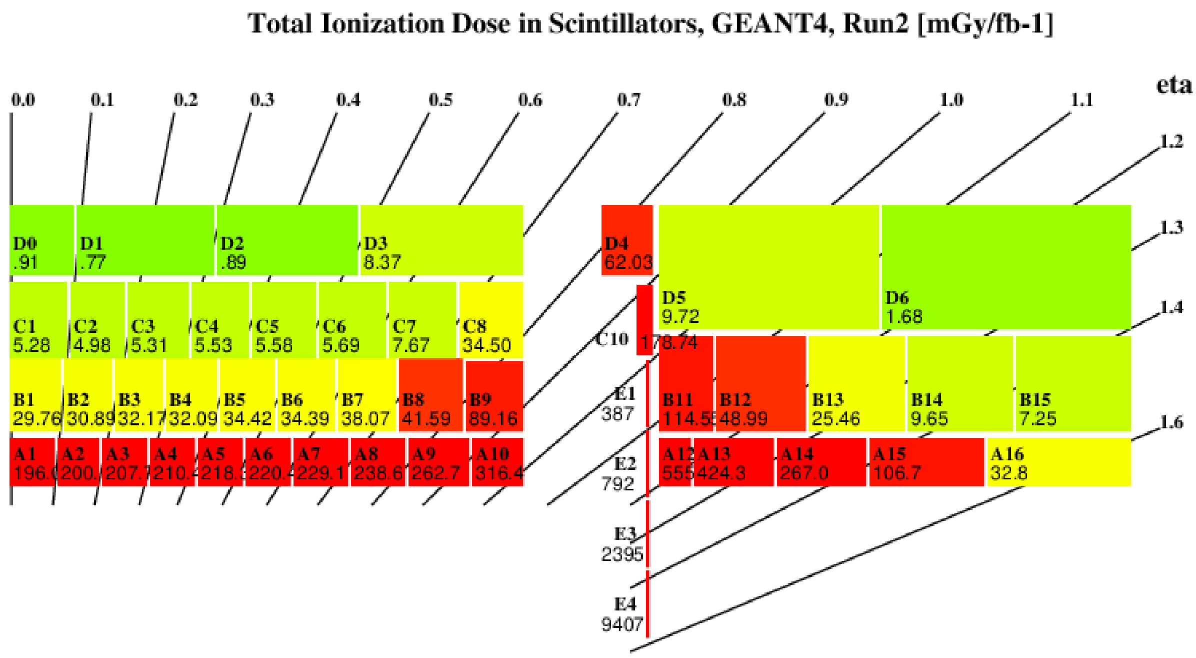

Figure 5.4: Average ionisation dose conversion factor per TileCal cell determined using GEANT4 simulation of the ATLAS detector in the Tile calorimeter region for 50000 $p-p$ generated collisions at the centre-of-mass energy of $\sqrt{s} = 13$ TeV. The ATLAS detector was simulated with geometry corresponding to the Run 2 operation.

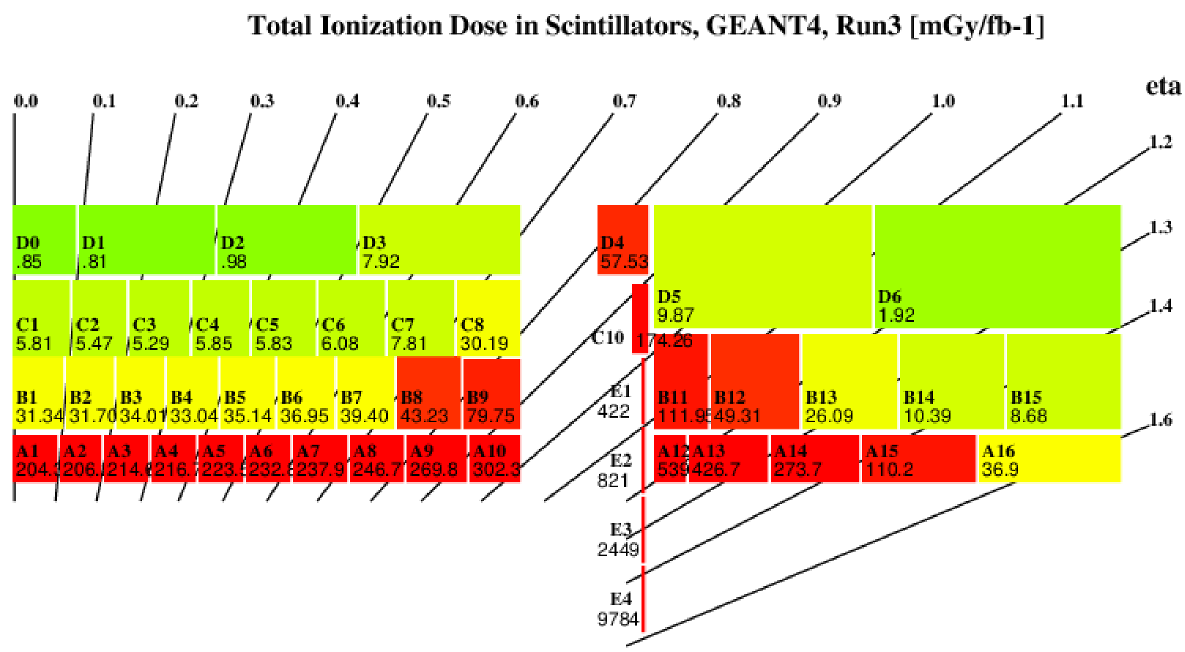

Figure 5.5: Average ionisation dose conversion factor per TileCal cell determined using GEANT4 simulation of the ATLAS detector in the Tile calorimeter region for 50000 $p-p$ generated collisions at the centre-of-mass energy of $\sqrt{s} = 13$ TeV. The ATLAS detector was simulated with geometry corresponding to the Run 3 operation.

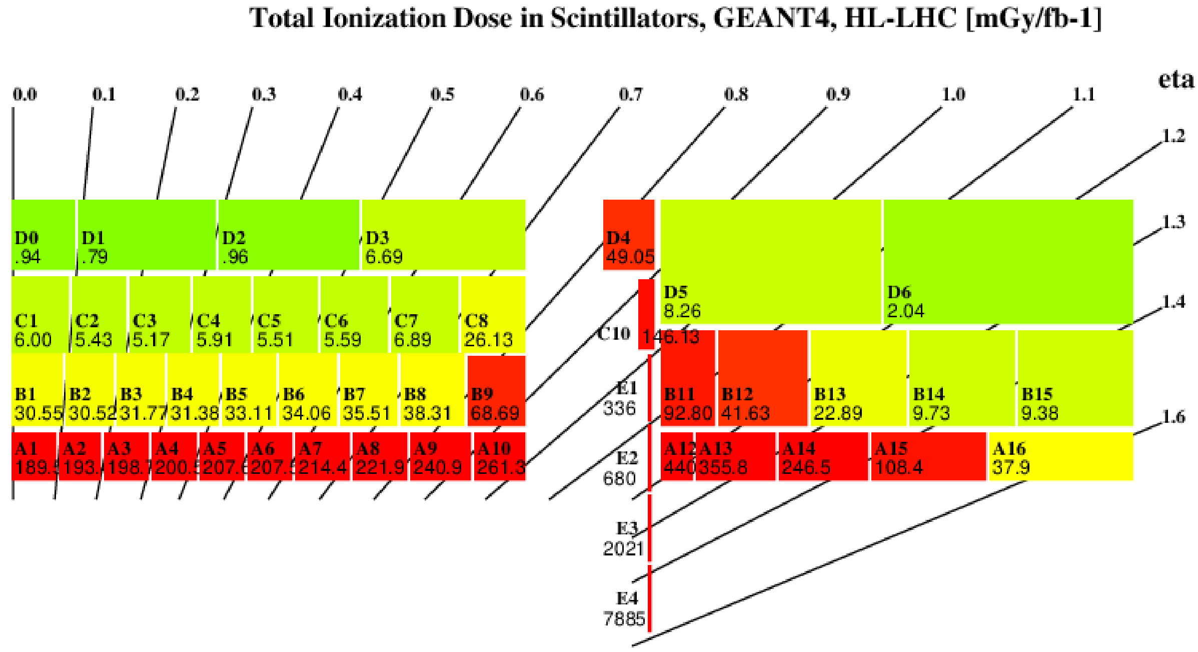

Figure 5.6: Average ionisation dose conversion factor per TileCal cell determined using GEANT4 simulation of the ATLAS detector in the Tile calorimeter region for 50000 $p-p$ generated collisions at the centre-of-mass energy of $\sqrt{s}=13$ TeV. The ATLAS detector was simulated with geometry corresponding to the HL-LHC operation.

5.2 Relative light yield of scintillators and fibres

The average deviation of a cell's response to the Cs (Δx^{Cs}) and to the Laser (Δx^{Las}) calibration systems are presented in Figures 3.14 and 3.13, respectively. At the end of Run 2, the response to the Cs for the A layer decreased by about 10% and the response of the PMTs reading the A layer to the to the Laser has reduced about 4%. This difference between the cell's response to the Cs and the PMT's response to the Laser corresponds to a degradation of about 6% of the scintillators and fibres response, caused by dose exposure. Therefore, by subtracting the two relative responses variations, we can measure the optical response. We define the relative light yield (I/I_0) of the cell's scintillators and fibres as:

$$I/I_0 = 1 + \frac{\Delta x^{Cs} - \Delta x^{Las}}{100\%}. \tag{5.1}$$

The relative light yield is calculated concerning the beginning of each collision campaign per year, independently per each year in Run 2 — 2015 to 2018. The accumulated relative light yield from 2015 to 2018 is obtained by combining the per year measurement. To take into account the loss of the relative light yield from the previous year, the relative light yield of the next year is multiplied by the relative light yield at the end of the year before: $I/I_{0_{year}} \times I/I_{0_{year-1}}^{final}$. For example, if the relative light yield of 2015 is 0.50 and for 2016 is 0.50, the relative light yield at the end of 2016 is 0.25. Table 5.1 presents the Cs data used in this analysis, including information about the beggining of the $p-p$ collisions, the $p-p$

integrated luminosity at the time of each Cs scan and the yearly reference scan used in the I/I_0 measurement. The Laser runs are chosen to be as close as possible from the Cs scans, and typically there is a Laser run within a few hours from a Cs scan.

Table 5.1: Cesium Scan number, date and integrated luminosity of the data analysed to determine the relative light yield.

Cs Scan number	Date	Integrated Luminosity [fb^{-1}]	Comment
270000	17 July 2015	0	Reference scan for 2015
$p-p$ collision start on 17 July 2015			
284600	3 November 2015	4.1	
294144	2 April 2016	4.2	
295683	15 April 2016	4.2	
$p-p$ collision start on 18 April 2016			
300300	24 May 2016	5.0	Reference scan for 2016
317200	6 March 2017	44.5	Reference scan for 2017
$p-p$ collision start on 22 May 2017			
342550	17 February 2018	94.8	Reference scan for 2018
$p-p$ collision start on on 16 May 2018			
356509	25 July 2018	123.4	
365480	27 October 2018	158.1	
367400	3 December 2018	158.1	

Some cells, in particular modules, have a different geometry than the regular cell map. In these cases, the deposited dose and their degradation is not the same as the cells with typical geometry. For this reason, these cells were excluded from the analysis:

- Minimum bias trigger scintillators — modules EBA/EBC 39-42 and 55-58 from PMT 5 (channel 4);
- Special C10 cells with a smaller size than regular C10 cells — modules EBA/EBC 39-42 and 55-58 from PMT 6 (channel 5);
- Special D4 cells with a smaller size than regular D4 cells — modules EBA/EBC 14, 15, 18, 19;

- D4 cells which are not shielded from special neighbouring D4 cells — modules EBA/EBC 13, 16, 17, 20;
- Special D5, where D4 readout is merged to D5 — modules EBA 15 and EBC 18.

Figure 5.7 shows the relative light yield of the A13 cell as a function of the simulated dose, obtained by multiplying the integrated luminosity, at each point, by the dose conversion factor introduced in Section 5.1. Given that the last two values of the relative light yield are measured for the same dose value, as can be seen in Table 5.1, they were averaged so that the statistical weight for this dose point is not larger than for the remaining points. The vertical width of the yellow band in this figure represents the systematic uncertainties on the relative light yield, where the Cesium systematics have a contribution of $\sim$0.5%, and the Laser uncertainties have a dependence with the luminosity as discussed in Section 4.3. These uncertainties are added in quadrature to determine the total uncertainty on I/I_0. The horizontal band in the dose axis represents the spread of the dose estimate within the large cell volume and corresponds to the RMS of the dose distribution within the cell, as shown in Figure 5.3. For the A13 cell the dose spread for an integrated luminosity of 158.1 fb^{-1}, at the end of Run 2, is 36.93 Gy. Data from 2015 to 2018 is presented with different markers and colours per year. The integrated luminosity increases with the year, so as the accumulated dose. But the light yield decreases since the scintillators will be exposed to more dose. The relative light yield for 2015 is stable around 1 and no degradation is observed for the 1,8 Gy of accumulated dose in the year. In the following years, from 2016 to 2018, the accumulate dose per year is similar, around 25 Gy/year, and the optics degradation ranges from 3 to 4% per year.

In Figure 5.7, the black vertical lines represent the expected dose by the end of Run 3 (assuming an integrated luminosity of 350 fb^{-1}) and HL-LHC (assuming 4000 fb^{-1}). White squares and triangles markers are data from bare scintillators irradiated with photons from a ^{137}Cs source at a dose rate of 60 mGy/s [21] and 4 mGy/s [36], respectively. Black squares are data from scintillators irradiated at a dose rate of 20 to 30 mGy/s with secondary hadrons from proton beam interaction with Aluminium target [21]. These irradiations were done to study the radiation hardness of scintillators during the TileCal design. However, the TileCal A layer cells have a typical dose rate between 1 and 10 mGy/h [54], which is much smaller than the dose rate of the irradiations of bare scintillators at the laboratory. Focusing on the region between 1 and 0.9 of the relative light yield in Figure 5.7, and comparing the A13 data with the laboratory results when the light yield loss is the same, we see that the dose is larger for the laboratory irradiations. So the degradation of the TileCal cells looks faster than the laboratory results indicated. This could be due to the impact of the dose rate effects on the degradation of scintillators. Another difference is the fact that in TileCal we measure the degradation of a cell — an ensemble of tiles and fibres — subject to an irregular dose profile, while the irradiations at laboratory test single scintillators received an uniform dose profile.

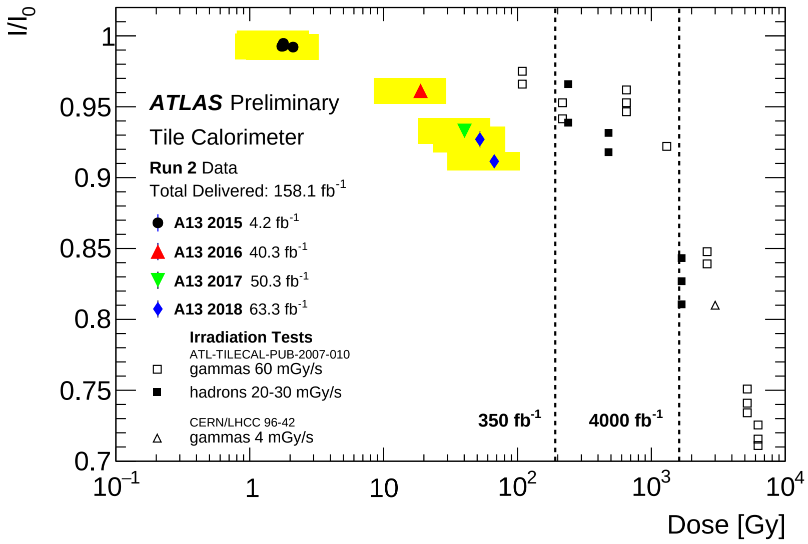

Figure 5.7: The measured relative light yield for the A13 cell as a function of the simulated dose in Run 2. The vertical errors are associated to the precision of the Cs (∼0.5%) and Laser systems, and the horizontal band corresponds to the dose spread within the large cell volume. The square markers are data from bare scintillators irradiated in the labs before the calorimeter construction [4].

It is expected that the innermost layer A will reach a smaller relative light yield value since they are the closest cells to the beam pipe and so more exposed to the particle fluence. The relative light yield at the end of Run 2 is shown in Figure 5.8 for all the TileCal cells. The relative uncertainty, $\frac{\Delta(I/I_0)}{I/I_0} \times 100\%$, is about 1% for all the cells, with the contribution of the Laser and Cs uncertainties. As expected, the cells more exposed to radiation, such as the A layer cells, and B9, B11, B12, C10 and D4 cells, have a larger loss in light yield, of the order of 5%. For the other cells, the degradation is 1%, and the current precision of the measurement does not allow to conclude on their damage.

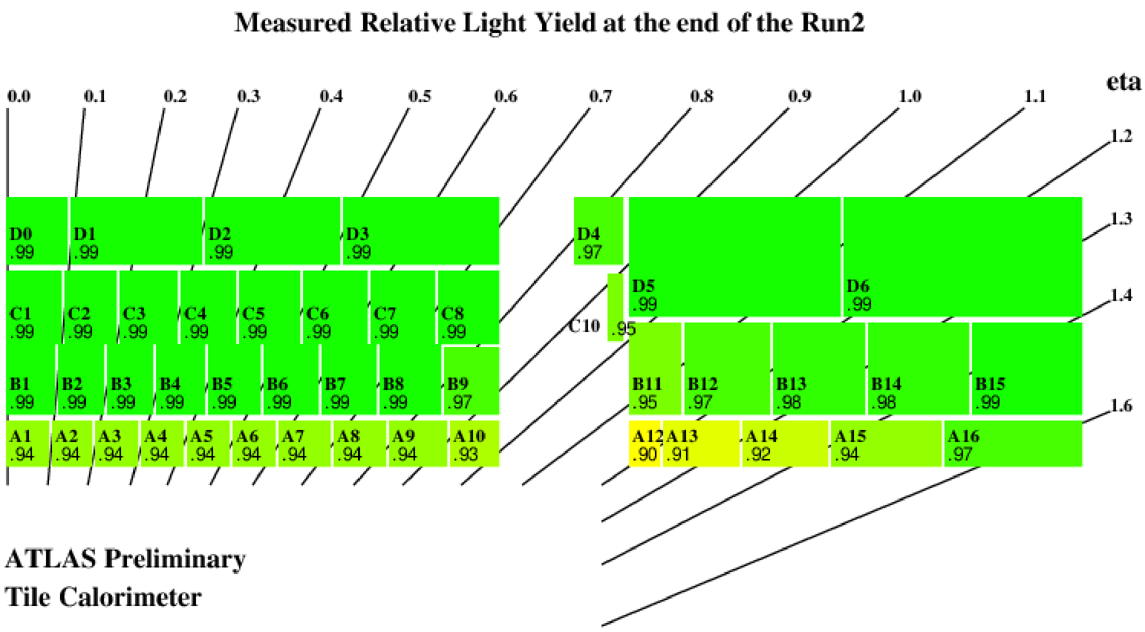

Figure 5.8: The measured relative light yield of the TileCal cells at the end of Run 2 [4, 8].

5.3 Model of the relative light yield as a function of dose

The current plan of the LHC operation will lead to the Run 3 and the High Luminosity phase at the LHC with an expected integrated luminosity of 350 fb^{-1} and 4000 fb^{-1}, respectively. With the luminosity increasing, the cells of the TileCal will be exposed to a higher dose and will degrade more. It is important to understand and model the radiation hardness of Tilecal in order to estimate its performance during these phases. As a first approximation, given the large uncertainties, we approximate the degradation of a TileCal cell with dose to a simple exponential function given by:

$$I/I_0 = e^{p_0 - dose/p_1} \tag{5.2}$$

the parameters p_0 give information on how consistent is the fit and p_1 represent the dose value for which the cell light yield reaches 37%, respectively. The exponential model fits well since the light output of the scintillator, typically, decreases exponentially with the receiving dose [16]. By using the RMS of the dose distribution as a dose uncertainty representing the tile exposure extreme cases, this model can be used. The exponential model was fitted to the Run 2 measurements, and the parameters were determined from data with the χ^2 method. The impact of the I/I_0 uncertainties and the dose spread on the fit parameters uncertainty is evaluated from the following three fits:

- The nominal fit, $e^{p_0 - dose/p_1}$, is done by adjusting to the set of points $\{I/I_0, dose\}$ composed of the nominal I/I_0 and average cell dose values;
- The upper variation fit, $e^{p_{0,up} - dose/p_{1,up}}$, is done by adjusting to the set of points $\{I/I_{0,up}, dose_{up}\}$ composed of the upwards uncertainty variation $I/I_0 + \Delta I/I_0$ and the RMS upwards variation of the average dose estimate;
- The down variation fit, $e^{p_{0,do} - dose/p_{1,do}}$, is done by adjusting to the set of points $\{I/I_{0,do}, dose_{do}\}$ composed of the downwards uncertainty variation $I/I_0 - \Delta I/I_0$ and the RMS lower variation of the average dose estimate;

The uncertainties on the function parameters were calculated as follows:

- The average difference between the nominal and the upper/lower fit parameters: $\delta p_1 = ((p_{1,up} - p_1) + (p_1 - p_{1,do}))/2$ and $\delta p_0 = ((p_{0,up} - p_0) + (p_0 - p_{0,do}))/2$;
- The final uncertainty corresponds to the quadratic sum between the δp and the uncertainty on the nominal fit δp_{nom}: $\Delta p_0^2 = \delta p_0^2 + \delta p_{0,nom}^2$ and $\Delta p_1^2 = \delta p_1^2 + \delta p_{1,nom}^2$.

The results for representative cells of the Long and Extended Barrel and the different layers are presented in Figures 5.9 and 5.10. The parameter values and the uncertainties of the nominal fit are presented in the plots as well as the resulting three fits: nominal in black solid line and upper and lower in black dashed line.

Table 5.2 shows the values of the model parameters for each cell. The p_0 value is compatible with 0 within the uncertainties for all the cells, as expected. p_1 spans from 13 to 840 Gy indicating that the

TileCal cells are degrading at different rates. Many factors can contribute to this, one of which is the rate at which the dose is accumulated by the cell.

Previous studies (see Subsection 2.2.1) have shown that the degradation not only depends on the absorbed dose but also on the dose rate, indicating that for smaller dose rate values, the degradation would occur more rapidly. In the simple exponential model, the larger the p_1 value the smaller the degradation rate, for it means that more dose must be accumulated to reach 37% light yield degradation. To study the possible impact of the dose rate effects, the fit parameter p_1 is plotted as a function of the dose conversion factors in Gy/fb^{-1} for the most degraded cells in Figure 5.11. The dose conversion factors are a good proxy for dose rate since they are directly proportional to each other: in order to obtain the dose rate, one just needs to multiply the dose conversion factor, in Gy/fb^{-1}, by the instantaneous luminosity at the LHC, in fb^{-1}/s. The results show that p_1 increases with dose rate, and so, the degradation rate decreases with the dose rate. Taking into account the large uncertainties, the conclusions are less clear. Nevertheless, if the uncertainties on the p_1 values have a purely systematic nature, we could conclude that the dose rate has an impact on the degradation of the scintillators.

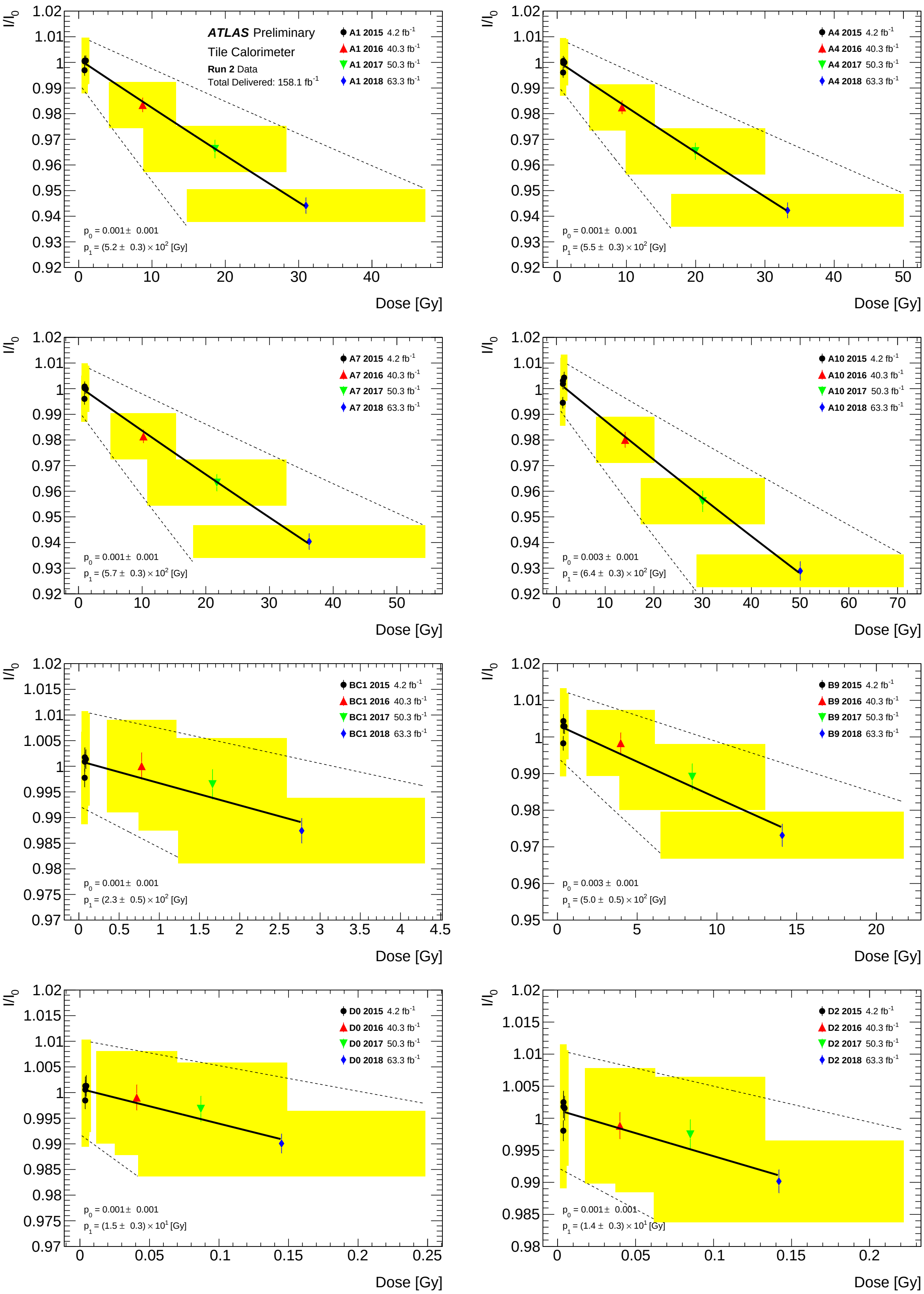

Figure 5.9: The relative light yield for the A1, A4, A7, A10, BC1, B9, D0 and D2 cells bellonging to the Long Barrel as a function of the simulated dose during the LHC Run 2. The solid black line is the exponential fit to the data, with the dashed black lines corresponding to the fit to the up and down uncertainty variations. The plots with the ATLAS Preliminary label can be viewed in [4].

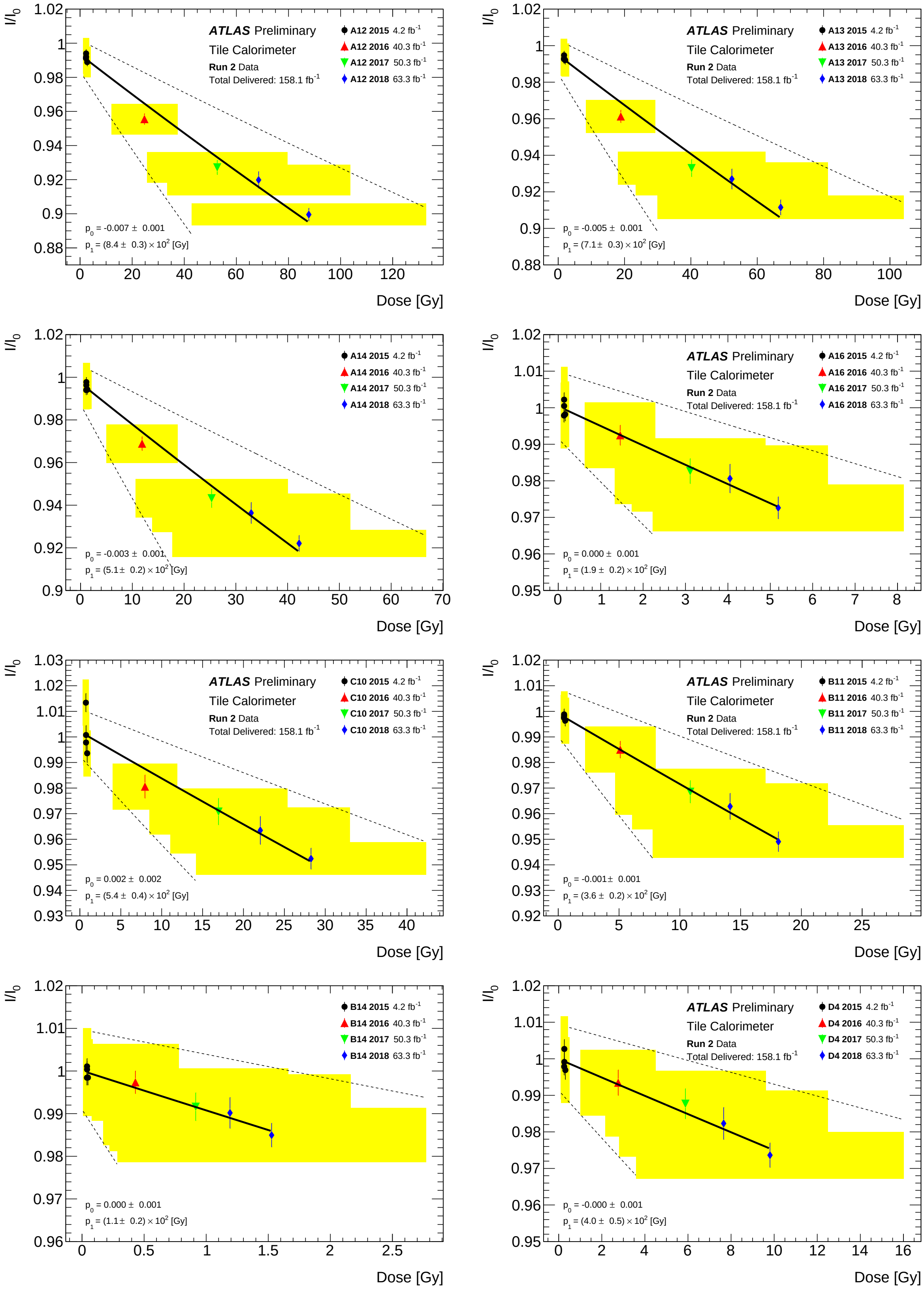

Figure 5.10: The relative light yield for the A10, A12, A13, A14, A16, C10, B11, B14 and D4 cells bellonging to the Extended Barrel as a function of the simulated dose during the LHC Run 2. The solid black line is the exponential fit to the data, with the dashed black lines corresponding to the fit to the up and down uncertainty variations. The plots with the ATLAS Preliminary label can be viewed in [4].

Table 5.2: Values of the exponential fit parameters (p_0 and p_1), of the simulated dose (D) and measured relative light at the end of Run 2 (I/I_0), and of the expected dose and the relative light yield (I/I_0) at the end of Run 3 (assuming 350 fb^{-1}) and HL-LHC assuming 4000 fb^{-1}.

			End Run 2		End Run 3		End HL-LHC	
cell	p0	p1 [Gy]	D [Gy]	I/I_0	D [Gy]	I/I_0	D [Gy]	I/I_0
A1	0.00±0.01	(5.2±2.6)10^2	31.0	0.94±0.01	70.3	0.88±0.05	828.7	0.21±0.15
A2	0.00±0.01	(5.2±2.5)10^2	31.6	0.94±0.01	71.3	0.87±0.05	845.0	0.20±0.14
A3	0.00±0.01	(5.3±2.6)10^2	32.8	0.94±0.01	74.1	0.87±0.05	869.0	0.20±0.14
A4	0.00±0.01	(5.5±2.6)10^2	33.3	0.94±0.01	74.9	0.87±0.05	877.1	0.20±0.14
A5	0.00±0.01	(5.6±2.7)10^2	34.5	0.94±0.01	77.5	0.87±0.05	907.9	0.20±0.14
A6	0.00±0.01	(5.5±2.7)10^2	34.8	0.94±0.01	79.6	0.87±0.05	910.0	0.19±0.14
A7	0.00±0.01	(5.7±2.7)10^2	36.2	0.94±0.01	82.0	0.87±0.05	939.6	0.19±0.14
A8	0.00±0.01	(5.8±2.8)10^2	37.7	0.94±0.01	85.1	0.87±0.05	972.8	0.19±0.14
A9	0.00±0.01	(6.0±2.9)10^2	41.5	0.94±0.01	93.4	0.86±0.05	1057.2	0.17±0.14
A10	0.00±0.01	(6.4±2.6)10^2	50.0	0.93±0.01	107.9	0.85±0.05	1153.5	0.17±0.12
A12	-0.01±0.01	(8.4±4.3)10^2	87.8	0.90±0.01	191.3	0.79±0.07	1952.9	0.10±0.12
A13	-0.01±0.01	(7.1±4.0)10^2	67.1	0.91±0.01	149.0	0.81±0.07	1572.2	0.11±0.13
A14	-0.00±0.01	(5.1±2.9)10^2	42.2	0.92±0.01	94.8	0.83±0.07	1080.8	0.12±0.14
A15	-0.00±0.01	(2.9±1.7)10^2	16.9	0.94±0.01	38.1	0.88±0.05	471.7	0.20±0.16
A16	0.00±0.01	(1.9±1.0)10^2	5.2	0.97±0.01	12.3	0.94±0.03	164.0	0.41±0.15
BC1	0.00±0.01	(2.3±1.0)10^2	2.8	0.99±0.01	6.3	0.97±0.02	79.5	0.71±0.08
BC2	0.00±0.01	(2.7±1.2)10^2	2.8	0.99±0.01	6.4	0.98±0.02	78.3	0.75±0.08
BC3	0.00±0.01	(2.6±1.2)10^2	3.0	0.99±0.01	6.7	0.98±0.02	80.7	0.74±0.08
BC4	0.00±0.01	(2.7±1.3)10^2	3.0	0.99±0.01	6.7	0.98±0.02	81.3	0.74±0.08
BC5	0.00±0.01	(2.5±1.1)10^2	3.2	0.99±0.01	7.1	0.97±0.02	84.4	0.72±0.08
BC6	0.00±0.01	(2.5±1.2)10^2	3.2	0.99±0.01	7.3	0.97±0.02	86.6	0.71±0.09
BC7	0.00±0.01	(3.2±1.5)10^2	3.6	0.99±0.01	8.2	0.98±0.02	93.0	0.75±0.08
BC8	0.00±0.01	(4.6±2.5)10^2	6.0	0.99±0.01	13.1	0.97±0.02	142.0	0.74±0.09
B9	0.00±0.01	(5.0±2.4)10^2	14.1	0.97±0.01	29.3	0.95±0.03	304.1	0.55±0.12
C10	0.00±0.01	(5.4±2.6)10^2	28.3	0.95±0.01	61.7	0.89±0.04	646.2	0.30±0.15
B11	-0.00±0.01	(3.6±2.0)10^2	18.1	0.95±0.01	39.6	0.89±0.04	410.8	0.32±0.16
B12	-0.00±0.01	(2.6±1.7)10^2	7.7	0.97±0.01	17.2	0.94±0.03	183.8	0.50±0.16
B13	0.00±0.01	(2.0±1.4)10^2	4.0	0.98±0.01	9.0	0.96±0.03	100.6	0.61±0.15
B14	0.00±0.01	(1.1±0.8)10^2	1.5	0.98±0.01	3.5	0.97±0.02	42.5	0.67±0.13
B15	0.00±0.01	(1.0±0.8)10^2	1.1	0.99±0.01	2.8	0.97±0.02	40.4	0.67±0.13
D0	0.00±0.01	(1.5±0.8)10^1	0.1	0.99±0.01	0.3	0.98±0.02	4.1	0.76±0.09
D1	0.00±0.01	(1.3±0.5)10^1	0.1	0.99±0.01	0.3	0.98±0.02	3.4	0.77±0.07
D2	0.00±0.01	(1.4±0.6)10^1	0.1	0.99±0.01	0.3	0.98±0.02	4.2	0.74±0.08
D3	0.00±0.01	(2.3±1.7)10^2	1.3	0.99±0.01	2.8	0.99±0.01	29.6	0.88±0.06
D4	-0.00±0.01	(4.0±2.4)10^2	9.8	0.97±0.01	20.8	0.95±0.03	217.1	0.58±0.14
D5	-0.00±0.01	(1.3±1.4)10^2	1.5	0.99±0.01	3.4	0.97±0.02	36.5	0.76±0.12
D6	0.00±0.01	(2.6±2.9)10^1	0.3	0.99±0.01	0.6	0.98±0.02	8.8	0.71±0.15

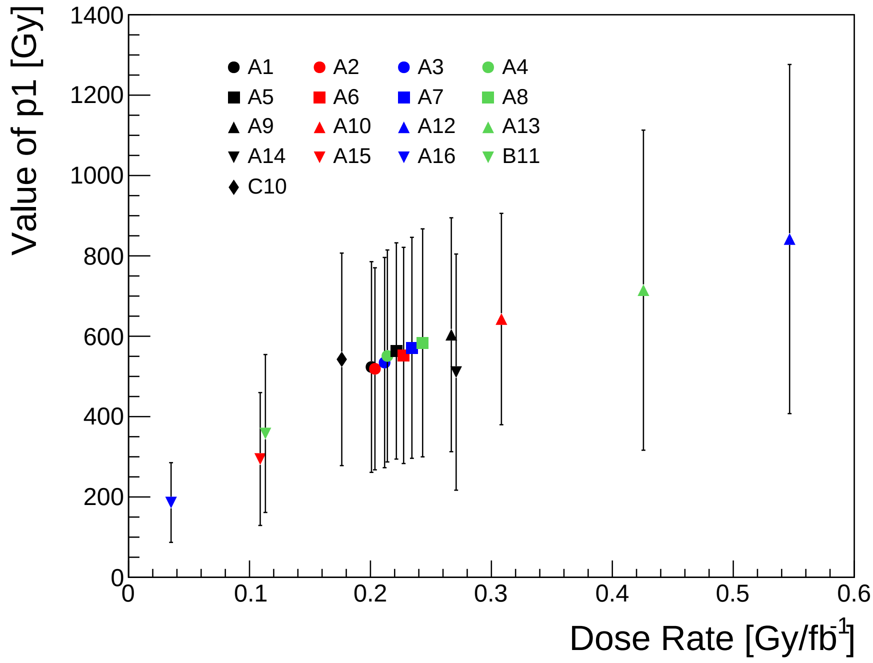

Figure 5.11: Value of p_1 parameter, obtained by an exponential fit of the form $e^{p_0 - dose/p_1}$ for the most degraded cells as a function of the dose rate in Gy/fb^{-1}.

5.4 Expected Relative light yield at the end of Run3 and HL-LHC

The expected relative light yield was calculated by extrapolating the exponential fit to the Run 2 data at the expected dose at the end of Run 3 and of the HL-LHC. Table 5.2 presents the values of the expected dose, of the relative light yield at the end of Run 3 and at the end of the HL-LHC. The total expected dose for the Run 3 is the sum of the dose estimated for the end of Run 2 and the dose estimated for the end of Run 3 using the dedicated dose map of Figure 5.5, assuming around 200 fb^{-1} acquired in Run 3-only. The same reasoning applies for the total expected dose at the end of the HL-LHC, which corresponds to the sum of the dose at the end of Run 3 with the dose in HL-LHC obtained with the respective conversion factors, presented in Figure 5.6. The uncertainties for the expected relative light yield were calculated by evaluating the difference between the relative light yield, for the exponential function, calculated with the uncertainty variation $p_i + \Delta p_i$ where $i = 1, 2$ and the nominal fit.

The results at the end of Run 3 show that the more affected cells are in layer A, and B11 and C10 cells with an expected light yield loss between 6 and 21%. For the remaining ones, the expected loss is between 1 and 6% (Figure 5.12). The relative uncertainty on the extrapolation is of the order of 5%.

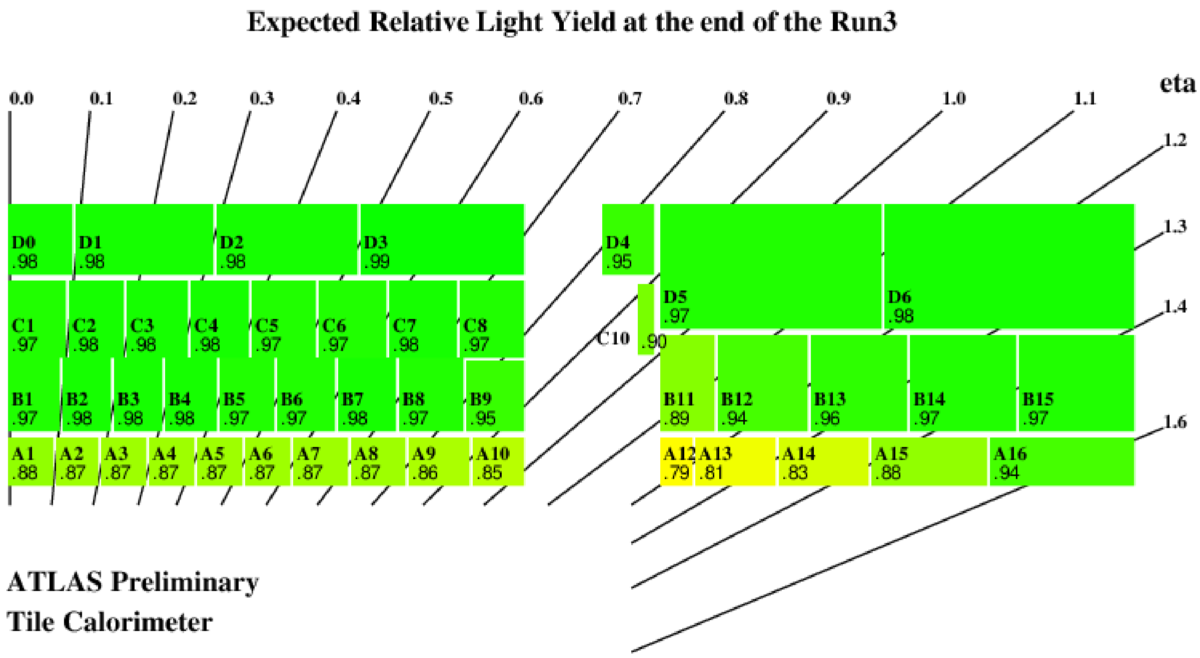

Figure 5.12: Expected relative light yield of the TileCal cells at the end of Run 3, assuming an integrated luminosity of 350 fb^{-1} [4, 8].

Since this model does not take into account a possible recovery or additional degradation of the scintillators between years or LHC runs, the end of Run 3 is also the beginning of the HL-LHC, so it is expected for TileCal to enter the HL-LHC phase with most of the cells unaffected in terms of light response. Preliminary results extrapolating to the end of the HL-LHC, in Figure 5.13 show that the most affected cells are again in layer A, and B11 and C10 cells, with an expected loss of light yield between 59 and 90%. For the remaining BC and D4 cells, the expected loss is between 25 and 50%. For the cells in the D layer, the expected loss is between 12 and 29%. The relative uncertainty on the extrapolation ranges from 40 to 100% for cells in the A layer, B11 and B12 cells, and is around 10% for the remaining ones. The uncertainties are very large, so it is still premature to make final conclusions about the TileCal radiation damage at the end of the LHC. More data from Run 3 will be needed to have more precision in the extrapolation.

The future TileCal performance depends on the scintillators and fibres robustness. Preliminary studies simulating a 50% loss of light yield show that the muon energy reconstruction performance is almost not affected and that the impact of this effect for the jet energy reconstruction is negligible [42]. Nevertheless, this study helped guiding the strategy for the TileCal phase II upgrade, where the PMTs reading the most degraded A cells will be replaced by PMTs with larger quantum efficiency in order to mitigate light loss with larger detection efficiency.

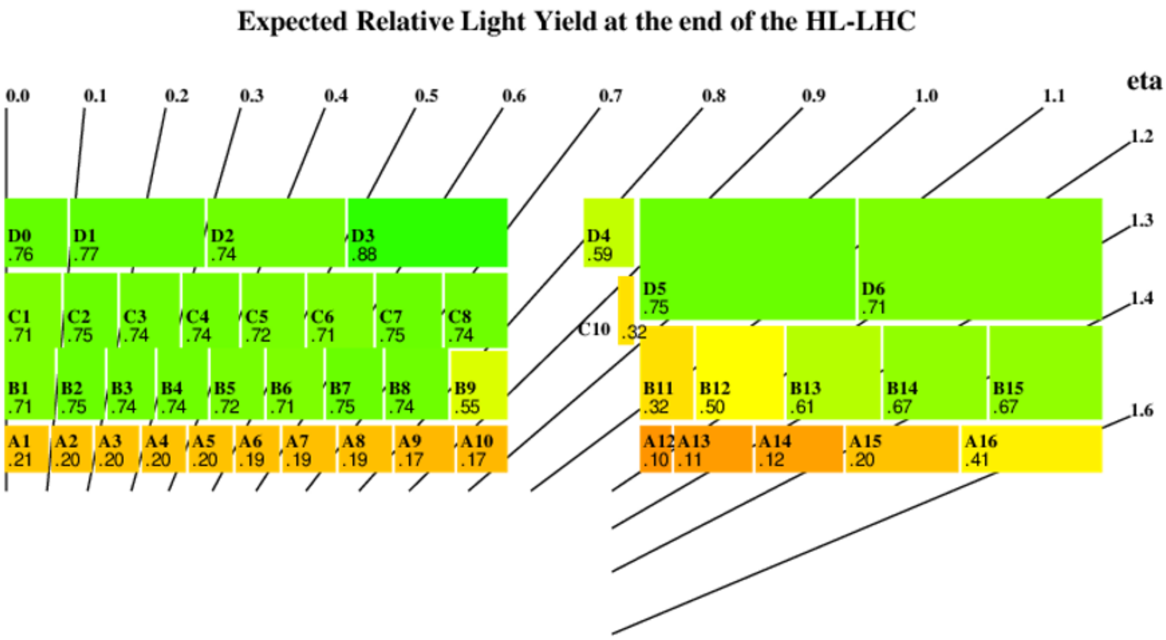

Figure 5.13: Expected relative light yield of the TileCal cells at the end of HL, assuming an integrated luminosity of 4000 fb^{-1}.

Chapter 6

Conclusion

The main work of this thesis consisted of studying the radiation hardness of the optical components of the ATLAS Tile Calorimeter. These components can degrade with radiation exposure compromising TileCal performance. The principal concern of the TileCal is the High Luminosity-LHC phase where the integrated luminosity can reach to 4000 fb^{-1}. Since the detector's lifetime will be extended, it is mandatory to study what can be expected during the future years in order to design mitigation strategies if needed. The strategies and the knowledge learned during the radiation hardness study can be broaden to future colliders such as the Future Circular Collider where the total integrated luminosity can reach 20-30 ab^{-1} [3].

The analysis is based on the difference in the calorimeter response to the Cesium and the Laser calibration systems. Thus, it is very important to precisely evaluate the uncertainties on the determination of the PMT calibration with the Laser system as well as the Cs systematics.

The uncertainties on the PMT calibration, described in Chapter 4, are addressed by a comparison between the TileCal response to the Cesium and Laser calibration systems using 2018 data. One of the advantages of the method is that it does not require many Cesium scans. This is very important since this system had a water leakage problem and the number of scans was significantly reduced in 2018. The final uncertainty obtained has a constant term around 0.5% and a term dependent on the integrated luminosity that reaches 0.1% at 63.3 fb^{-1} integrated luminosity in 2018.

The uncertainties on the PMT calibration were used in the evaluation of the radiation hardness of the TileCal optical components. The relative light yield of the detector cell's scintillators and fibres in Run 2 was measured using Cesium and Laser calibration data. The innermost cells are the most affected ones, which is expected since they are closer to the LHC beam pipe and the dose deposit is larger. Measurements during this Run have shown that cells in layer A, and B11 and C10 cells have already lost about 5% of light yield. Within 1% of uncertainty, no significant changes were found for the other cells.

A simple exponential was used to model the light yield degradation as a function of the accumulated dose simulated with GEANT4 for each TileCal cell. The parameters of the fit are different from cell to cell, indicating that they will degrade at different rates. One factor that may contribute to this is the dose rate. To study this, we investigated the dependence of the fit parameter on the dose rate using a subset of cells for which the degradation in Run 2 is non-negligible. The nominal trend indicates that the degradation rate is linearly dependent on the dose rate, but the large uncertainties affecting the contribution have to be reduced in order to have a clear conclusion.

The light yield degradation was extrapolated to the end of Run 3 and High Luminosity LHC phase from the exponential fit to the Run 2 measurements. At the end of Run 3, the great majority of TileCal cell is not expected to degrade more than 1 to 6%, while the most exposed cells belonging to the layer A, and the B9 and C10 cells expects a light loss between 6 and 21%. The extrapolation uncertainty is about 5%. The preliminary results from the extrapolation to the end of the HL-LHC phase show a light loss between 50 and 12% for most of the BC and all the D layers, with a relative uncertainty of 10%. A significant light loss is shown for the A layer cells, but the uncertainties are very large and possible effects of recovery during long shut down periods were not taken into account.

Part of the future work is to use more data, from the Run 3, to reduce the extrapolation uncertainty on the relative light yield at the end of the HL-LHC phase and to evaluate the impact of the relative light loss in the detection of particles. It is also important to study, in more detail, the dose rate impact in the degradation process and at which values this phenomenon is more substantial as well as study and to model the recovery of the scintillator materials.

Bibliography

[1] William R Leo. *Techniques for nuclear and particle physics experiments: a how-to approach*. Springer Science & Business Media, 2012.

[2] 2020 update of the european strategyfor particle physics by the european strategy group. https://home.cern/sites/home.web.cern.ch/files/2020-06/2020%20Update%20European%20Strategy.pdf. Accessed: 2020-10-13.

[3] FCC collaboration et al. Fcc-hh: The hadron collider: Future circular collider conceptual design report volume 3. *European Physical Journal: Special Topics*, 228(4):755–1107, 2019.

[4] Light yield public plots. https://twiki.cern.ch/twiki/bin/view/AtlasPublic/ApprovedPlotsTileCalibrationCombined. Accessed: 2020-11-05.

[5] Laser uncertainties. https://twiki.cern.ch/twiki/bin/view/AtlasPublic/ApprovedPlotsTileCalibrationLaser. Accessed: 2020-10-13.

[6] B Pereira. The 6th idpasc/lip phd students workshop poster. https://indico.lip.pt/event/699/contributions/2443/. Accessed: 2020-10-13.

[7] B Pereira on behalf of the ATLAS Collaboration. The 5th international conference on particle physics and astrophysics poster. https://indico.particle.mephi.ru/event/35/contributions/2312/. Accessed: 2020-10-13.

[8] B Pereira on behalf of the ATLAS Collaboration. Radiation hardness of the atlas tile calorimeter optical components. In *Journal of Physics: Conference Series*, volume 1690, page 012053. IOP Publishing, 2020.

[9] Carl Zorn. *Plastic and liquid organic scintillators*, volume 9. 1993.

[10] Brian Harold Bransden, Charles Jean Joachain, and Theodor J Plivier. *Physics of atoms and molecules*. Pearson Education India, 2003.

[11] Peter Atkins and Ronald Friedman. *Molecular quantum mechanics*. Oxford university press, 2011.

[12] Maria Evelina Fantacci. Methods and instrumentation for measuring radioactivity. In *Nuclear Medicine Textbook*, pages 117–135. Springer, 2019.

[13] Andriy Chmyrov. *Photo-induced dark states in fluorescence spectroscopy – investigations and applications*. PhD thesis, 06 2010.

[14] J B Birks. Scintillations from organic crystals: Specific fluorescence and relative response to different radiations. *Proceedings of the Physical Society. Section A*, 64(10):874–877, oct 1951.

[15] Yu N Kharzheev. Radiation hardness of scintillation detectors based on organic plastic scintillators and optical fibers. *Physics of Particles and Nuclei*, 50(1):42–76, 2019.

[16] V Khachatryan, AM Sirunyan, A Tumasyan, A Litomin, V Mossolov, N Shumeiko, M Van De Klundert, H Van Haevermaet, P Van Mechelen, A Van Spilbeeck, et al. Dose rate effects in the radiation damage of the plastic scintillators of the cms hadron endcap calorimeter. *Journal of Instrumentation*, 11(10):T10004, 2016.

[17] AD Bross and A Pla-Dalmau. Radiation damage of plastic scintillators. *IEEE transactions on nuclear science*, 39(5):1199–1204, 1992.

[18] E Biagtan, E Goldberg, J Harmon, and R Stephens. Effect of gamma radiation dose rate on the light output of commercial polymer scintillators. *Nuclear Instruments and Methods in Physics Research Section B: Beam Interactions with Materials and Atoms*, 93(3):296–301, 1994.

[19] B. Bicken, U. Holm, T. Marckmann, K. Wick, and M. Rohde. Recovery and permanent radiation damage of plastic scintillators at different dose rates. In *1990 IEEE Nuclear Science Symposium Conference Record*, pages 871–876, 1990.

[20] Yves Sirois and Richard Wigmans. Effects of long-term low-level exposure to radiation as observed in acrylic scintillator: Cause and prevention of radiation disease in uranium calorimeters. *Nuclear Instruments and Methods in Physics Research Section A: Accelerators, Spectrometers, Detectors and Associated Equipment*, 240(2):262–274, 1985.

[21] ATLAS Collaboration. The production and qualification of scintillator tiles for the atlas hadronic calorimeter. Technical report, 2007.

[22] Kamal Ahmed. *Design and Experimental Investigations of Electrical Breakdown in a Plasma Jet Device and Applications*. PhD thesis, 08 2014.

[23] Hamamatsu. `https://www.hamamatsu.com/resources/pdf/etd/PMT_handbook_v4E.pdf`. Accessed: 2020-11-22.

[24] Alessandro De Angelis and Mário João Martins Pimenta. *Introduction to particle and astroparticle physics: questions to the Universe*. Springer, 2015.

[25] Description of the linac2. `https://home.cern/science/accelerators/linear-accelerator-2`. Accessed: 2020-07-14.

[26] Description of the proton syncrotron booster. `https://home.cern/science/accelerators/proton-synchrotron-booster`. Accessed: 2020-07-14.

[27] Description of the proton synchrotron. https://home.cern/science/accelerators/proton-synchrotron. Accessed: 2020-07-14.

[28] Description of the super proton synchrotron. https://home.cern/science/accelerators/super-proton-synchrotron. Accessed: 2020-07-17.

[29] Description of the large hadron collider. https://home.cern/science/accelerators/large-hadron-collider. Accessed: 2020-07-17.

[30] Lyndon Evans and Philip Bryant. Lhc machine. *Journal of instrumentation*, 3(08):S08001, 2008.

[31] schematic of cern. https://cds.cern.ch/record/2636343?ln=fr. Accessed: 2020-09-30.

[32] Lhc report: The final days of run 2. https://home.cern/news/news/accelerators/lhc-report-final-days-run-2. Accessed: 2020-07-17.

[33] Image of the lhc high luminosity upgrade. https://project-hl-lhc-industry.web.cern.ch/sites/project-hl-lhc-industry.web.cern.ch/files/inline-images/HL-LHC-plan-2020-Plan-1.pdf. Accessed: 2020-07-22.

[34] ATLAS Collaboration. Atlas inner detector : Technical design report, 1. https://cds.cern.ch/record/331063.

[35] ATLAS Collaboration. Atlas liquid-argon calorimeter : Technical design report. https://cds.cern.ch/record/331061.

[36] ATLAS Collaboration. Atlas tile calorimeter : Technical design report, cern-lhcc-96-042. Technical report, 1996.

[37] ATLAS Collaboration. Atlas muon spectrometer : Technical design report. https://cds.cern.ch/record/331068.

[38] ATLAS Collaboration. Atlas magnet system : Technical design report, 1. https://cds.cern.ch/record/338080.

[39] ATLAS Collaboration. The atlas experiment at the cern large hadron collider. *Jinst*, 3:S08003, 2008.

[40] Image of the atlas inner detector. https://cds.cern.ch/images/CERN-GE-0803014-01. Accessed: 2020-07-22.

[41] ATLAS Collaboration. Readiness of the atlas tile calorimeter for lhc collisions. *The European Physical Journal C*, 70(4):1193–1236, 2010.

[42] ATLAS Collaboration. Technical design report for the phase-ii upgrade of the atlas tile calorimeter. Technical report, 2017.

[43] J Abdallah, J Proudfoot, S Némécek, JE Pilcher, C Vellidis, P Lourtie, J Li, A Vartapetian, M Simonyan, F Marroquim, et al. The production and qualification of scintillator tiles for the atlas hadronic calorimeter. 2007.

[44] Pawel Klimek and on behalf of the ATLAS Collaboration. Calibration and performance of the atlas tile calorimeter during the lhc run 2. In *Journal of Physics: Conference Series*, volume 1162, page 012003. IOP Publishing, 2019.

[45] Calibration public plots. `https://twiki.cern.ch/twiki/bin/view/AtlasPublic/ApprovedPlotsTileCalibration`. Accessed: 2020-09-30.

[46] P Adragna, C Alexa, K Anderson, A Antonaki, A Arabidze, L Batkova, V Batusov, HP Beck, P Bednar, E Bergeaas Kuutmann, et al. Testbeam studies of production modules of the atlas tile calorimeter. *Nuclear Instruments and Methods in Physics Research Section A: Accelerators, Spectrometers, Detectors and Associated Equipment*, 606(3):362–394, 2009.

[47] K Anderson, A Gupta, F Merritt, M Oreglia, J Pilcher, H Sanders, M Shochet, F Tang, R Teuscher, H Wu, et al. Design of the front-end analog electronics for the atlas tile calorimeter. *Nuclear Instruments and Methods in Physics Research Section A: Accelerators, Spectrometers, Detectors and Associated Equipment*, 551(2-3):469–476, 2005.

[48] Cis calibration constant averages of all the high-gain. `https://twiki.cern.ch/twiki/bin/view/AtlasPublic/ApprovedPlotsTileCalibrationCIS`. Accessed: 2020-08-26.

[49] J Abdallah, C Alexa, Y Amaral Coutinho, SP Amor Dos Santos, KJ Anderson, G Arabidze, JP Araque, A Artamonov, L Asquith, R Astalos, et al. The laser calibration of the atlas tile calorimeter during the lhc run 1. *Journal of Instrumentation*, 11(10):T10005, 2016.

[50] Evolution of the mean relative response measured by the laser calibration system. `https://twiki.cern.ch/twiki/bin/view/AtlasPublic/ApprovedPlotsTileCalibrationLaser`. Accessed: 2020-08-26.

[51] G Blanchot, M Bosman, J Budagov, M Cavalli-Sforza, I Efthymiopoulos, A Isaev, Y Ivanyushenkov, A Karyukhin, S Kopikov, M Nessi, et al. The cesium source calibration and monitoring system of the atlas tile calorimeter: design, construction and results. *Journal of Instrumentation*, 15(03):P03017, 2020.

[52] Evolution of tile calorimeter response to cesium source. `https://twiki.cern.ch/twiki/bin/view/AtlasPublic/ApprovedPlotsTileCalibration#Cesium`. Accessed: 2020-08-26.

[53] Radiation public plots. `https://twiki.cern.ch/twiki/bin/view/AtlasPublic/RadiationSimulationPublicResults`. Accessed: 2020-10-25.

[54] R Pedro and on behalf of the ATLAS Collaboration. Optics robustness of the atlas tile calorimeter. In *Journal of Physics: Conference Series*, volume 1162, page 012004. IOP Publishing, 2019.

Appendix A

Appendix A

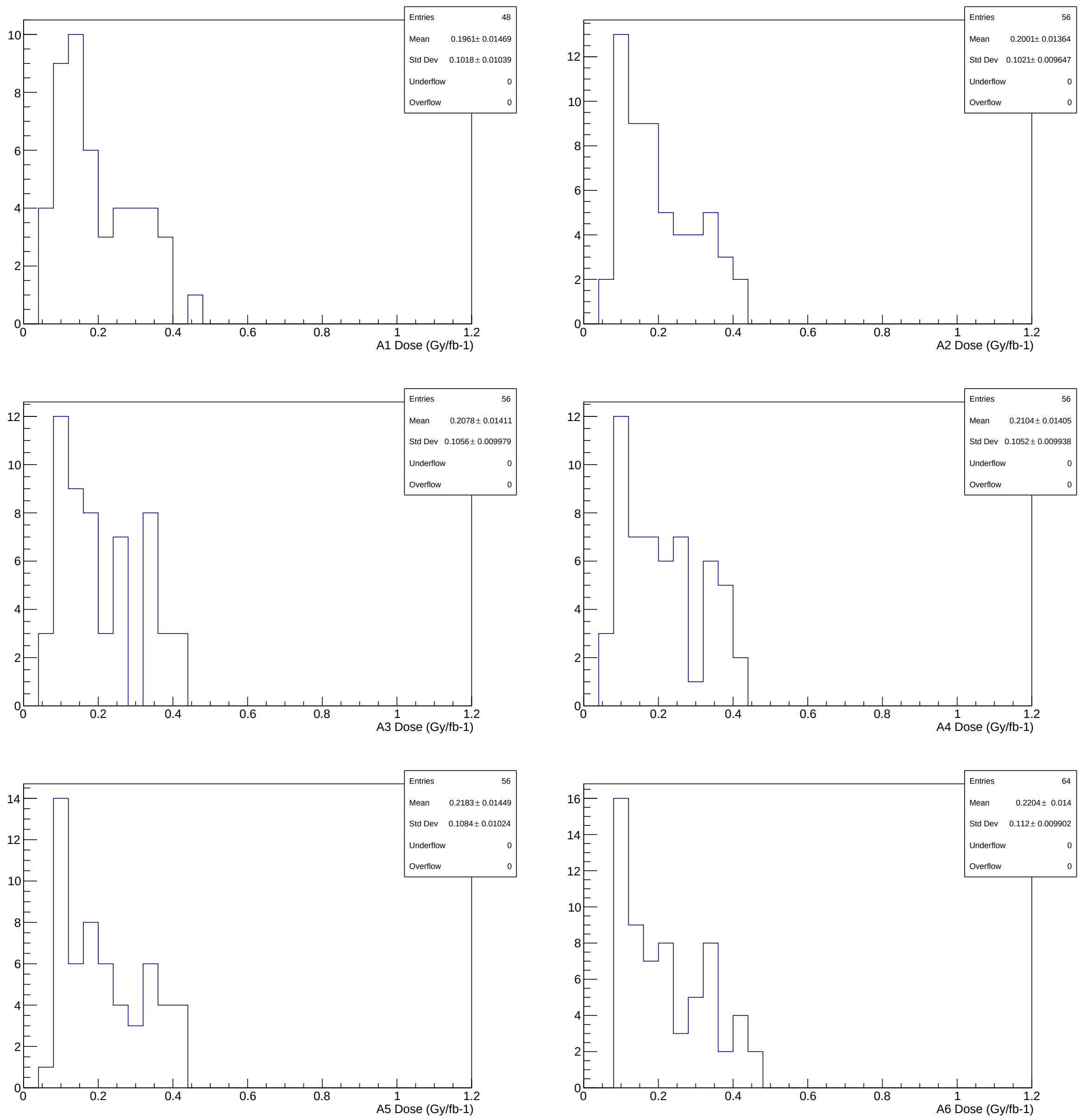

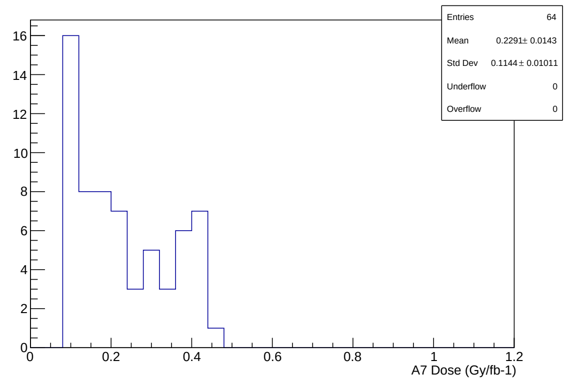
Entries 64
Mean 0.2291 ± 0.0143
Std Dev 0.1144 ± 0.01011
Underflow 0
Overflow 0
A7 Dose (Gy/fb-1)

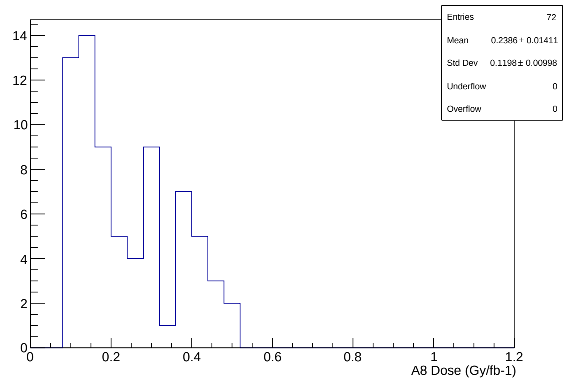
Entries 72
Mean 0.2386 ± 0.01411
Std Dev 0.1198 ± 0.00998
Underflow 0
Overflow 0
A8 Dose (Gy/fb-1)

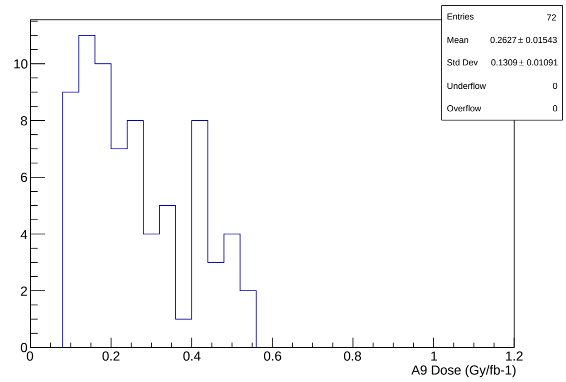
Entries 72
Mean 0.2627 ± 0.01543
Std Dev 0.1309 ± 0.01091
Underflow 0
Overflow 0
A9 Dose (Gy/fb-1)

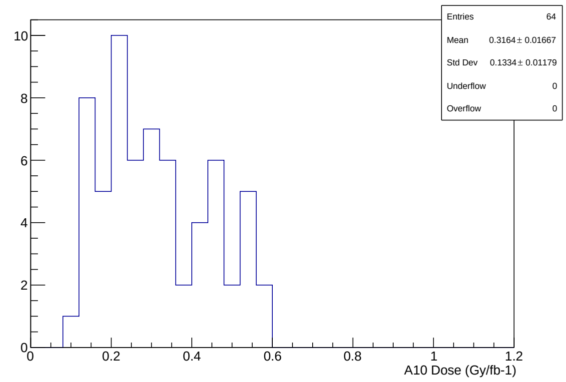
Entries 64
Mean 0.3164 ± 0.01667
Std Dev 0.1334 ± 0.01179
Underflow 0
Overflow 0
A10 Dose (Gy/fb-1)

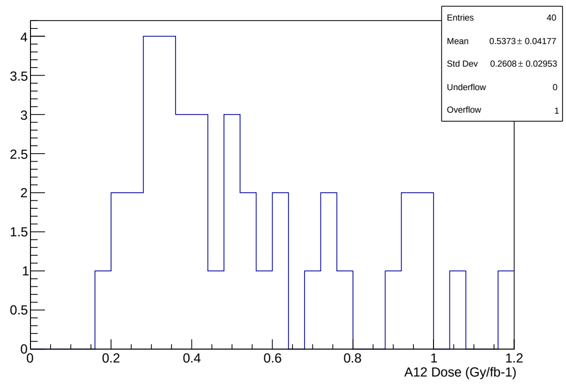
Entries 40
Mean 0.5373 ± 0.04177
Std Dev 0.2608 ± 0.02953
Underflow 0
Overflow 1
A12 Dose (Gy/fb-1)

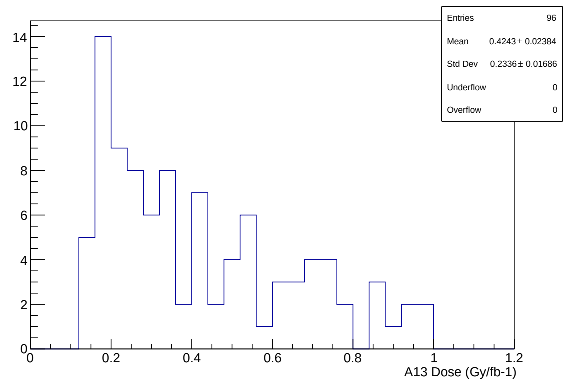
Entries 96
Mean 0.4243 ± 0.02384
Std Dev 0.2336 ± 0.01686
Underflow 0
Overflow 0
A13 Dose (Gy/fb-1)

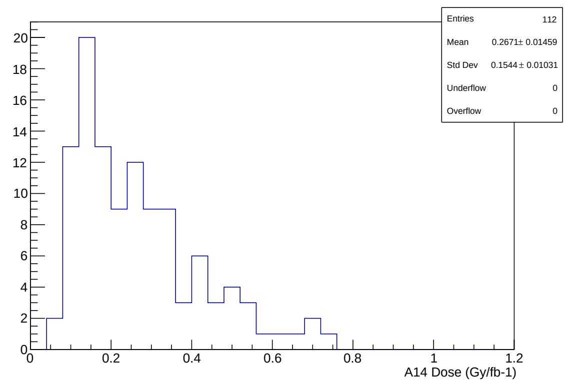
Entries 112
Mean 0.2671 ± 0.01459
Std Dev 0.1544 ± 0.01031
Underflow 0
Overflow 0
A14 Dose (Gy/fb-1)

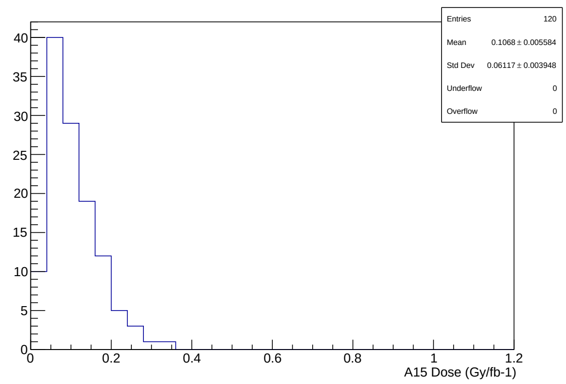
Entries 120
Mean 0.1068 ± 0.005584
Std Dev 0.06117 ± 0.003948
Underflow 0
Overflow 0
A15 Dose (Gy/fb-1)

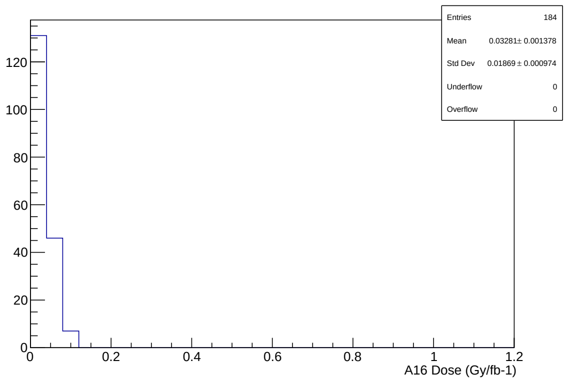
Entries 184
Mean 0.03281 ± 0.001378
Std Dev 0.01869 ± 0.000974
Underflow 0
Overflow 0
A16 Dose (Gy/fb-1)

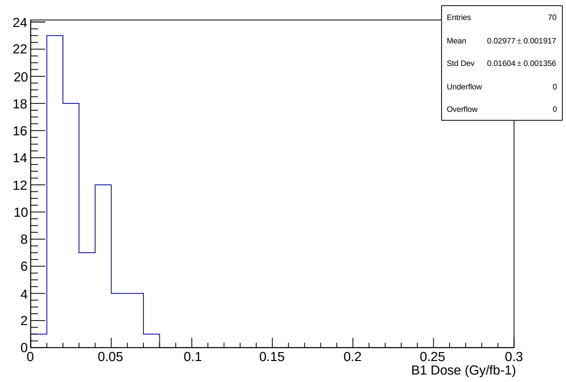
Entries 70
Mean 0.02977 ± 0.001917
Std Dev 0.01604 ± 0.001356
Underflow 0
Overflow 0
B1 Dose (Gy/fb-1)

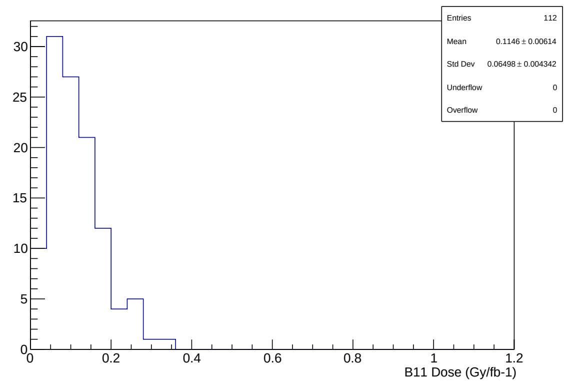
Entries 112
Mean 0.1146 ± 0.00614
Std Dev 0.06498 ± 0.004342
Underflow 0
Overflow 0
B11 Dose (Gy/fb-1)

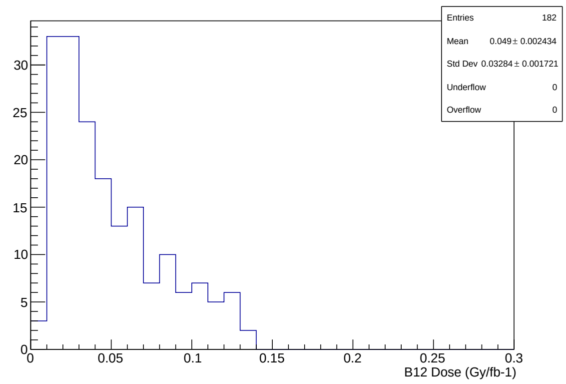
Entries 182
Mean 0.049 ± 0.002434
Std Dev 0.03284 ± 0.001721
Underflow 0
Overflow 0
B12 Dose (Gy/fb-1)

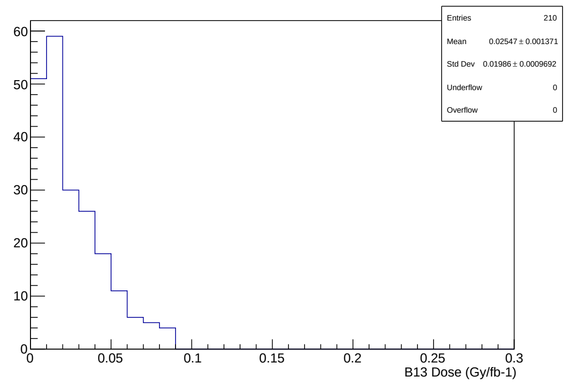
Entries 210
Mean 0.02547 ± 0.001371
Std Dev 0.01986 ± 0.0009692
Underflow 0
Overflow 0
B13 Dose (Gy/fb-1)

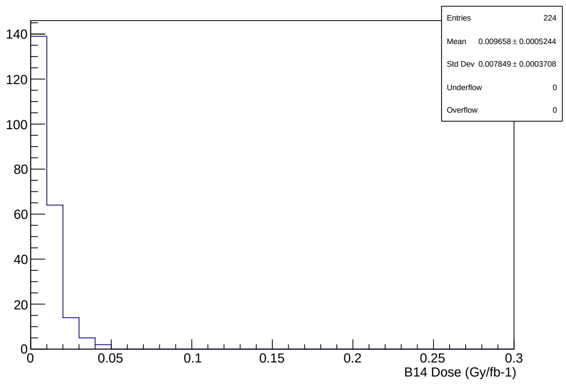
Entries 224
Mean 0.009658 ± 0.0005244
Std Dev 0.007849 ± 0.0003708
Underflow 0
Overflow 0
B14 Dose (Gy/fb-1)

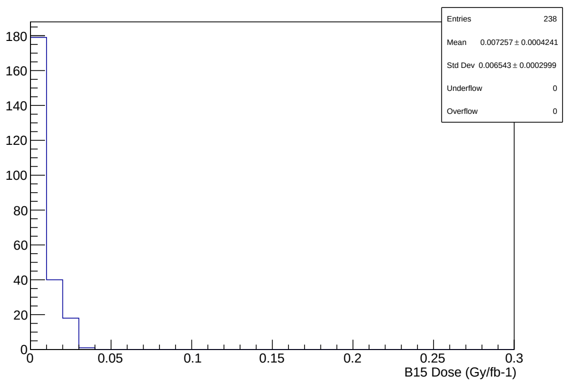
Entries 238
Mean 0.007257 ± 0.0004241
Std Dev 0.006543 ± 0.0002999
Underflow 0
Overflow 0
B15 Dose (Gy/fb-1)

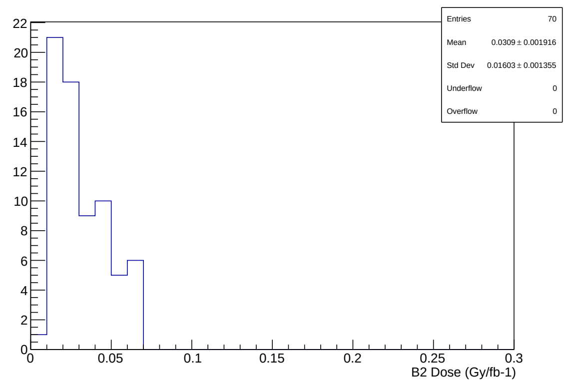
Entries 70
Mean 0.0309 ± 0.001916
Std Dev 0.01603 ± 0.001355
Underflow 0
Overflow 0
B2 Dose (Gy/fb-1)

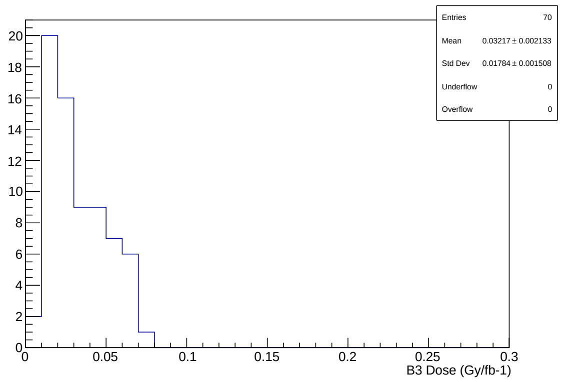
Entries 70
Mean 0.03217 ± 0.002133
Std Dev 0.01784 ± 0.001508
Underflow 0
Overflow 0
B3 Dose (Gy/fb-1)

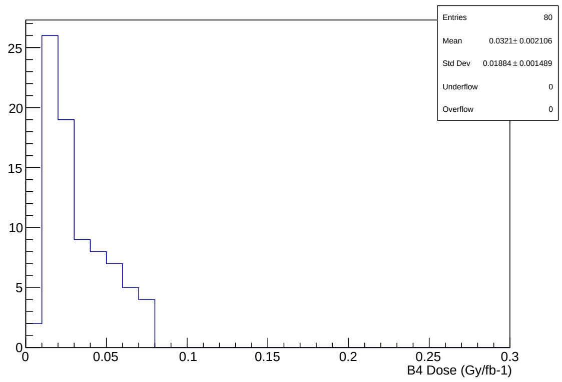
Entries 80
Mean 0.0321± 0.002106
Std Dev 0.01884 ± 0.001489
Underflow 0
Overflow 0
B4 Dose (Gy/fb-1)

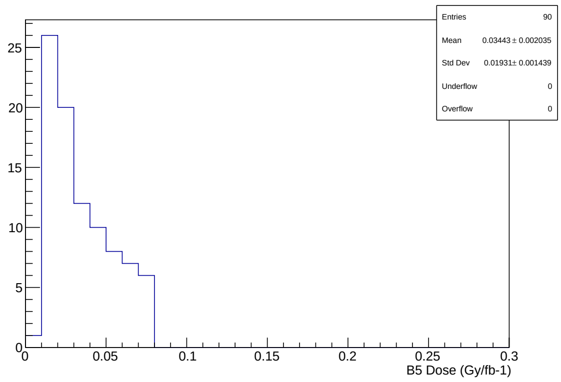
Entries 90
Mean 0.03443 ± 0.002035
Std Dev 0.01931± 0.001439
Underflow 0
Overflow 0
B5 Dose (Gy/fb-1)

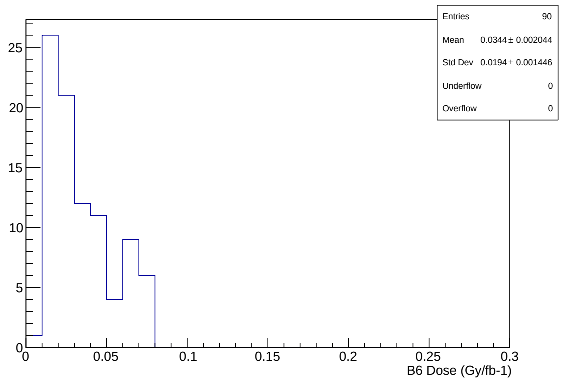
Entries 90
Mean 0.0344 ± 0.002044
Std Dev 0.0194 ± 0.001446
Underflow 0
Overflow 0
B6 Dose (Gy/fb-1)

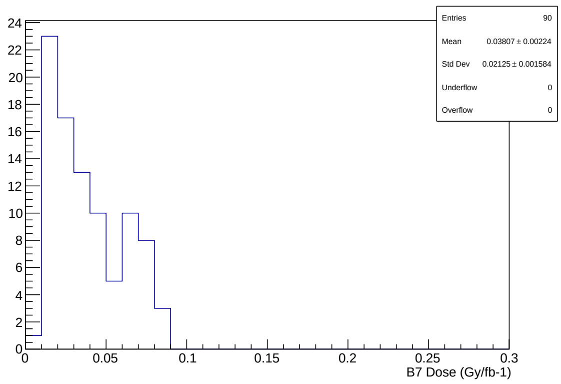
Entries 90
Mean 0.03807 ± 0.00224
Std Dev 0.02125 ± 0.001584
Underflow 0
Overflow 0
B7 Dose (Gy/fb-1)

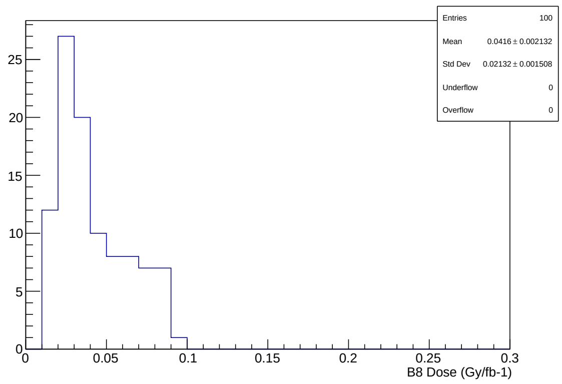
Entries 100
Mean 0.0416 ± 0.002132
Std Dev 0.02132 ± 0.001508
Underflow 0
Overflow 0
B8 Dose (Gy/fb-1)

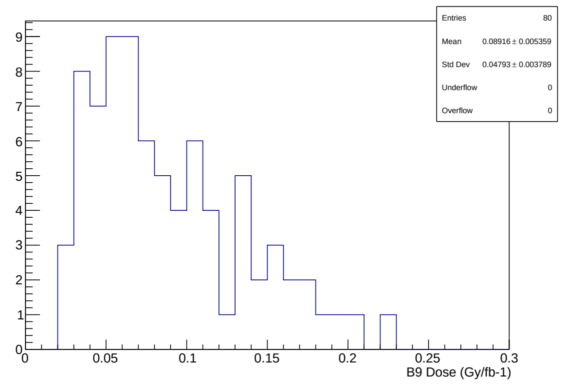
Entries 80
Mean 0.08916 ± 0.005359
Std Dev 0.04793 ± 0.003789
Underflow 0
Overflow 0
B9 Dose (Gy/fb-1)

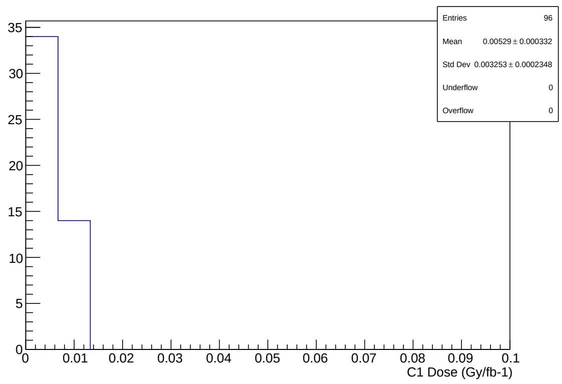
Entries 96
Mean 0.00529 ± 0.000332
Std Dev 0.003253 ± 0.0002348
Underflow 0
Overflow 0
C1 Dose (Gy/fb-1)

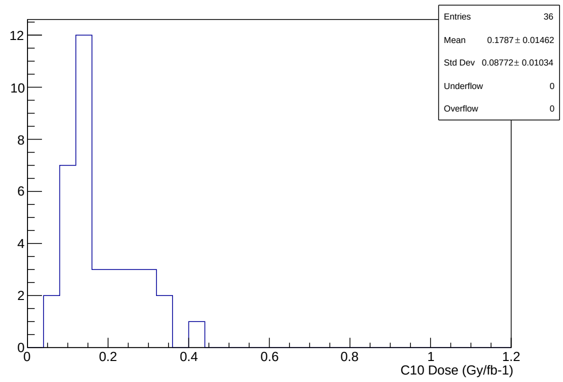
Entries 36
Mean 0.1787 ± 0.01462
Std Dev 0.08772 ± 0.01034
Underflow 0
Overflow 0
C10 Dose (Gy/fb-1)

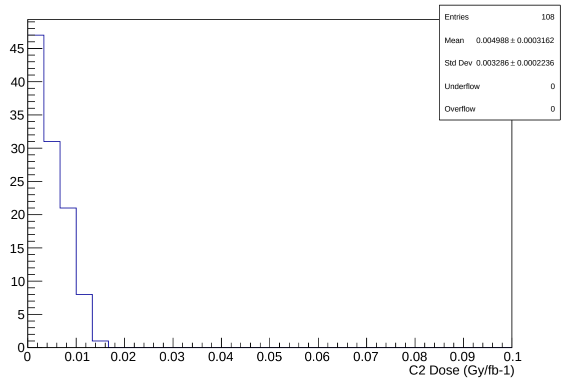
Entries 108
Mean 0.004988 ± 0.0003162
Std Dev 0.003286 ± 0.0002236
Underflow 0
Overflow 0
C2 Dose (Gy/fb-1)

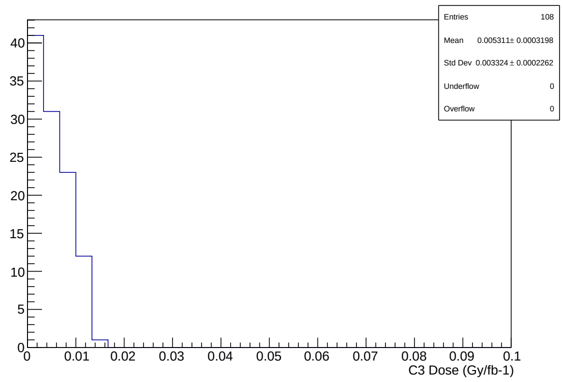
Entries 108
Mean 0.005311± 0.0003198
Std Dev 0.003324 ± 0.0002262
Underflow 0
Overflow 0
C3 Dose (Gy/fb-1)

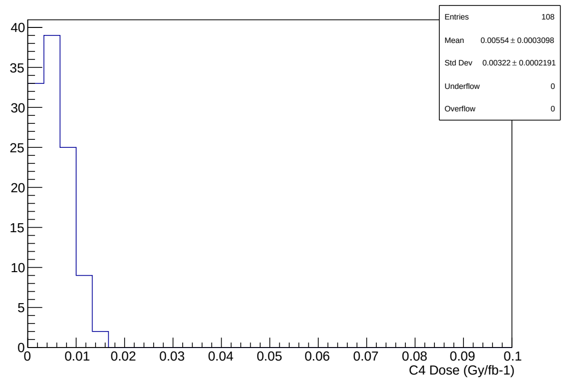
Entries 108
Mean 0.00554 ± 0.0003098
Std Dev 0.00322 ± 0.0002191
Underflow 0
Overflow 0
C4 Dose (Gy/fb-1)

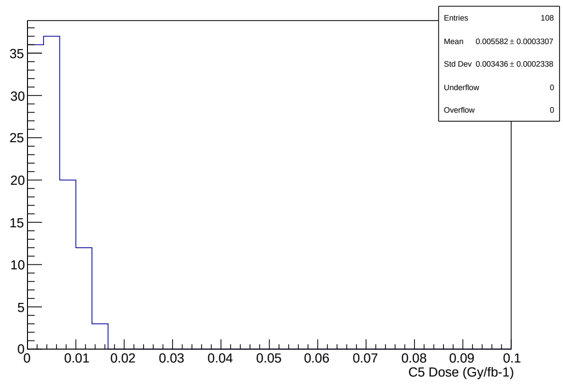
Entries 108
Mean 0.005582 ± 0.0003307
Std Dev 0.003436 ± 0.0002338
Underflow 0
Overflow 0
C5 Dose (Gy/fb-1)

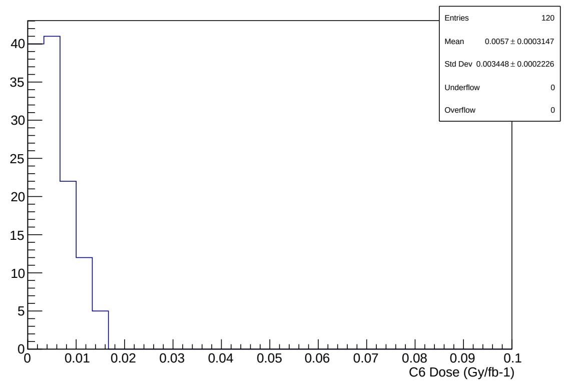
Entries 120
Mean 0.0057 ± 0.0003147
Std Dev 0.003448 ± 0.0002226
Underflow 0
Overflow 0
C6 Dose (Gy/fb-1)

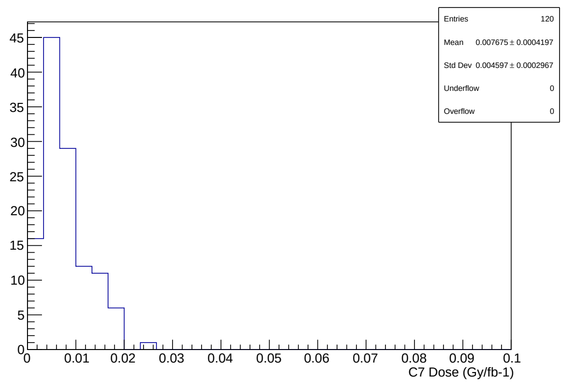
Entries 120
Mean 0.007675 ± 0.0004197
Std Dev 0.004597 ± 0.0002967
Underflow 0
Overflow 0
C7 Dose (Gy/fb-1)

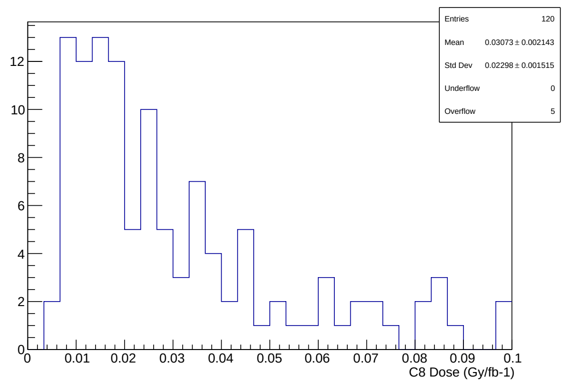
Entries 120
Mean 0.03073 ± 0.002143
Std Dev 0.02298 ± 0.001515
Underflow 0
Overflow 5
C8 Dose (Gy/fb-1)

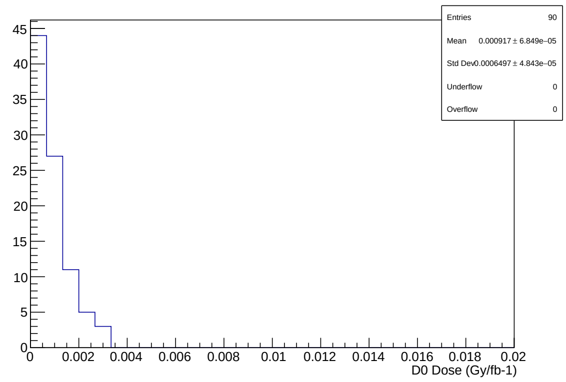
Entries 90
Mean 0.000917 ± 6.849e−05
Std Dev 0.0006497 ± 4.843e−05
Underflow 0
Overflow 0
D0 Dose (Gy/fb-1)

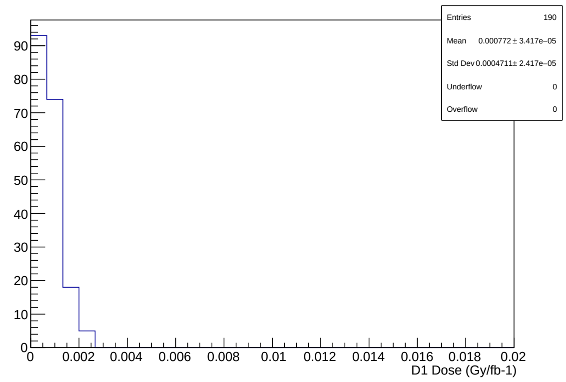
Entries 190
Mean 0.000772 ± 3.417e−05
Std Dev 0.0004711 ± 2.417e−05
Underflow 0
Overflow 0
D1 Dose (Gy/fb-1)

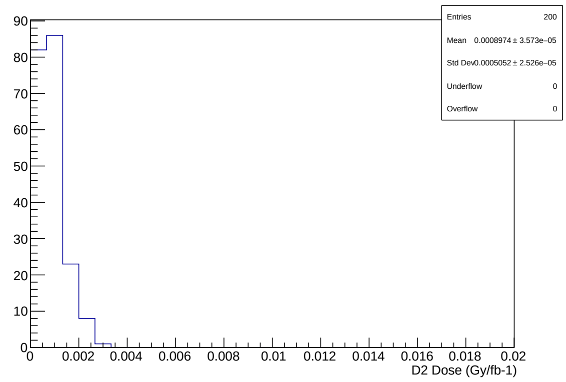
Entries 200
Mean 0.0008974 ± 3.573e−05
Std Dev 0.0005052 ± 2.526e−05
Underflow 0
Overflow 0
D2 Dose (Gy/fb-1)

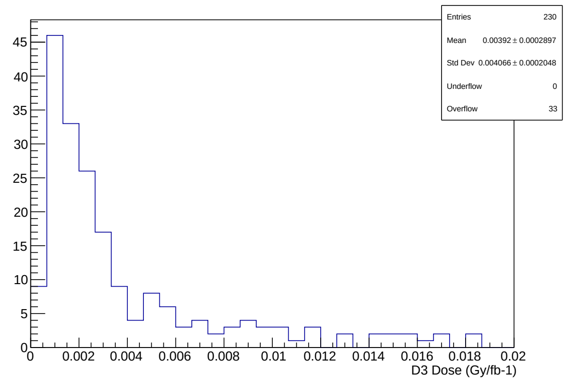
Entries 230
Mean 0.00392 ± 0.0002897
Std Dev 0.004066 ± 0.0002048
Underflow 0
Overflow 33
D3 Dose (Gy/fb-1)

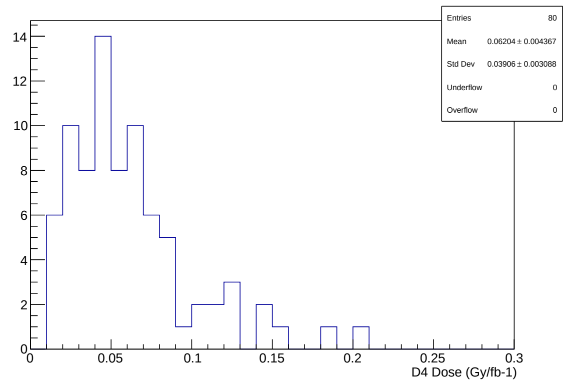
Entries 80
Mean 0.06204 ± 0.004367
Std Dev 0.03906 ± 0.003088
Underflow 0
Overflow 0
D4 Dose (Gy/fb-1)

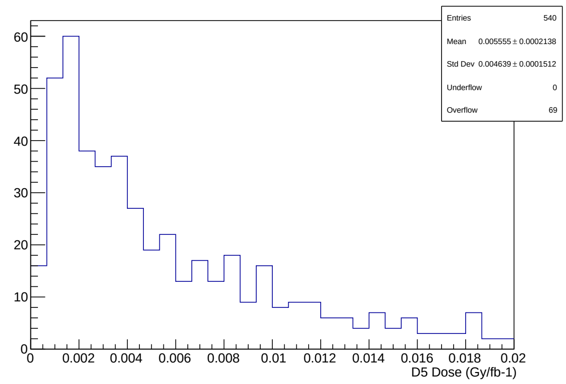
Entries 540
Mean 0.005555 ± 0.0002138
Std Dev 0.004639 ± 0.0001512
Underflow 0
Overflow 69
D5 Dose (Gy/fb-1)

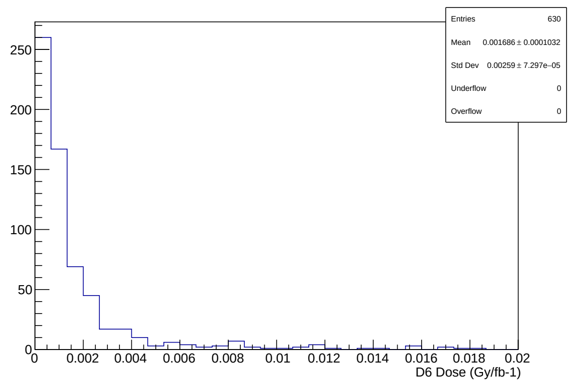
Entries 630
Mean 0.001686 ± 0.0001032
Std Dev 0.00259 ± 7.297e−05
Underflow 0
Overflow 0
D6 Dose (Gy/fb-1)

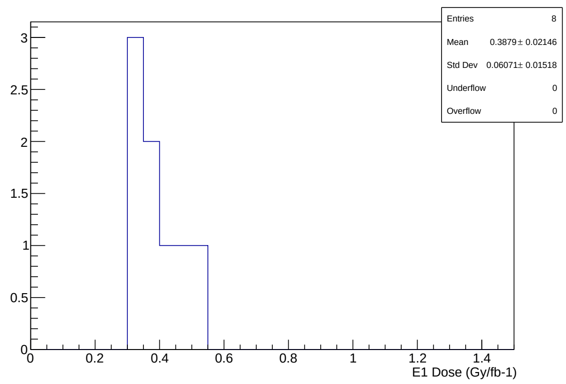
Entries 8
Mean 0.3879 ± 0.02146
Std Dev 0.06071 ± 0.01518
Underflow 0
Overflow 0
E1 Dose (Gy/fb-1)

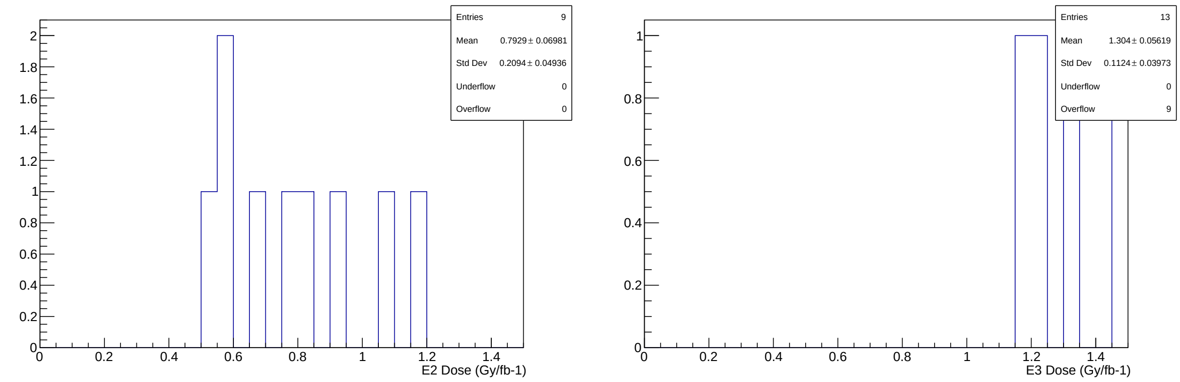

Figure A.1: Distribution of the dose values, obtained in bins of 4 cm $\times$ 4 cm, using GEANT4 simulation of the ATLAS detector in the Tile calorimeter region for 50000 $p-p$ generated collisions at the centre-of-mass energy of $\sqrt{s}=13$ TeV.